Imperial College
London

From EMAT to Image: Practical Guided Wave Tomography

by

Matthias Seher

A thesis submitted to Imperial College London for the degree of

Doctor of Philosophy

Department of Mechanical Engineering

Imperial College London

October 2015

Copyright Declaration

Declaration of Originality

The content presented in the thesis "From EMAT to Image: Practical Guided Wave Tomography" is entirely the result of the authors own independent research under the supervision of Professor Michael J. S. Lowe and co-supervision of Dr. Peter Huthwaite. All published or unpublished material used in this thesis has been given full acknowledgement. The author is unaware of any conflicts of interest and no human beings or animals were hurt during the production of the underlying research. Informed consent has been granted where required.

Matthias Seher

London, 19. October, 2015

Abstract

The detection and characterisation of corrosion type defects on pipelines is a major challenge for the petrochemical industry, especially in regions with poor accessibility. Guided wave tomography is one feasible approach to inspect areas with restricted access by transmitting guided waves through the area and then processing the measured wave field into a thickness map of the pipeline wall, without having to take measurements at all points on the surface. The key objective of this research project is to develop, implement and test a prototype guided wave tomography system based on the A0 Lamb mode.

For the development of a guided wave tomography system a low-frequency, omni-directional A0 Lamb wave ElectroMagnetic Acoustic Transducer (EMAT) is developed, and operates at 0.50 MHzmm on a steel plate. For that, a parametric Finite Element (FE) model is implemented in a commercially available FE software and a numerical optimization process employing a genetic algorithm is set up to optimised the EMAT design for an improved A0 mode selectivity. The FE model is validated against measurements on an aluminium plate and on a steel plate. A two-step model-based design approach is proposed whereby only the Lorentz force is used in the first step for the optimisation and then in a second step, a realistic estimate of the mode selectivity can be obtained by additionally considering the magnetisation force. The optimised design fulfils the S0 suppression design requirement and is integrated into the guided wave tomography system consisting of two ring arrays.

The developed guided wave tomography system is tested on two steel pipes with smooth and well defined defect. The repeatability of measurements is assessed and the robustness of the guided wave tomography measurements to sensor position errors is investigated. It is demonstrated that there is a small influence on the thickness reconstruction for fairly large systematic and unsystematic position errors. Similar results are obtained for single sensor failures or gaps in the arrays and an increase in sensor spacing is found to increase reconstruction artefacts. With Golay complementary sequences, a signal processing technique is presented that allows for a significant increase in the data capture speed with the same performance as time averaging.

Three areas with restricted access, support locations, pipe clamps and STOPAQ(R) coatings, are considered and their influence on the thickness reconstruction is investigated relative to a reference configuration and only a small influence is found in the experiments.

Contents

List of Figures

List of Tables

Chapter 1

Introduction

1.1 Motivation

Detecting and characterising defects in structures is vital for many industries in order to avoid costly failures. The oil industry is one example that is facing the inspection task of determining the integrity of many thousand kilometres of pipelines, which may have been in service for many years and subjected to corrosion. Non-destructive testing is one means of inspecting such pipelines, as it allows for inspection without causing further damage. There are a plethora of inspection techniques, which exploit various physical phenomena, such as the interaction of ultrasound or electromagnetic fields with the damaged regions to identify or characterise the damage and are tailored for various inspection scenarios. One class of techniques are long-range guided wave based techniques, which have been used by the industry for over fifteen years and it has been shown that they can compete with longer-established methods such as inspection pigs [Wagner et al., 2013]. Guided waves have the significant advantage that they can scan large lengths (typically tens and up to hundreds of metres from a single measurement). However, while estimating the location is generally straightforward from such measurements, determining the shape of the defect and its size in each dimension is difficult without more information [Carandente and Cawley, 2012]. For this reason, the Guided Wave Testing (GWT) method has been

established as a screening method, after which indications are followed up by detailed local inspections [British Standards Institution, 2011].

While the location of a defect can be established from GWT, there is then still a need to accurately determine the minimum remnant wall thickness, which is particularly important for characterising corrosion defects and this information may further contribute to estimating the remaining life of the component. Traditional thickness gauging measurements, like ultrasonic point-wise thickness gauging, are a widespread and well established technique to follow up on indications given by GWT. They allow for an efficient, reliable and cost-effective inspection of small areas, where direct access to the region of interest is possible. However, for regions of interest with restricted access such as near supports, under clamps or coatings, traditional thickness gauging techniques are often only deployable with some additional effort. By contrast, guided wave tomography, which is another inspection approach, whereby guided waves are transmitted through the area of interest and then processed into an image, can produce a thickness map of the pipeline wall without having to take measurements at all points on the surface. This technique exploits the dispersive nature of guided waves, which change their speed as the pipe wall thickness changes. This speed variation can be reconstructed by an imaging algorithm and then converted into a thickness measurement using the known dispersion relationship.

An attractive approach in guided wave tomography is to excite and measure dispersive Lamb waves, which are also the focus of this research project. A challenging aspect of guided wave tomography with Lamb waves is that multiple Lamb wave modes may exist at any one frequency, even at low frequencies. One approach is to simply send and receive multiple modes as for example in [Jansen and Hutchins, 1990], [Hou et al., 2004], [Miller and Hinders, 2014], however, the thickness reconstruction may suffer due to uncertainties in the signal processing used to separate out the various modes. Since the higher order modes exhibit a cut-off frequency (see Figure 1.2), some attempts have been made to exploit this for flaw detection, such as [Rose and Barshinger, 1998] or [Belanger, 2010], [Belanger, 2014]. By comparison, attempts to excite and measure a single Lamb wave mode by careful transduction have shown superior results, using the S0 mode in [Volker and Vos, 2012], [Volker and Vos, 2013], [Volker and van Zon, 2013], [Volker et al., 2015] and the A0 mode in [Pei et al., 1996], [Wright et al., 1997], [Belanger, 2010], [Huthwaite and Simonetti, 2013], [Huthwaite, 2014], [Instanes et al., 2015] allowing for accurate thickness maps of

complex defects to be produced. It needs to be remarked, that the absolute accuracy of the various approaches to guided wave tomography underlie certain constraints, for example imposed by the resolution limit or geometry of the defect and further improvements are being pursued by several research groups, including the afore mentioned. The relative merits of the A0 and S0 mode are discussed in [Huthwaite et al., 2013a] and based on this, here the focus is on exploiting A0 Lamb waves. There, the A0 mode has been shown to be more sensitive to the majority of corrosion defects than the S0 mode, at the operation point marked in Figure 1.2.

One of the practical issues identified in [Belanger et al., 2010] is the array scattering from the piezoelectric A0 Lamb wave transducers bonded to a plate, which correspond to a localised thickness change and interferes with the ability to attribute the scattered wave field to the defect by the imaging algorithm. Physically this means that the scattering from the transducers generates (coherent) noise that masks the scattering from the defect and thus negatively influences the thickness reconstruction. This problem of transducer array scattering can be overcome by utilising contactless transduction, which can be achieved with, for example, electromagnetic acoustic transducers (EMATs) [Hirao and Ogi, 2003]. The contactless nature of EMATs allows for applications in high temperature environments and the inspection of fast moving media, such as rolled sheet metal. Nonetheless, the EMAT may still be in physical contact with the test specimen, for example due to the pull force of the permanent magnet when placed on a steel plate, and cause guided wave scattering, even without the presence of a coupling agent. However, in the absence of a coupling agent and for thick plates, such as the ones considered here, the effect of guided wave scattering is expected to be minimal, due to the large inertia and stiffness of the specimen. Besides the contactless transduction ability, measurements with EMATs are generally very reproducible and in comparison to piezoelectric transducers do not require a coupling agent to couple the ultrasonic field generated by the transducer into the test specimen. The main limitations of EMATs are their ability to only operate on materials with “good” electric conductivity, such as metals, making them infeasible for wave excitation in some modern engineering materials such as many composites and plastic. Another major limitation of EMATs is their often low signal-to-noise ratio. However, for guided wave tomography applications the ability to avoid transducer scattering prevails and makes them invaluable. Therefore, the focus here is extended to developing a selective A0 EMAT.

An EMAT usually consists of two main components, an induction coil and a permanent magnet that are arranged as to excite the desired wave type. For the generation of low frequency omni-directional A0 Lamb waves, a design is illustrated in Figure 1.1. Note that this design can also be adapted to excite S0 Lamb waves by changing the geometrical parameters [Wilcox et al., 2005]. In Figure 1.1, a pancake coil is placed above the specimen surface and is driven by an alternating current, inducing eddy currents in a skin depth layer within the conductive specimen. The permanent magnet is located coaxially above the pancake coil and provides a bias magnetic field that penetrates into the specimen. The interaction of the dynamic magnetic field of the eddy currents and the bias magnetic field of the permanent magnet produces a force, which gives rise to elastic waves in the specimen. In reception, the elastic wave generates an electromotive force by interacting with the bias magnetic field that induces a voltage in the induction coil of the receiving EMAT and can be measured at the terminals of the coil.

The aim of this project is to develop and test an EMAT based guided wave tomography system using the A0 Lamb mode. For that, in a first step the EMAT is developed and then integrated into the prototype of a guided wave tomography system. The development of

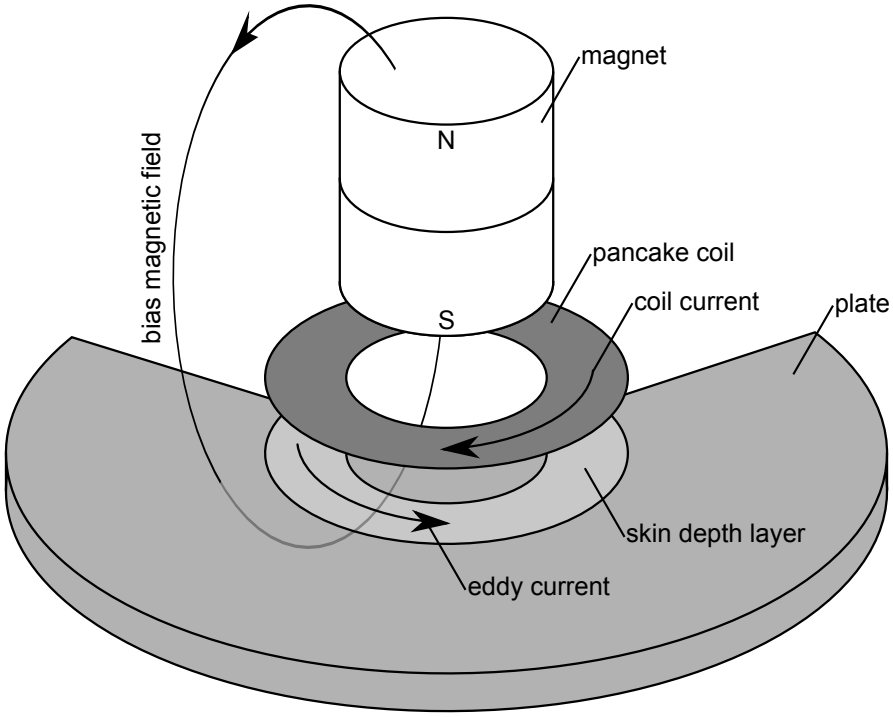

Figure 1.1: Design concept of an omni-directional, low frequency, Lamb wave EMAT, showing the permanent magnet and the induction coil. The skin depth layer, the direction of the magnetic field, the coil and induced eddy current are illustrated.

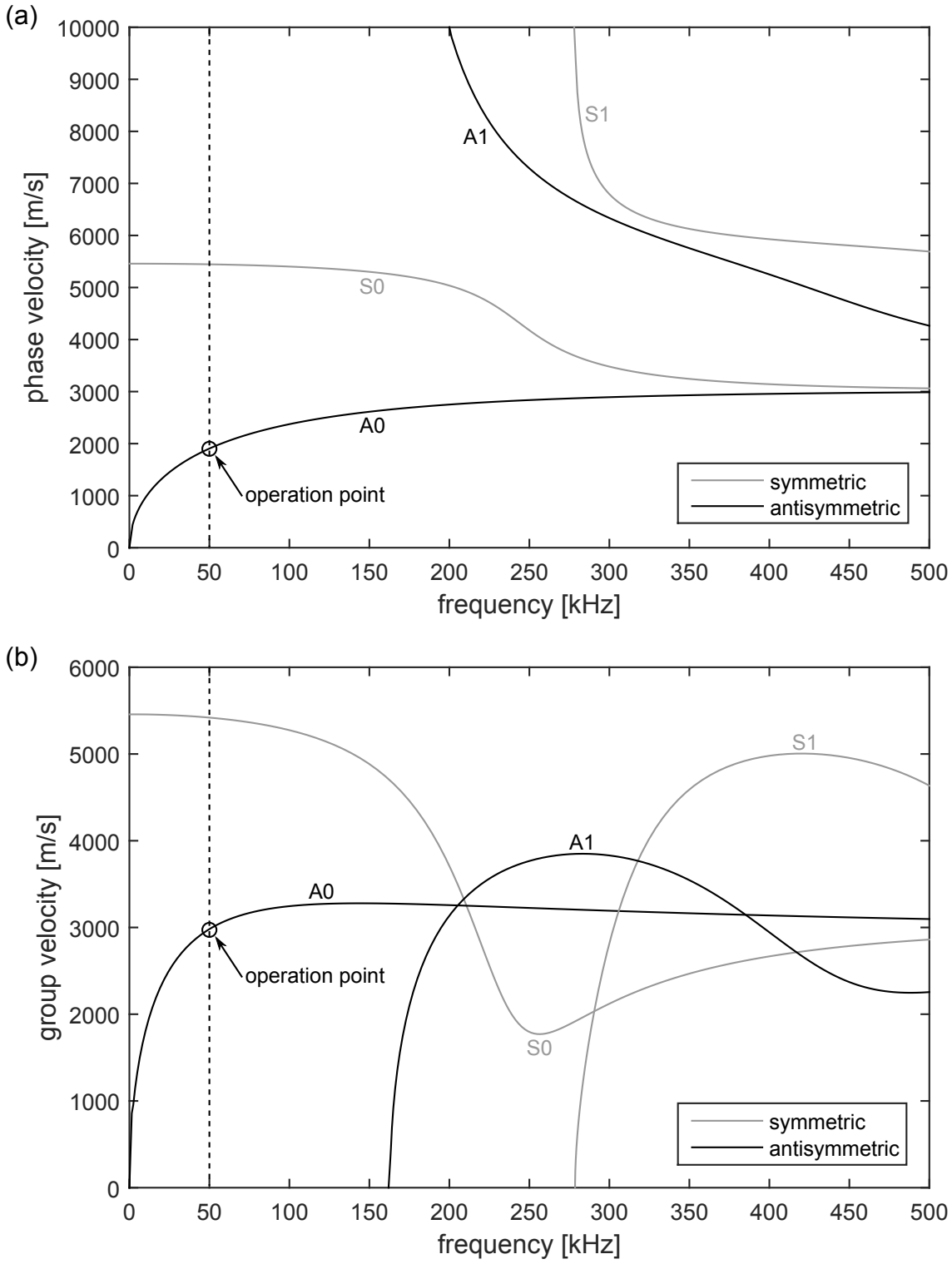

Figure 1.2: Dispersion curves for a 10 mm thick steel plate, illustrating the phase velocity (a) and the group velocity (b). The dispersion curves are computed with DISPERSE [Lowe and Pavlakovic, 2013] and the operation point of the guided wave tomography system is marked.

an EMAT based on the design concept of Figure 1.1 demands a set of design requirements that need to be fulfilled, in order for the EMAT to be useful for A0 Lamb wave tomography. Firstly, the frequency operation point for the EMAT is given by the operation point of the tomography system and is chosen to be at a frequency of 50 kHz on a 10 mm thick plate. This is illustrated in Figure 1.2, where the dispersion curves for the lower order Lamb modes in a steel plate are shown and the reasons for this operation point are discussed in [Huthwaite et al., 2013a]. Also, as seen from Figure 1.2, at the designated operation point, there are two modes present, the A0 and the S0 mode. The S0 mode exhibits a much greater group velocity, which implies that any excited S0 waveform will arrive before the A0 waveform. Since any scattered and reflected components of a wave typically arrive after the main wave packet, this means that these components of the S0 waves may corrupt the main A0 signal. For that reason, a target S0 suppression of approximately 30 dB in relation to the A0 mode, measured for an EMAT to EMAT send-receive setup, is required, as this will push the S0 amplitude to the order of the noise of a typical EMAT system. Lastly, the EMAT is required to work on steel, which is a ferromagnetic material and therefore requires additional consideration in the development.

One aspect that needs to be considered in the development of the EMAT is the duality of mode selectivity and sensitivity (signal-to-noise ratio). While the mode selectivity is given by how pure the EMAT excites the A0 over the S0 mode, the sensitivity regards how well either can be detected relative to the noise. Here, mode selectivity prevails over sensitivity and potential sensitivity issues may be overcome with more powerful measurement electronics. The sensitivity may be additionally enhanced by tuning for example the coil geometry, the coil impedance, which is a topic of on going research, or specialised magnetic flux shaping to increase the magnetic flux density in the eddy current layer (such as in [Koch et al., 2008]).

The EMAT, which is optimised for the A0 Lamb wave transduction, is incorporated as the key component into the guided wave tomography system prototype. The guided wave tomography system is engineered for the efficient acquisition of the tomography measurements of all necessary send-receive combinations, by employing a multi-channel design. The main requirement is the computer controlled data acquisition, which allows for unsupervised data capture. The development process of the prototype system regards two aspects, the hardware and software development. The hardware development includes the definition of the necessary components, their commission and implementation in the prototype. The

software development includes the definition and implementation of various aspects, such as the data management and program flow, as well as controlling the various hardware components. The prototype of the guided wave tomography system is tested and the best parameters for data acquisition are defined, to allow for tomography measurements.

The developed guided wave tomography system is used to inspect various scenarios of areas with restricted access, with the aim to study and understand possible limitations that are imposed by those areas onto the feasibility of guided wave tomography using the A0 mode. The experiments are conducted on a steel pipe and two artificial and smoothly varying defects are considered in the experimental studies presented here. Such a defect represents a favourable target for the tomography algorithm employed here and allows therefore for a better understanding of the influence of restricted areas, rather than the joint influence of the area of restricted access and resolution limitations. The joint influence is for example studied in [Volker et al., 2015], where a field trial on support locations is presented, based on an EMAT based guided wave tomography system and employing the S0 mode. The emphasis there is to show the feasibility of guided wave tomography for the inspection of support locations, given their EMAT system. The research presented here differs from that presented in [Volker et al., 2015] by analysing the influence of various regions with restricted access onto the thickness reconstructions relative to a reference measurement in a controlled environment.

Additional to the inspection of areas with restricted access, various experimental studies and studies based on numerically altered experimental data around the repeatability and robustness of measurements regarding sensor position errors are conducted. These practical aspects are vital to assess the performance of the guided wave tomography system and the necessary precision in the operation of the guided wave tomography system.

As part of a larger long-term programme for the development of guided wave tomography in the field of non-destructive evaluation, this research project draws from the advances made within the larger project, which namely include the selection of the Lamb mode [Huthwaite et al., 2013a], the development of the tomography algorithm [Huthwaite, 2012] and the system calibration [Huthwaite, 2012]. The research presented here represents the practical implementation of the previous findings in form of a prototype system, employing the various algorithms for the tomographic inversion (without modifications), to provide a tool for the

experimental testing of the performance of the previously developed tomography algorithms for various inspection scenarios.

1.2 Thesis Outline

In this research project a guided wave tomography system based on the A0 Lamb mode and using EMATs is developed and experimentally tested.

In Chapter 2, the development process of the guided wave tomography system is illustrated. The focus there is on the development of the A0 Lamb wave EMAT with the requirements presented earlier and a model-based design approach is proposed, which represents one of the novelties of this research project. The development of the sensor is based on a numerical optimisation of a parametric finite element model, which is experimentally validated based on a prototype sensor of the optimised design. Further, the integration of the sensor prototype into the guided wave tomography system is then presented.

Chapter 3 studies the influence of various practical issues on the thickness reconstructions when operating the developed guided wave tomography system. The studies presented are based on experimental measurements and numerically altered experimental measurements and concern with repeatability and robustness of the thickness reconstructions. Further, an advanced signal processing technique is presented to enhance the data acquisition speed.

Chapter 4 looks at the inspection of areas with restricted access, using the developed guided wave tomography system. For that, experimental tests are conducted on life sized pipe specimens, considering three areas of interest, support locations, pipe clamps and STOPAQ(R) coatings, where the influence of the presence of these restrictions to access on the thickness reconstructions is studied, which represents another novelty of this research project.

The last chapter gives a summary of all findings and points towards possible future research opportunities.

Chapter 2

Guided Wave Tomography System Development

One of the key components of the tomography system is the EMAT, which has to fulfil the requirement of contactless transduction and mode selectivity. In this chapter, the development process of the EMAT sensor is illustrated, as well as the integration of the sensor into the tomography system. The main novelty of this chapter lies in the EMAT development and the model-based EMAT design approach, as well as the physical implementation of the guided wave tomography system.

At first, the theory of EMAT transduction and guided waves is presented followed by the model-based EMAT development and the integration of the EMAT into the tomography system.

2.1 Theoretical Background

The development process of the guided wave tomography system requires some knowledge of the physics involved. In this section, first an introduction to electromagnetism and the electromagnetic-acoustic interaction is given, which describes the operating principle of how an EMAT generates elastic waves. Further, the theoretical background of Lamb waves are

presented, as these are the type of elastic waves that are being exploited by the tomography system.

2.1.1 Electromagnetic Acoustic Interaction

In the field of electromagnetic acoustic transduction, electromagnetic and elastodynamic domains are coupled to produce stress waves from the changes of the electromagnetic field quantities. In the following, the derivations are based on [Moon, 1984], [Jackson, 1998], [Jiles, 1998] and represent a brief overview of the mathematical treatment of the electromagnetic acoustic coupling. The variables in bold font denote vector/tensor quantities, whereas regular fonts represent scalar quantities.

2.1.1.1 Maxwell's Equations

In an electromagnetic continuum, there are several quantities that are attributed to material domains. These are the charge density ρ_V, the current density $\mathbf{J}$, the polarization density $\mathbf{P}$ and the magnetization density $\mathbf{M}$. The interaction of multiple material domains distributed in space is established via auxiliary quantities that may permeate all space, outside and within a material domain. The auxiliary variables are the magnetizing field (alternatively auxiliary magnetic field) $\mathbf{H}$, the magnetic flux density (magnetic field, magnetic induction) $\mathbf{B}$, the electric field $\mathbf{E}$ and the electric displacement field (electric flux density) $\mathbf{D}$. The auxiliary quantities $\mathbf{H}$, $\mathbf{B}$, $\mathbf{E}$, $\mathbf{D}$ are related to the material quantities (ρ_V, $\mathbf{J}$, $\mathbf{P}$, $\mathbf{M}$) through constitutive relationships.

The mathematical relationship between the auxiliary quantities is governed by Maxwell's equations, which is a set of partial differential equations consisting of Ampère's law (with Maxwell's correction), Faraday's law, Gauss' law and Gauss' magnetism law. These can be given in either the integral (balance law) or differential form (as a localisation of the integral form under the application of various vector identities). Here, the differential representation of Maxwell's equations is chosen as presented in [Moon, 1984],

$$\nabla \times \mathbf{H} = \mathbf{J} + \frac{\partial \mathbf{D}}{\partial t}, \tag{2.1}$$

$$\nabla \times \mathbf{E} = -\frac{\partial \mathbf{B}}{\partial t}, \tag{2.2}$$

$$\nabla \cdot \mathbf{D} = \rho_V, \tag{2.3}$$

$$\nabla \cdot \mathbf{B} = 0 \tag{2.4}$$

Equation (2.1) denotes Ampère's law with Maxwell's correction (or Maxwell's generalisation of Ampère's law) and equation (2.2) Faraday's law. Equation (2.1) implies that a change in the current density or temporal change in the electric flux density gives rise to a solenoid magnetic field and equation (2.2) that a temporal change in the magnetic flux density gives rise to a solenoid electric field. Equation (2.3) represents Gauss' law and states that the total electric flux density passing through a surface is equal to the charge within the volume that is contained by the surface. Equation (2.4) is known as Gauss' law of magnetism and requires that the magnetic flux density is a rotational vector field, as its divergence is zero. As a consequence from that and unlike its electrical equivalent, there are no magnetic monopoles/charges.

The treatment of interfaces between two materials or a material and vacuum requires the definition of boundary conditions to ensure the continuity of the electromagnetic field quantities. These may be formulated mathematically where the numbered subscripts denotes the material number such that

$$\mathbf{D_1} \cdot \mathbf{n} + \mathbf{D_2} \cdot \mathbf{n} = Q_s, \tag{2.5}$$

$$\mathbf{E_1} \times \mathbf{n} + \mathbf{E_2} \times \mathbf{n} = \mathbf{0}, \tag{2.6}$$

$$\mathbf{B_1} \cdot \mathbf{n} + \mathbf{B_2} \cdot \mathbf{n} = 0, \tag{2.7}$$

$$\mathbf{n} \times \mathbf{H_1} + \mathbf{n} \times \mathbf{H_2} = \mathbf{K}. \tag{2.8}$$

In equations (2.5) to (2.8), $\mathbf{n}$ denotes an outward pointing normal vector on the interface between the two different materials. From equation (2.5) it is found that the electric flux density passing through the surface is equal to the charge distribution in the interface Q_s and from equation (2.6) that the in-interface component of the electric field is continuous. Equation (2.7) states that the normal component of the magnetic flux density is continuous across the interface, whereas from equation (2.8) it can be seen that the in-interface component of the auxiliary magnetic field is equal to the surface current density $\mathbf{K}$ in the interface.

2.1.1.2 Electromagnetic Constitutive Relationships

In order to solve Maxwell's equations, a set of constitutive relationships are necessary to reduce the number of unknowns. The constitutive relationships relate electromagnetic quantities to material properties such as the magnetization density $\mathbf{M} = \mathbf{M}(\mathbf{H})$, polarization density $\mathbf{P} = \mathbf{P}(\mathbf{E})$ and current density $\mathbf{J} = \mathbf{J}(\mathbf{E})$ and are generally nonlinear. It needs to be noted that the material dependent electromagnetic properties may depend on both the electric and magnetising fields, however, for the materials considered here this does not apply. For the case of a linear, isotropic and stationary material, the constitutive relationship for a dielectric material can be written as

$$\mathbf{P} = \epsilon_0 \eta \mathbf{E} \quad \text{or} \quad \mathbf{D} = \epsilon_0(1+\eta)\mathbf{E} = \epsilon_0\epsilon_r\mathbf{E} = \epsilon\mathbf{E}. \tag{2.9}$$

Equation (2.9) relates the polarization density to the electric field via the electric susceptibility η or the electric flux density to the electric field via the electric permittivity ϵ. The electric permittivity can be given as the product of the relative permittivity ϵ_r, which is a material property and the permittivity in vacuum ϵ_0, which approximately takes the value of $\epsilon_0 \approx 8.854 \times 10^{-12}\,\mathrm{F/m}$. The relative electric permittivity is sometimes given as a function of the electric susceptibility such that $\epsilon_r = (1+\eta)$, as seen from equation (2.9). In the EMAT application considered here, the dielectric phenomenon is not regarded such that $\epsilon_r = 1$ is assumed and its constitutive relationship is only given for completeness.

In case of a linear, isotropic and stationary magnetic materials the constitutive relationship may be given as

$$\mathbf{M} = \chi\mathbf{H} \quad \text{or} \quad \mathbf{B} = \mu_0(1+\chi)\mathbf{H} = \mu_0\mu_r\mathbf{H} = \mu\mathbf{H}. \tag{2.10}$$

Equation (2.10) gives the magnetisation density in terms of the magnetising field via the magnetic susceptibility χ or the magnetic flux density as a function of the magnetising field via the magnetic permeability μ. The magnetic permeability can also be given as the product of the material-dependent relative permeability μ_r and the magnetic permeability of vacuum μ_0, which takes the value of $\mu_0 = 4\pi \times 10^{-7}\,\mathrm{Vs/Am}$. The relative magnetic permeability is sometimes given as a function of the magnetic susceptibility such that $\mu_r = (1+\chi)$, as seen from equation (2.10).

For non-magnetic materials the relative permeability μ_r is equal to unity, however, for

magnetic materials the relative permeability diverges from unity. Magnetic materials can be roughly classified into ferromagnetic and non-ferromagnetic materials, with the difference being that ferromagnetic materials exhibit the capability to retain magnetization even after an external magnetic field is removed. Ferromagnetic materials are for example Nickel, Cobalt, Iron and some of their alloys (carbon steel, etc.).

Non-ferromagnetic materials can be divided into two groups, paramagnetic and diamagnetic. In the latter case, diamagnetic, the material responds to an external field by aligning the magnetization in the material opposite to that of the external field. These materials have a relative magnetic permeability $\mu_r < 1$ (or a magnetic susceptibility $\chi < 0$), such as for example silver $\chi = -2.02 \times 10^{-6}$ or copper $\chi = -0.77 \times 10^{-6}$ (values from [Jiles, 1998]). Paramagnetic materials respond to an external magnetic field by aligning the magnetization in the same direction as the external magnetic field and have a relative magnetic permeability $\mu_r > 1$ (magnetic susceptibility $\chi > 0$). An example of a paramagnetic material is aluminium with $\chi = 1.65 \times 10^{-6}$ (value from [Jiles, 1998]). Paramagnetic and diamagnetic materials generally exhibit a relative magnetic permeability of around unity and can be modelled using equation (2.10).

Ferromagnetic materials are able to retain magnetisation, even when the external field is removed and also feature a saturation magnetisation. They can be distinguished into soft and hard ferromagnetic materials, based on the area of the hysteresis loop of their magnetisation curves (BH-curves). For small areas of the hysteresis loop, the material is termed soft ferromagnetic and can be modelled mostly according to equation (2.10) for small magnetising fields (no magnetic saturation occurs). In comparison to non-ferromagnetic materials, the relative permeability may be several orders of magnitude larger. Hard ferromagnetic materials, on the other hand, are characterised by their large area of the hysteresis loop. For small magnetising fields (no magnetic saturation), these can be modelled as

$$\mathbf{B} = \mu_0(1+\chi)\mathbf{H} + \mathbf{B_r} = \mu_0\mu_r\mathbf{H} + \mathbf{B_r} = \mu\mathbf{H} + \mathbf{B_r}, \tag{2.11}$$

where $\mathbf{B_r}$ represents the remnant magnetic flux density. In the following, any ferromagnetic material is modelled with a strong paramagnetic approximation (following equation (2.10) or (2.11)) for simplicity and due to the vast uncertainties in accurate material parameters.

The current density $\mathbf{J}$ is related to the electric field $\mathbf{E}$ via Ohm's law such that

$$\mathbf{J} = \sigma \mathbf{E}, \tag{2.12}$$

where σ is the electric conductivity of the material domain. Typical values for μ_r, ϵ_r and σ are for example listed in [Moon, 1984], [Jiles, 1998].

2.1.1.3 Quasi-static Approximation for EMAT modelling

For EMAT applications, the magneto-quasi-static approximation of the Galilean limit [Bellac and Levy-Leblond, 1973] of Maxwell's equations can be employed. The solution to Maxwell's equations yields a propagating wave solution when solved for any frequency, which is caused by the time derivative of the electric flux density $\partial \mathbf{D}/\partial t$ (equation (2.1)) added by Maxwell to Ampère's law. However, for frequencies below 100 MHz and in good conductors [Moon, 1984], this term may be omitted from Maxwell's equations, which then represent a set of parabolic partial differential equations, an example of which is the diffusion equation. In [Moon, 1984] it is shown that in good conductors the free charge density decays to zero virtually instantly (exponentially with an electric charge diffusion time on the order of $\tau \approx 10^{-20}$ s, for example, for steel), due to the high electric conductivity values of the respective material and $\tau \propto 1/\sigma$. Therefore, it can be assumed for the modelling purposes here that any change in the electromagnetic field quantities occurs instantaneously throughout the regarded spatial domain.

The simplification of neglecting Maxwell's correction to Ampère's law mathematically expresses the skin effect as one of the implications of the diffusion equation. The skin effect describes the exponential decay of the electromagnetic quantities due to an alternating electromagnetic field at the surface. The skin depth is defined as in [Moon, 1984] as

$$\delta = \sqrt{\frac{1}{\pi f \sigma \mu}}. \tag{2.13}$$

Equation (2.13) calculates the skin depth δ for a material with conductivity σ and magnetic permeability μ impinged upon by an electromagnetic field at a frequency of f.

With the above assumptions, Maxwell's equations may be given in terms of the magnetic

vector potential $\mathbf{A}$, such that

$$\nabla^2 \mathbf{A} - \mu\sigma \frac{\partial \mathbf{A}}{\partial t} = -\mu \mathbf{J_e}. \tag{2.14}$$

In equation (2.14), $\mathbf{J_e}$ represents the externally applied current density and from the magnetic vector potential, the magnetic flux density ($\mathbf{B} = \nabla \times \mathbf{A}$) and electric field $\mathbf{E} = -\dot{\mathbf{A}}$ may be computed. The induced current density can be given as $\mathbf{J} = -\sigma\dot{\mathbf{A}}$ using Ohm's law. In addition to equation (2.14), for the computation of electromagnetic field quantities, a gauging condition needs to be introduced, such as the Coulomb gauge ($\nabla \cdot \mathbf{A} = 0$).

2.1.1.4 Electromagnetic Forces and Equation of Motion

The interaction of electromagnetic fields with conducting elastic domains gives rise to elastic deformations. The elastic deformations cause changes in the electromagnetic field quantities, making coupling generally bidirectional. However, for EMAT applications, hierarchical coupling can be assumed [Chian and Moon, 1981], as the changes in the electromagnetic quantities due to elastodynamic phenomena are small and so can be neglected. This enables the separation of both domains and in a first step the electromagnetic phenomena can be computed and then the results can be utilized for the determination of the elastic domain excitation. The coupling of the electromagnetic and elastic domain is determined by three major mechanisms [Moon, 1984], [Thompson, 1978].

The first mechanism is the Lorentz force, which describes the forces acting on static and moving charges. However, as the magneto-quasi-static approximation is considered, the net charge density is zero due to the short electric charge diffusion time τ and therefore can be neglected in the force calculation, so that the Lorentz body force becomes

$$\mathbf{f}^L = \mathbf{J} \times \mathbf{B}. \tag{2.15}$$

The second interaction mechanism between the electromagnetic and elastic domains is the magnetization force [Brown, 1953], [Brown, 1966]. The magnetization force can be understood as the forces acting on magnetic dipole moments in the presence of a (spatially

varying) magnetic field. The total magnetization force can be calculated as

$$\mathbf{F}^{mag} = \mu_0(\mu_r - 1)\int_V (\mathbf{H}\cdot\nabla)\mathbf{H}\,\mathrm{d}V + \frac{(\mu_r-1)^2}{2\mu_0\mu_r^2}\int_S B_n^2\mathbf{n}\,\mathrm{d}S. \tag{2.16}$$

Equation (2.16) describes the total magnetisation force acting on the body given as a function of the total magnetising field $\mathbf{H}$ and magnetic flux density $\mathbf{B}$. It is composed of two terms, a volume integral, which relates to the forces in the body due to external and internal sources and a surface integral over the surface of the whole body, which is required due to the discontinuity of the relative magnetic permeability at a material interface. In equation (2.16), the surface integral is expressed in terms of the magnetic flux density to facilitate the computation, as the normal component of the magnetic flux density is continuous across a material interface. This formulation of the magnetisation force assumes a paramagnetic constitutive relationship (equation (2.10)) as an approximation for a ferromagnetic constitutive relationship and it is acknowledged that this may be an oversimplification. One implication of this is that no magnetic saturation occurs in the body and it needs to be ensured that this condition is met. Further, in equation (2.16), ∇ denotes the Nabla or del vector operator and the term in parentheses condenses to a scalar operator due to the dot product between the magnetization $\mathbf{H}$ and the Nabla operator.

The third interaction mechanism is magnetostriction and is a phenomenon that causes dimensional changes (elastic strains) in ferromagnetic materials due to changes in the magnetic state [Lee, 1955]. For EMAT applications [Ribichini, 2011], mostly magnetostriction due to external magnetic fields (Joule magnetostriction) is relevant and generally highly nonlinear [Bozorth, 1951]. It can be represented as a constitutive relationship between the strain and the magnetizing field [Engdahl, 2000]. Magnetostriction is neglected here, as it exhibits vast uncertainties in the material parameters and it is expected that for the EMAT design here would only have a small influence, in accordance with the findings in [Ribichini et al., 2012].

The governing equations for the elastodynamic domain are obtained from the localized version of the balance of linear momentum [Malvern, 1969] (page 500). By assuming a linear isotropic elastic constitutive relationship between the Cauchy stress tensor and the elastic strain tensor, such as Hook's law, the equation of motion of the linear elastic domain

reads

$$(\lambda' + \mu')\nabla(\nabla \cdot \mathbf{u}) + \mu'\nabla^2\mathbf{u} - \rho\frac{\partial^2\mathbf{u}}{\partial t^2} = -\rho\mathbf{f}. \tag{2.17}$$

Equation (2.17) is also known as Navier's equation of motion and λ' and μ' represent the Lamé constants; ρ denotes the mass density and $\mathbf{u}$ the particle displacement and the variable $\mathbf{f}$ denotes the body force acting on the regarded elastic continuum. When only considering the Lorentz force as an excitation mechanism, equation (2.15) can be substituted directly for $\mathbf{f}$. In the case where the magnetisation force is considered, equation (2.16) needs to be adapted slightly, such that the localised version of the volume integral is substituted for the body force $\mathbf{f}$ and the surface integral term represents a traction boundary condition. The body force (with traction boundary condition in case of the magnetisation force) is also the coupling term for a weak coupling between the electrodynamic and the elastodynamic domains.

2.1.2 Guided Waves

Lamb waves [Lamb, 1917] and shear horizontal waves are two possible guided wave types that occur in plates. A plate here refers to a continuum bounded by two parallel planes and has infinite extent in all directions parallel to the bounding surfaces. The plate represents the wave guide and the elastic wave propagates parallel to the bounding planes. Perpendicular to the direction of the bounding planes (thickness direction), the guided wave behaves as a standing wave, which determines its properties (symmetric/antisymmetric/shear horizontal). In the following, a brief overview of Lamb waves is given, as only those are regarded here. A rigorous derivation can be found in for example [Achenbach, 1973] (page 220ff.) or alternatively in [Auld, 1990] or [Rose, 2004].

The mathematical treatment of Lamb waves is based on the homogeneous Navier's equation (2.17). Under a plain strain assumption (infinite plate), the Rayleigh-Lamb frequency equations can be derived by solving the homogeneous Navier's equations for traction-free boundary conditions on the top and bottom surface of the plate. The Rayleigh-Lamb frequency equations describe the dependence of the wave speed on the frequency, which is also referred to as a dispersion curve. There are an infinite number of solution to the Rayleigh-Lamb frequency equations and since they are transcendental, their solution can only be found numerically, for which reason the software DISPERSE [Lowe and Pavlakovic, 2013]

is used to retrieve the dispersion curves.

In Figure 1.2, the dispersion curves for a 10 mm thick steel plate are shown for the lower order symmetric and antisymmetric modes in the frequency range of up to 1 MHz. The Lamb wave modes are numbered from zero onwards and are depicted in ascending order from left to right. From Figure 1.2(a), which shows the phase velocities, it can be clearly seen that only the zeroth order symmetric and antisymmetric modes exist for all frequencies. Higher order modes exhibit a cut-off frequency, where the phase velocity tends towards infinity. In Figure 1.2(b) the group velocity of the Lamb wave modes are shown for the same modes and frequency range. The group velocity exhibits a similar cut-off frequency behaviour as the phase velocity, whereby the cut-offs vanish through zero velocity, with the S0 and A0 mode persisting throughout the whole spectrum and the higher order modes showing a cut-off frequency. Further, as frequency tends to infinity, the phase and group velocity for the zeroth order modes approaches the Rayleigh wave speed of the plate material, whereas for the higher order modes, both phase and group velocity converge to the shear velocity of the material.

2.1.2.1 Concept of Force Shaping

The concept of force shaping here may be understood as a general concept whereby the excitation forces for the elastic wave generation are tailored to match favourable excitation conditions for the targeted Lamb mode, independent of the physical principle which controls the direction of the force generation. By decomposing the applied (body) force into its in-plane and out-of-plane components, the contributions of each component to the various modes can be computed. This approach has been presented in [Achenbach and Xu, 1999] for the excitation of Lamb waves due to a point force excitation. Wilcox et al. [Wilcox et al., 2005] extended these findings to their analytical model of a S0 Lamb wave EMAT operating on aluminium plates.

In EMAT applications, non-negligible body forces only occur in the skin depth layer, which has a frequency dependent thickness given by equation (2.13) and is approximately $\delta = 67\,\mu$m at the designated operation point. This means that for the excitation of a particular Lamb mode, the body forces within the skin depth layer control the mode selectivity. Since the goal of the EMAT development is to preferentially suppress the S0 mode over the A0

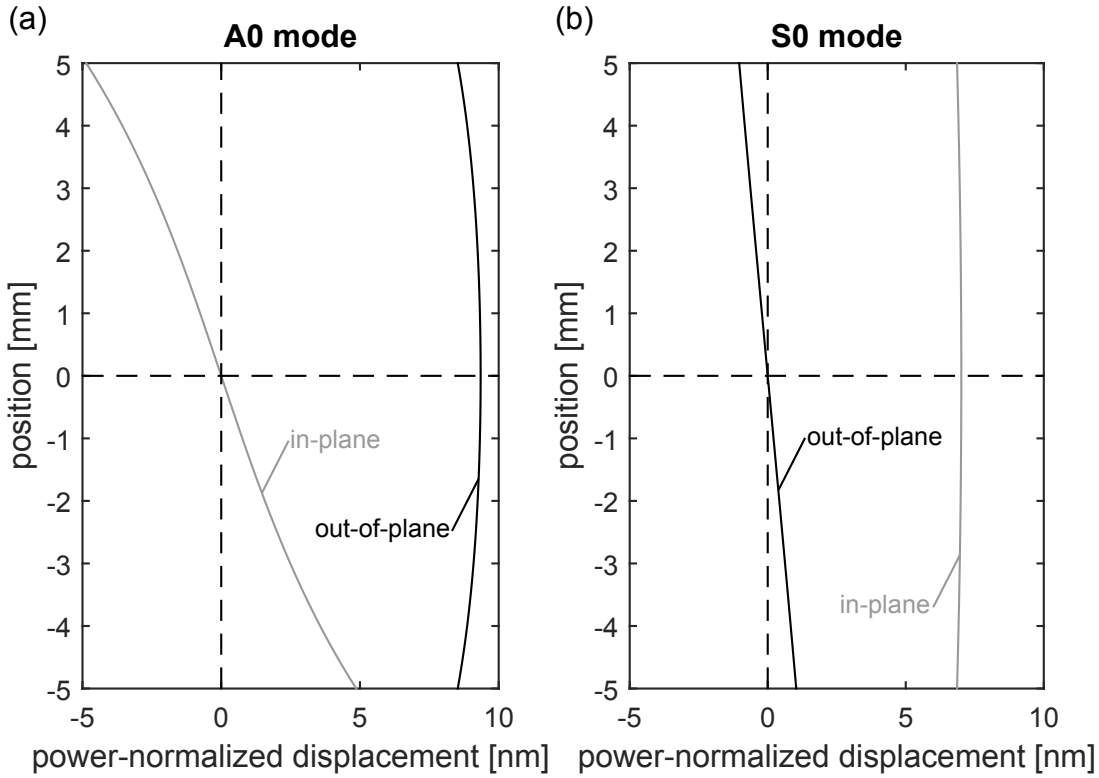

Figure 2.1: In-plane and out-of-plane displacements for a unit power flow for the A0 mode (a) and the S0 mode (b) across the thickness direction of the plate (origin at mid-thickness), shown for an operation point at 50 kHz on a 10 mm thick steel plate (using typical values for material parameters).

mode and because of this, the respective mode shape of each mode must be considered so that the exciting forces generate the A0 mode as purely as possible. In Figure 2.1, the power-normalized mode shapes (in-plane and respective out-of-plane displacements) for the A0 and S0 modes are depicted as a function of the thickness coordinate in the plate for the desired operation point. The power-normalization ensures that the waves have a unit power flow in the direction of propagation and is chosen to enable a direct comparison between the two modes shapes. For the A0 mode, which is pictured in Figure 2.1(a), the out-of-plane displacement clearly outweighs the in-plane displacement. On the other hand, for the S0 mode, which is displayed in Figure 2.1(b), the in-plane displacement is greater than the out-of-plane displacement. The idea of force shaping here is to therefore approximate the ratio of the in-plane and out-of-plane displacements near the surface of the plate (within the skin depth) with a respective body force distribution, typically over a distance of half the wavelength. A second type of force shaping exploits the Poisson effect, whereby the in-plane and out-of-plane components of the excitation force are balanced such that the unwanted mode is suppressed (see also [Nagy et al., 2014]).

For the EMAT application here, the concept of force shaping is realised by tailoring the orientation of the static magnetic field, which controls the orientation of the excitation force distribution. For example for the operation of a low frequency Lamb wave EMATs (design principle illustrated in Figure 1.1) such as in [Wilcox et al., 2005] on an aluminium plate, the direction of the excitation forces within the skin depth layer are always perpendicular to the magnetic flux lines, in accordance with equation (2.15), as the Lorentz force is the only excitation mechanism. The concept of force shaping is applied in the model-based design approach.

2.2 EMAT Development

In this section, the development of the EMAT is presented. At first, an overview of the EMAT model including the various physics and modelling aspects is given, followed by the introduction of the numerical optimization process and the development of an optimization criterion. Further, the optimisation results are presented and a physical prototype is built and tested. The FE model used for the simulations is validated experimentally for the Lorentz force excitation on an aluminium plate and the combination of Lorentz and magnetisation force on a steel plate. A numerical robustness study for two key parameters is conducted and a model-based EMAT design approach is presented.

2.2.1 Model Overview

Figure 2.2(a) shows the layout of the model of the EMAT and represents a cross-section through a symmetry plane of Figure 1.1. The global coordinate reference frame for the model is placed on the upper surface of the plate, as shown in Figure 2.2(a). By exploiting the axisymmetric nature of the EMAT design, a cylindrical coordinate system can be assumed, where the axial direction (z-axis) coincides with the cylinder axis of the permanent magnet. The radial coordinate axis (r-axis) then is parallel to the surface of the plate. This axisymmetric modelling approach dramatically reduces the computational effort, when compared to a fully three-dimensional model, but is clearly unable to represent a domain containing both the transmitting and receiving transducer and will therefore only be used to estimate the performance of the design in transmission. However, the relative sensitivities to A0 and

S0 in reception will be the same as the relative sensitivities when transmitting, provided the values have been power-normalised. The cable-to-cable A0-S0 ratio can therefore be computed by squaring the power-normalised A0-S0 ratio from the transmission case.

Figure 2.2(a) also shows the geometric parameters of the model. Apart from the magnet diameter (d_magnet) and the magnet lift-off from the top of the coil (s_liftoff), which are subjected to optimization, all other parameters are maintained constant at the illustrated values. The inner and outer diameters of the induction coil are taken from [Wilcox et al., 2005], where they match the values for the coil of EMAT VII. It was shown in [Wilcox et al., 2005] that mode selectivity can be controlled by the coil dimensions, such that if the average diameter of the induction coil is approximately half the wavelength of the desired Lamb mode, then the excitation of that mode is maximized. This finding is exploited here, as at the operation point of 50 kHz on a 10 mm thick steel plate, the A0 wavelength is 37 mm, half of which is approximately the average coil diameter of 19 mm. In contrast, the wavelength of the S0 mode is approximately 107 mm at the same operation point and this vast difference in wavelength may significantly contribute to the mode selectivity of the transducer. The number of turns of the induction coil is not included as an optimisation parameter, as

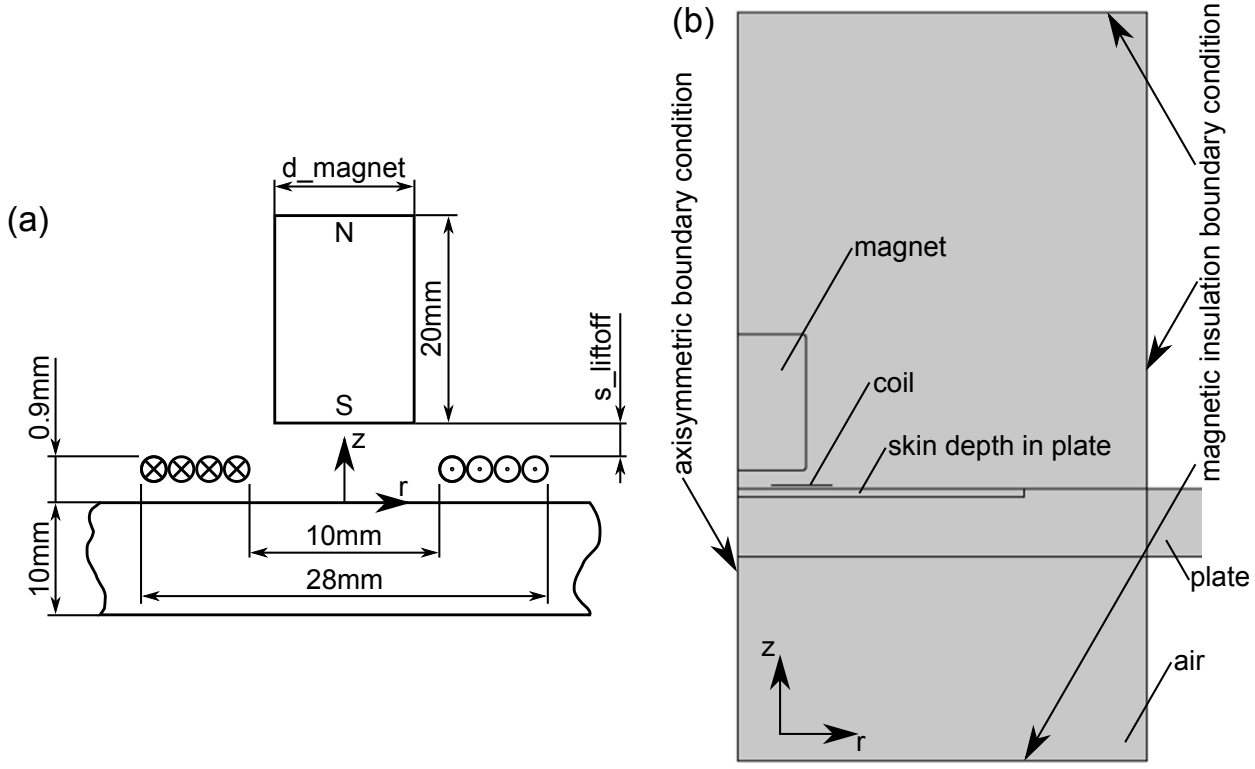

Figure 2.2: Overview of the EMAT model and the various geometric parameters used (a). In (b) the implementation in COMSOL is illustrated.

this only increases the number of optimisation parameters and adds complexity to the optimisation process. In [Wilcox et al., 2005] it has been shown that this parameter only increases the sensitivity of the EMAT with increasing number of turns. Ongoing research, whereby the EMAT transduction process is modelled via a transformer model, suggests that in the light of signal-to-noise ratio computations, the number of turns may be a parameter among others that can be tuned to enhance the EMAT sensitivity in correlation with the measuring electronics.

The model is numerically implemented using the finite element (FE) software COMSOL [COMSOL Inc., 2012] to model and simulate the EMAT under development. The modelling approach employed is adapted from [Ribichini, 2011], where the software COMSOL was used to model and simulate EMATs for shear wave applications, while considering the effects of magnetostriction. In the model in [Ribichini, 2011], the dynamic magnetic field due to the induction coil and the elastodynamics were implemented in the model and the bias magnetic field was assumed to be spatially homogeneous. In [Ribichini, 2011], this model is experimentally validated and, given the similarity to the model proposed here, a realistic behaviour of the model is expected. In contrast to the work in [Ribichini, 2011], this paper additionally implements the bias magnetic field within the model, so that the geometric parameters of the magnet may participate in controlling the mode selectivity between the A0 and S0 modes.

Figure 2.2(b) depicts the EMAT model as it is implemented in COMSOL. In addition to Figure 2.2(a), an air domain is added that engulfs the magnet and the induction coil. The air domain is necessary in order to model the return path of the magnetic flux from the permanent magnet and induction coil outside the steel plate. It should behave as if it is of infinite extent; therefore it is set sufficiently large (60 mm in radial and 110 mm in axial direction) such that the magnetic insulating boundary conditions can be assumed to have a negligible effect on the model across the full range of design parameters, the magnet lift-off and diameter. Further, the air domain is only associated with the electromagnetic physics and so is localized to the transducer part of the model, but is omitted for the plate elsewhere. The omission of the air domain is a common assumption for elastic wave propagation in solids, as the difference in mechanical impedance at the air-to-solid interface is large enough and it can be assumed that no energy is lost to the air domain. This approach also helps to reduce the computational effort, as the elastic wave field does not need to be computed

Table 2.1: Electromagnetic material parameters employed in the FE model.

Material	rel. permittivity ϵ_r	rel. permeability μ_r	el. conductivity σ
Air	1	1	$10\,\mathrm{S/m}$
N42 magnet	1	1.05	$8 \times 10^5\,\mathrm{S/m}$
Steel	1	160	$4.032 \times 10^6\,\mathrm{S/m}$

in the air domain. The edge of the plate, which extends 1.2 m in the radial direction, is terminated with Perfectly Matched Layers (PMLs) [COMSOL Inc., 2012], in order to emulate an infinite extent in the radial direction and avoid end reflections. The application of PML regions is necessary, as the COMSOL simulations are conducted in the frequency domain and therefore edge reflections cannot be avoided by gating off the reflected waves from the time traces, unlike for time domain simulations.

The computation of the bias magnetic field generated by the permanent magnet, as well as the dynamic magnetic field by the induction coil require the material parameters to be defined for the constitutive relationships. The electromagnetic parameters for the various materials involved are listed in Table 2.1. The permanent magnet is modelled as a N42 grade Neodymium-Iron-Boron magnet (material parameters taken from [Arnold Magnetic Technologies Corporation, 2009]). The constitutive relationship between the magnetizing field $\mathbf{H}$ and the magnetic flux density $\mathbf{B}$ is assumed to be $\mathbf{B} = \mu_0\mu_r\mathbf{H} + \mathbf{B_r}$, where $\mathbf{B_r}$ is the remnant magnetic flux density vector and takes a value of $|\mathbf{B_r}|$=1.3 T in case of a N42 grade magnet. The orientation of the remnant flux density points in the positive z-direction, as within the magnet the magnetic flux lines run from the south to the north pole of the magnet. Further, for the effective relative magnetic permeability of the magnet, the recoil permeability is assumed. The air domain assumes a linear constitutive relationship and the electric conductivity of the air domain is given a very small, non-zero value in order to improve the numerical stability of the COMSOL solver as suggested in [COMSOL Inc., 2012]. The electromagnetic constitutive relationship for the steel plate is also assumed to be linear, with a relative magnetic permeability of $\mu_r = 160$ [Ribichini et al., 2012]. It has been verified that across all possible design parameters there is no magnetic saturation in the steel plate, as this would violate the strong paramagnetic assumption, which is underlying to the magnetisation force computation. The relative electric permittivity ϵ_r for all materials in Table 2.1 is selected as unity because these materials do not exhibit any sort of dielectric behaviour in EMAT applications.

The induction coil, which produces the dynamic magnetic field and induces the eddy currents in the steel plate, is modelled as a surface current. The value for the surface current density K is calculated from the number of turns of the coil N, the coil dimensions illustrated in Figure 2.2(a) and the electric current I in the wires such that

$$K = \frac{N}{l} I. \tag{2.18}$$

In equation (2.18), the variable l represents the coil length, which is given by the difference of the outer and inner coil radius. The factor N/l can be regarded as a coil parameter, as it gives the number of turns per unit length of the coil, assuming constant wire spacing. The coil modelled in this paper, which is taken from the coil of EMAT VII in [Wilcox et al., 2005], has 46 turns in two layers on a printed circuit board (PCB) and leads to a factor of N/l=2.55 1/mm. For the simulations, the coil current I is set to 1 A and the model is solved in the frequency domain.

The boundary conditions for the electromagnetic model are illustrated in Figure 2.2(b) and a magnetically insulating boundary condition ($\mathbf{n} \cdot \mathbf{B} = 0$) is assumed for the edges of the air domain, including the edge of the steel plate. The axis of symmetry is also modelled with a magnetically insulating boundary condition (symmetry boundary condition). The discretization of all domains of the FE model is achieved using quadratic triangular elements and the same mesh is used for both the static magnetic simulation of the bias magnetic field as well as for the dynamic magnetic field of the induction coil. The region of interest in the FE model is the skin depth layer, as illustrated in Figure 2.2(b) and represents the coupling region between the electromagnetic and elastodynamic physics. In this region the mesh density is extremely high, in order to correctly approximate the electromagnetic-elastodynamic interaction. A convergence study on a single wire over a half space FE model using COMSOL has been conducted in [Ribichini, 2011] by comparing the numerical results to an analytical solution given in [Chari and Reece, 1974]. It is found that at least one element per skin depth is necessary for accurate approximation. Due to the fact that the skin depth decreases with increasing frequency, the element size is determined by the maximum occurring frequency.

The elastic material properties of the plate are selected to be those of steel with a mass density ρ=7850 kg/m^3, Young's modulus E_{Young}=200 GPa and Poisson's ratio $\nu = 0.33$ for

the elastodynamic simulation. The radius of the plate is chosen as 1.2 m, allowing the complete separation in the time domain of the S0 and A0 Lamb wave modes for a five cycle Hann-windowed tone burst centred at 50 kHz, when measured on the top surface of the plate. The centre line of the EMAT model (z-axis in Figure 2.2(a)) is the axis of axisymmetry and thus by definition the nodes on this line are fixed in the radial displacement, which represents the boundary condition on this line. For the other three sides of the plate, traction-free surface boundary conditions are implemented (with the exception where the surface traction of the magnetisation force acts). The plate domain is discretized with quadratic triangular elements and the maximum element size is 1 mm, which corresponds to less than 1/30 of the wavelength for the A0 mode at 50 kHz and has been shown to be sufficient in [Drozdz, 2008]. The accuracy of the elastodynamic physics at this discretization level is verified by comparing the phase velocity to the results from DISPERSE [Lowe and Pavlakovic, 2013] and a discrepancy of less than 1% is found [Drozdz, 2008], rendering the discretization fine enough.

The time domain data for the evaluation of the simulation results is recovered using the method of Fourier synthesis, since all simulation with the exception of the bias magnetic field are conducted in the frequency domain. The idea of Fourier synthesis is to use the frequency domain dataset that is computed by COMSOL to calculate the desired signal at all frequencies, then perform an inverse Fourier transform to obtain the time domain signal. In theory, to account for the input signal, the Fourier transform of the input must be taken and each component is applied as a source to the frequency domain FE model. However, in practice this can be by-passed by applying a unit source at all frequencies, running the COMSOL model, then multiplying by the source values at the end, prior to the inverse Fourier transform, which exploits the linearity of the system to generate the same result. With the goal to minimize the computational effort of the simulations, the frequency dataset computed from the FE model is band limited in the frequency domain to reduce the number of frequency evaluation points. However, it is to be remarked that besides the band limits, the sampling rate and the length of the zero-padded input waveform also determine the number of frequency evaluation points. The band limits are determined by regarding the Fourier transformation of the input toneburst and for example for a five cycle Hann-windowed toneburst, as considered here, it is found that it is sufficient to include only frequencies within the main and first side lobes of the amplitude spectrum. The accuracy of

the band limited input toneburst has been determined in a convergence study by regarding the root mean square (RMS) of the difference of the time domain signals between the band limited and the full spectrum case. With increasing bandwidth, this RMS value drops, approaching zero asymptotically and accuracy is defined based on the change in the RMS. For a centre frequency of 50 kHz this corresponds to a frequency band of 20 kHz to 80 kHz.

The electromagnetic simulation results of the bias magnetic field simulation and dynamic magnetic field simulation are used in a third step to compute the Lorentz body force, using equation (2.15) and the magnetization force, using equation (2.16), which act on the steel plate in the elastodynamic physics within the skin depth layer. The force calculation of the Lorentz force utilises the current density given by the simulation of the dynamic magnetic field of the induction coil and the magnetic flux density given by the simulation of the static magnetic field of the permanent magnet. The magnetisation force expressed by equation (2.16) describes the total force acting on the steel plate and is implemented in the FE model as a body force given by the argument of the volume integral, as well as a surface traction given by the argument of the surface integral. The traction force acts on the top surface of the skin depth region of Figure 2.2(b). For the computation of the body and traction forces, the electromagnetic field quantities are assumed to be the sum of the static and dynamic simulations and only the terms that yield contributions at the regarded frequency are considered. Further, it is assumed that the electromagnetic forces deform the steel plate and their reaction forces are countered by a rigid permanent magnet that is fixed to the inertial frame.

2.2.2 Optimisation Overview

The optimization process aims to improve the mode selectivity of the A0 mode over the S0 mode at the desired operation point. The mode selectivity here is controlled by the magnet diameter and the magnet lift-off, which determine the spatial variation of the bias magnetic field and therefore the force distribution in the skin depth layer and further the wave excitation.

The influence of the direction of the exciting forces on the mode selectivity is discussed by Nagy et al. in [Nagy et al., 2014] for a simplified case, in order to better illustrate the concept of S0 suppression. For the derivations in [Nagy et al., 2014], only the Lorentz

force is considered, which is modelled via a traction cone. The whole magnetic effect is not modelled and is disregarded for the discussion, as the emphasis is on the mode selectivity. One of the conclusions is that for certain angles between the traction force and the surface normal of the specimen, there exists a clear maximum in the A0-S0 ratio due to reduced excitation of the S0 mode, which is explained by the Poisson effect. Further, time traces from two different EMAT designs, one without and one with optimised traction forces, are presented and used to experimentally demonstrate the feasibility of the mode selectivity enhancement. For the design regarded here, it is expected that there should similarly be an optimum and that this should be found by the numerical optimization process. Additionally to [Nagy et al., 2014], here the influence of the magnetic permeability is considered and for the wave excitation, a body force (and a surface traction in case of the magnetisation force) is assumed.

The optimization process requires a measure for the performance or fitness of every candidate design. The idea for the performance evaluation here is to relate the amplitude of the transmitted A0 Lamb mode to that of the S0 Lamb mode. Here, the performance metric γ is introduced and represents the ratio of the amplitudes of the A0 and S0 modes expressed in [dB], such that

$$\gamma = 20 \log_{10} \left(\alpha \frac{A_0}{S_0} \right)^2 . \tag{2.19}$$

Equation (2.19) describes the cable-to-cable A0-S0 ratio and the A0 and S0 amplitudes are determined by exploiting the different symmetries of the mode shapes on the neutral line of the plate (at mid thickness); the A0 amplitude there corresponds to the out-of-plane displacement (z-axis), whereas the S0 amplitude to the in-plane displacement (r-axis). The power-normalisation coefficient α is defined as the ratio of the power-normalised S0 and A0 amplitudes and can be determined from Figure 2.1 at mid thickness. There the in-plane S0 amplitude is devided by the out-of-plane A0 amplitude yielding α, which takes a value of $\alpha = 0.752$ at the operation point of 0.5 MHz-mm on the steel plate.

Another point to consider for the choice of the performance criterion is the distance to the transducer centre as in the near field of the transducer, the performance of the EMAT may be different than in the far field. For this, Figure 2.3 illustrates the performance metric γ as a function of the radial coordinate (r-axis in Figure 2.2(a)), for the excitation with only the Lorentz force and the joint excitation of Lorentz and magnetisation forces. Also,

the performance is depicted for computations based on the time-domain data (obtained via Fourier synthesis) and frequency domain data (at centre frequency). From Figure 2.3 it can be seen that for large enough distances away from the origin of the reference frame (in the far field), the performance index reaches a steady value. For the computation of the performance index γ, the far field is arbitrarily defined as starting at a radial coordinate of 0.1 m, as the performance already has reached a steady value then. Further, this is also approximately the wavelength of the S0 mode at the given operation point. The computation of the A0-S0 ratio is then achieved by spatially averaging the A0-S0 ratio over the far field region with the goal of a more robust performance measure as compared to a single point, which may be subjected to small variations.

A further observation from Figure 2.3 is that the A0-S0 ratio for both frequency and time domain simulations match in the far field and most of the near field for both the excitation with the Lorentz force, as well as the excitation with both the Lorentz and magnetisation force. The evaluation of the time domain data to determine the amplitudes of the A0 and S0 mode relies on the maximum value of the wave envelope for the respective time trace, whereas for the frequency domain, merely the absolute value of the complex spectral amplitude is considered. It is important to distinguish between the evaluation based on time and frequency domain, because the computation of the time domain dataset is significantly more computationally expensive than a single frequency domain computation. Therefore, as both time and frequency domain evaluations match well in the far field, all computations are carried out in the frequency domain at the operation frequency for the optimisation.

The major drawback of the performance criterion γ is the fact that the optimisation searches for the largest amplitude difference between the A0 and S0 mode as a function of the design parameters only. However, the (absolute) mode sensitivity is not explicitly considered and is of importance for practical realisation of an optimised design.

The realization of the optimization process is achieved by employing a genetic algorithm [Winter, 1995]. The genetic algorithm represents a heuristic search technique that aims to imitate the evolution of a species. It is a non-gradient based technique and as such has the advantage that an analytical derivative of the performance function with respect to the design variables is not required, when compared to gradient based methods. The derivative can be approximated with finite differences for gradient based methods, however, this requires

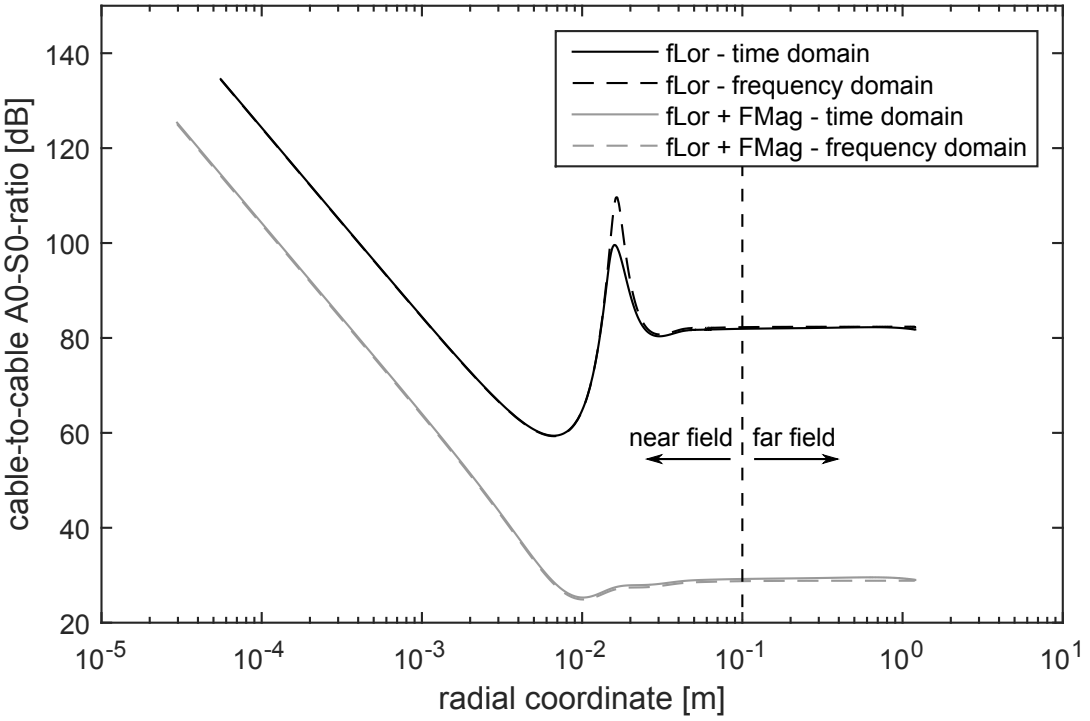

Figure 2.3: Cable-to-cable performance as a function of the radial coordinate calculated on the neutral line of the plate for the excitation with Lorentz force (fLor) and Lorentz plus magnetisation force (fLor+FMag), comparing the time and frequency domain (at centre frequency) performance.

additional evaluations of the performance function, which may be computationally very expensive depending on the performance function. Additionally, gradient based techniques generally conduct a line search in the direction of the steepest gradient or proposed search direction, which again requires further evaluations of the performance function. Here, since each evaluation of the performance function requires a full FE model to be run, gradient based techniques are likely to be computationally intensive. Gradient-based optimizations can also converge to local minima if present in the feasible design space and making them dependent on the initial design. On the other hand, for non-gradient based techniques such as the genetic algorithm, an initial population of several designs is randomly scattered over the whole feasible design space and therefore covering a larger area. However, it needs to be noted that the genetic algorithms may still yield a local minimum as the optimal design rather that the global minimum. In order to avoid finding a local minimum, the optimization is run multiple times to test if the optimized design represents a local or global minimum. The genetic algorithm is selected here, as it requires no prior knowledge of the behaviour of the performance function within the feasible design space and covers large areas of the

feasible design space. A practical advantage of the genetic algorithm is that it is already implemented in the Matlab Optimization Toolbox [The MathWorks Inc., 2012].

2.2.3 Optimisation Results

The software implementation of the genetic algorithm for the optimization process uses the Matlab Optimization Toolbox [The MathWorks Inc., 2012] and a custom fitness function that conducts a FE simulation for every call, returning the respective performance index (see previous section). The optimization is conducted using a population of ten individuals and simulating ten generations, yielding a total of 110 function evaluations, as the initial population (zeroth generation) also needs to be evaluated. However, the optimal design is usually found after approximately five or six generations. The optimization is run on a workstation with two Intel(R) Xeon(R) CPU X5690 at 3.47 GHz with 6 cores and is completed in approximately two hours (for 110 performance function evaluations).

The two design parameters subjected to optimization are bounded to confine the feasible design space to a smaller region and the bounds are set to a practical range: 5 mm to 30 mm for the magnet diameter and 1 mm to 3 mm for the magnet lift-off. At first, only the Lorentz force is considered as an excitation mechanism as it is well characterised and can be reliably calculated. The magnetisation force requires multiple assumptions about the ferromagnetic material properties and this exhibits a large degree of uncertainty. However, it is expected that the magnetisation force will influence the mode selectivity. Also, by only employing the Lorentz force, it is expected that some of the findings from [Nagy et al., 2014] regarding mode selectivity could be recreated for the case of an extended coil, rather than the "single turn coil" regarded by Nagy et al.

The optimisation is run ten times to ensure convergence and it is found that the optimisation

Table 2.2: Optimization results at 50 kHz on a 10 mm thick steel plate based on the excitation with only the Lorentz force for the optimal design and proposed realisation. The cable-to-cable A0-S0 ratio for the case of both the Lorentz and magnetisation force are calculated based on the given magnet diameter and lift-off.

optimisation result	magnet diameter	magnet lift-off	cable-to-cable A0-S0 ratio	
			fLor	fLor+FMag
optimal design	21.05 mm	1.47 mm	83.6 dB	27.3 dB
proposed realization	20.0 mm	2.1 mm	82.1 dB	29.5 dB

converges to the same region for all optimisation runs, implying a global optimum. From the optimization runs it is observed that multiple combinations of magnet diameter and lift-off yield similar performances of better than 75 dB for the A0-S0 ratio within this region. These optima maintain a high A0-S0 ratio for a large variation of the magnet lift-off, while for the magnet diameter are sensitive to slight variations. This implies that the magnet diameter is the dominant design parameter in the optimization (due to this variation) and the gradient of the A0-S0 ratio with respect to the magnet lift-off in the feasible design space is very small. Physically this might be explained with the high magnetic permeability of steel, which causes the magnetic flux lines to strongly alter their direction at the air to steel boundary (continuity of the normal component of the magnetic flux density and tangential component of the magnetising field at interfaces, see equations (2.7) and (2.8)), which may be less susceptible to the lift-off distance than to the magnet diameter. Thus, from all the optimization runs that returned an A0-S0 ratio of better than 75 dB, the one with the highest A0 amplitude in the far field is selected as the global optimum and is listed as the 'optimal design' in Table 2.2. Another observation that can be made from the optimisation is that the optimal magnet diameter is approximately half the wavelength of the A0 mode at the assumed operation point and for the given coil dimensions.

The optimal design, however, requires a magnet with a diameter that is not commercially available. For that reason, the magnet diameter is set to the closest commercially available one (diameter of 20 mm) and then the optimisation is rerun to determine a new magnet lift-off distance, approximately matching the performance of the optimal design. This design is termed 'proposed realisation' in Table 2.2 and is physically implemented for experimental validation of the FE model. Table 2.2 also lists the A0-S0 ratio for the same design parameters, when both the Lorentz and magnetisation force are considered. For the optimal design, the predicted A0-S0 ratio drops to around 27 dB and for the proposed realisation to 29 dB, when the magnetisation force is additionally considered.

Naturally, by looking at the performance drop due to including the magnetisation force into the model, the question arises, whether an optimisation with both excitation forces would lead to an even better design. For this, the A0-S0 ratio is calculated as a function of the magnet diameter for the lift-off of 2.1 mm (proposed realisation) under consideration of both excitation mechanisms. The influence of the lift-off is disregarded here with the argument above of only small changes to the magnetic flux lines due to the change in magnet lift-off.

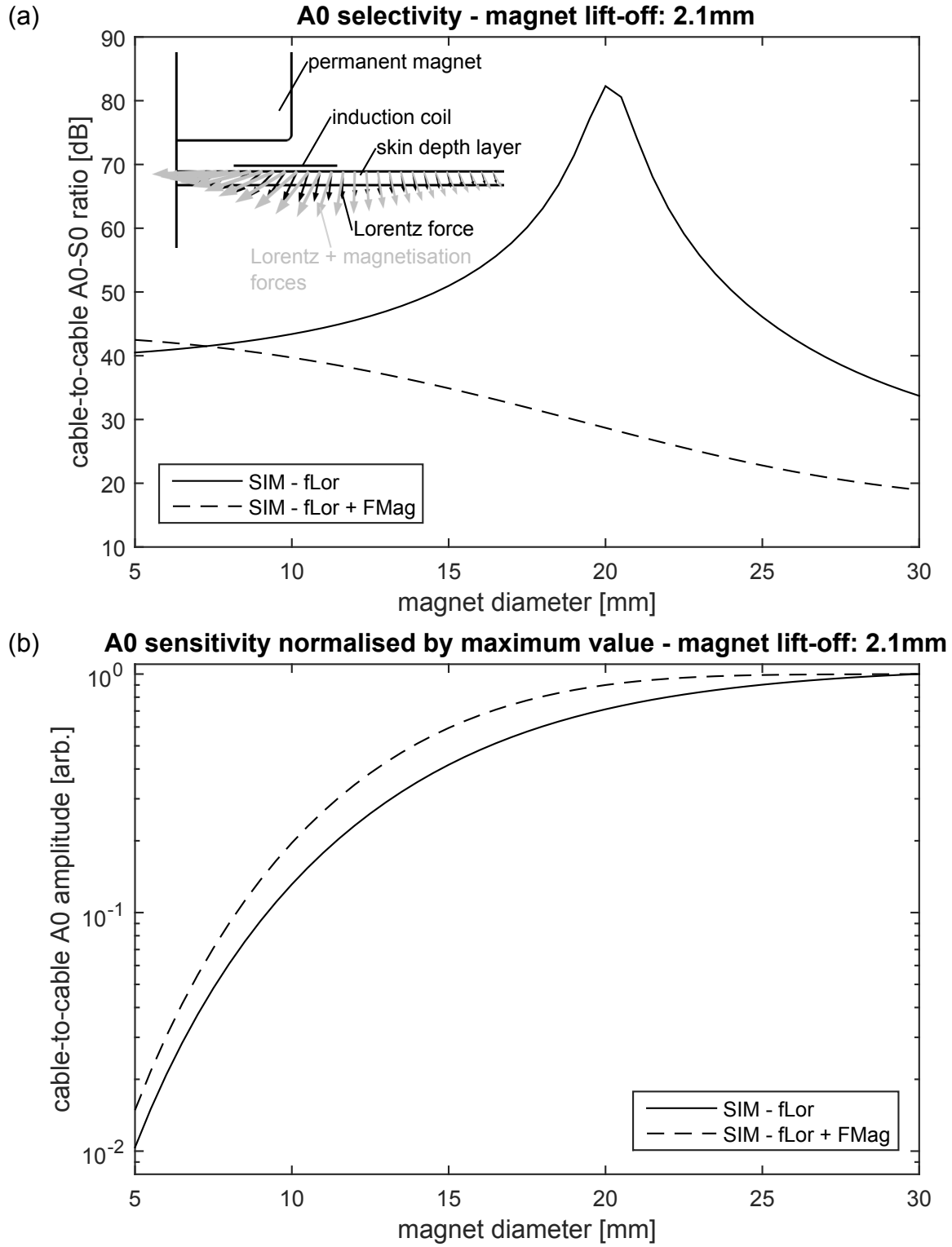

Figure 2.4: Cable-to-cable A0-S0 ratio (a) and normalised cable-to-cable A0 mode sensitivity by maximum A0 amplitude (b) as a function of the magnet diameter for the proposed realisation (Table 2.2). The curve with only the Lorentz force excitations matches with the findings from [Nagy et al., 2014]. The inset in (a) shows the distribution of body forces in the skin depth layer for the proposed realisation from Table 2.2.

The result of this is illustrated in Figure 2.4(a), where it can be seen that for the case of only the Lorentz force excitation, there is a clear maximum at a magnet diameter of 20 mm, as expected. This behaviour of a clear maximum is also observed in [Nagy et al., 2014], where the A0-S0 ratio is studied as a function of the cone angle, which can be controlled via the magnet diameter. The excitation with both the Lorentz and magnetisation force does not exhibit a unique maximum for A0-S0 ratio within the considered interval for the magnet diameter, but takes its largest value at a magnet diameter of 5 mm, which is the lower bound on the range of magnet diameters. There, the mode selectivity is significantly improved compared to that of a 20 mm magnet, however, due to the smaller magnet, the overall A0 mode sensitivity reduces significantly. This can be seen from Figure 2.4(b), where the cable-to-cable A0 mode sensitivity is depicted as a function of the magnet diameter and it can be observed that for a decreasing magnet diameter, the A0 mode sensitivity drops sharply over the range of magnet diameters. This sharp drop in A0 mode sensitivity can be explained with the reduced magnetic flux density within the skin depth layer that reduces the magnitude of the exciting forces. One way to counter the problem of the reduced excitation forces due to a small magnet diameter is to employ a conical flux guide such as in [Koch et al., 2008], where the magnetic flux from a larger magnet is concentrated via a cone to a smaller cross-sectional area. However, this is an additional component and would increase the cost for each transducer, as well as complicate the modelling and optimisation process and therefore is not considered here.

The evaluation of the feasible design space shows that in case of both excitation mechanisms, the performance indeed peaks at the lowest magnet diameter and lift-off and exhibits a smooth decrease in A0-S0 ratio with increasing magnet diameter and lift-off. In contrast, when only considering the Lorentz force, there is a region of high A0-S0 ratio for magnet diameters around 20 mm, which is fairly independent of the magnet lift-off. Outside this region of a high A0-S0 ratio, the A0-S0 ratio drops steeply as illustrated in Figure 2.4(a). The reason for there not being a clear maximum when both excitation forces are considered is traced back to the S0 amplitude, which is significantly higher (almost 100 times, see Figure 2.8(c) at 50 kHz) in case of both excitation mechanisms, when compared to the case of only the Lorentz force, whereas the A0 amplitude remains almost unchanged in that comparison. This can also be understood from the inset in Figure 2.4(a), which illustrates the distribution of the body forces within the skin depth layer for the case of only the Lorentz force and

the case of both Lorentz and magnetisation forces, for the proposed realisation (see Table 2.2) at the designated operation point. The arrow lengths are logarithmically scaled, due to the large range of amplitudes and for better comparison. From the inset, it is immediately clear that for the case of the joint excitation of Lorentz and magnetisation forces, a different A0-S0 ratio is to be expected, due to the difference in force distribution, especially as there are more in-plane components for the joint excitation. Since the Lorentz force only case of the proposed realisation represents an optimum in terms of the A0-S0 ratio, any deviation from that distribution would lead to a lower A0-S0 ratio and in a later study is shown to be due to an increase in S0 amplitude.

2.2.4 Experimental Model Validation

The vast drop in the A0-S0 ratio when considering the magnetisation force as an additional excitation mechanism requires an experimental validation of the FE model, in order to draw conclusions about the optimisation process and its feasibility for EMAT design. In the following, first the experimental setup is presented, followed by the validation of the Lorentz force model on an aluminium plate and the combination of the Lorentz and magnetisation force on a steel plate.

2.2.4.1 Experimental Setup

The EMAT prototype based on the proposed realisation is displayed in Figure 2.5 as it rests on a steel plate. The permanent magnet, which has been modelled with a height of 20 mm, consists of two magnets (Magnet Expert Ltd., Tuxford, UK, part number F646) of 10 mm height that are stacked on top of each other. The magnet lift-off from the coil is established with a plastic disc that is filed down to 2.1 mm thickness to match the lift-off of the proposed realization. The coil is a two layered PCB coil that is taken from [Wilcox et al., 2005], where it is the coil of EMAT VII. A wear plate is placed under the coil, which serves the purpose of protecting the coil, while moving the EMAT along the steel plate. The wear plate is a simple plastic foil and the combined height of the wear plate and the coil is 0.9 mm, which corresponds to the value of the height of the coil in the FE model. Furthermore, the induction coil is glued to the wear plate to reduce the number of movable components in the prototype. This allows higher positioning accuracy for the permanent

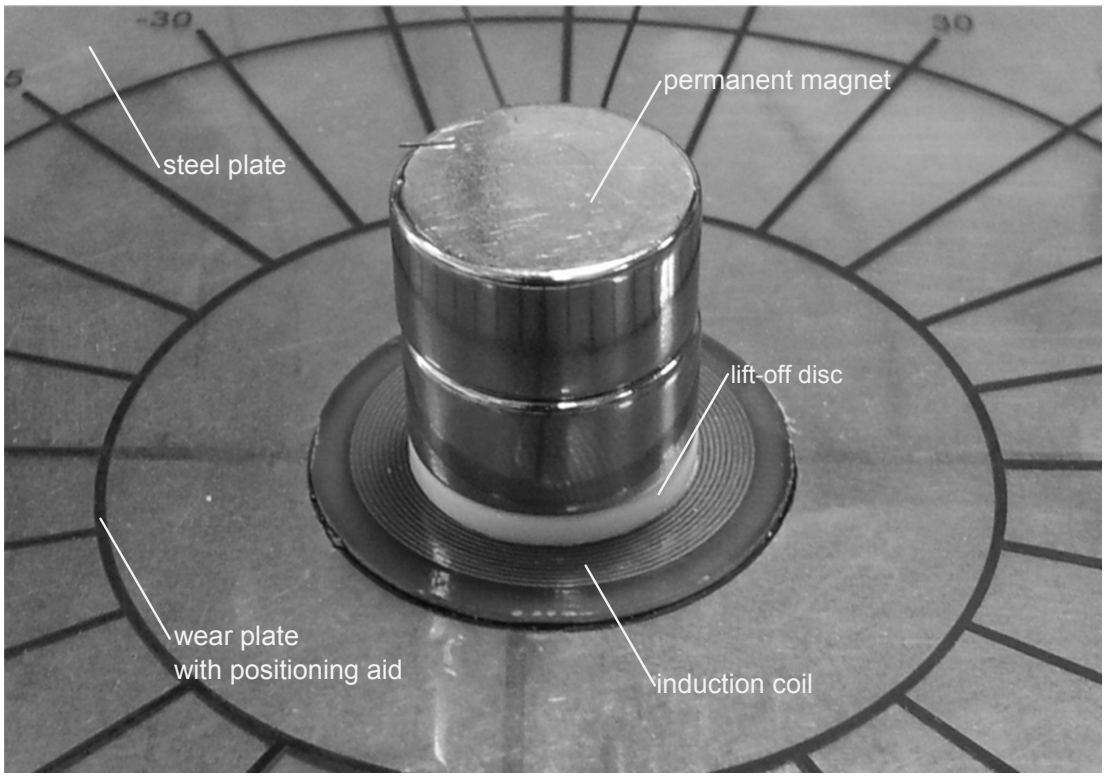

Figure 2.5: EMAT prototype for the proposed realisation in Table 2.2.

magnet with respect to the coaxial position relative to the induction coil. The two ports of the PCB induction coil are connected to a BNC connector for the connection with the measurement instrumentation.

The experimental setup is illustrated in Figure 2.6 for the measurements on a steel plate. Two identical EMAT prototypes are deployed on a 1.2 m by 1.2 m square steel plate with a thickness of 10 mm and are operated in pitch-catch mode. The separation distance is selected as 600 mm and both EMATs are placed at a distance of 300 mm from the plate centre on the symmetry line, as indicated in Figure 2.6. This separation distance of 600 mm is chosen as it allows good distinction between the maxima of the first arrival S0 and A0 Lamb mode wave packets and their reflections from the plate edges. This is especially important for lower frequencies, as the group velocities are more different and the S0 edge reflection wave packets may superimpose on the A0 first arrivals, but it is ensured that the peaks of the S0 and A0 wave packet can still be separated from each other.

A computer is used to control a Handyscope HS3 (TiePie Engineering, Sneek, The Netherlands) digital oscilloscope with integrated arbitrary function generator. The waveform generated with the Handyscope HS3 is amplified using a Hafler P1500 amplifier, prior to being

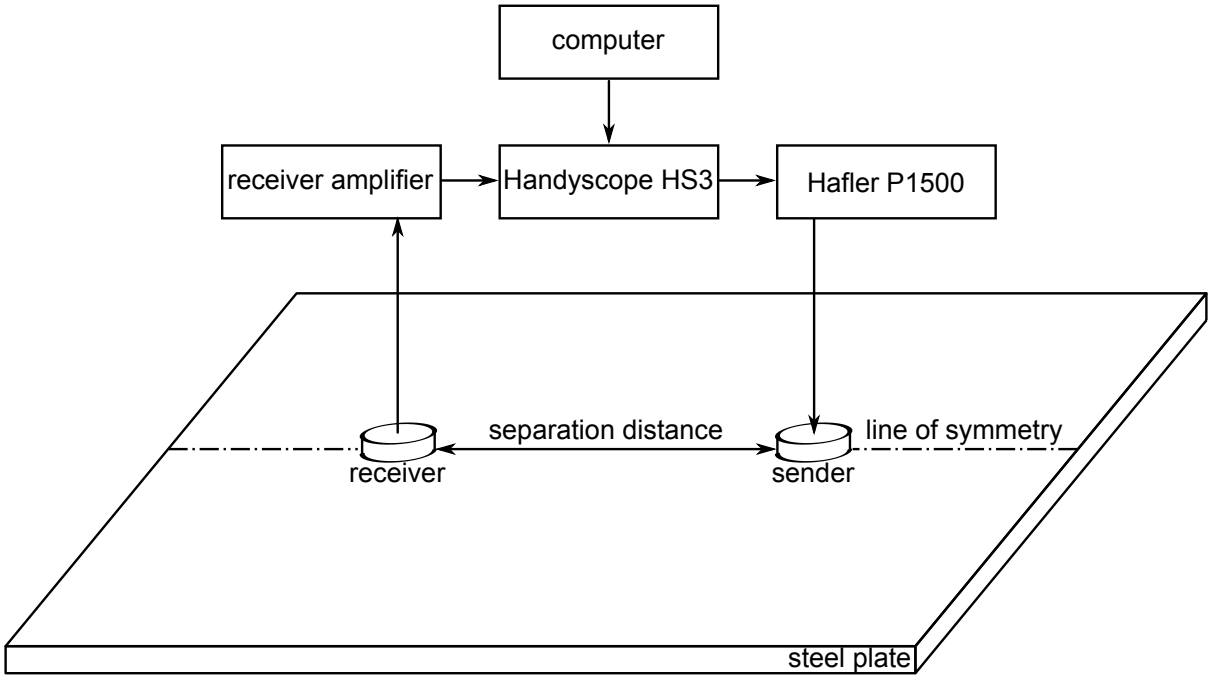

Figure 2.6: Experimental setup for the measurements on a plate, showing the instrumentation used.

fed into the sending EMAT. The receiving EMAT is connected to the Handyscope HS3 via a custom built EMAT receiver amplifier with a gain of approximately 95 dB.

The waveform transmitted by the sending EMAT is a five cycle Hann-windowed toneburst, following the FE simulations. The signal measured at the receiver is digitally filtered in addition to the hardware filtering of the EMAT receiver amplifier, limiting the bandwidth to the frequency band of interest. In the case of this research, this means that the main lobe and the first side lobes of the amplitude spectrum of the input toneburst are considered, as discussed in the model overview section. The filtered voltage time traces are averaged 5000 times in order to reduce incoherent noise. This is particularly important for the S0 mode, whose amplitude may be very low. For verification purposes, the waveform sent to the sending EMAT is monitored for distortions by measuring the input current with a current transformer. The quantisation of the measured signals uses a 12 bit resolution for the amplitudes with a range of $200\,\mathrm{mV}_{p-p}$, which is the lowest range available with the Handyscope HS3 employed. The typical amplitude of the measured noise ranges at around $2\,\mathrm{mV}_{p-p}$ and has been determined based on the time traces for the higher centre frequencies, as the S0 mode can be clearly identified and therefore only experimental noise is present

between the S0 wave packet and the cross-talk.

The validation of the FE model is conducted by considering the A0-S0 ratio as a function of the centre frequency. This approach also helps to eliminate any effect of the frequency response of the measurement electronics, as it is assumed that the frequency response of the measurement electronics is time-invariant and therefore affecting both the A0 and S0 mode equally when considering the same frequency range. Further, it is expected that the mode selectivity changes with the centre frequency, as the coil geometry is no longer matched well with the A0 wavelength and the excitation force direction no longer suppresses the S0 mode well. This is especially important, considering the fairly high A0-S0 ratio of the proposed realisation at the given operation point, as with a dropping A0-S0 ratio, the S0 amplitude may be more reliably determined. The behaviour of the A0-S0 ratio as a function of centre frequency also determines the frequency range of operation for the EMAT prototype for the required operation conditions. The centre frequency is varied from 40 kHz in steps of 5 kHz to 130 kHz. The A0 and S0 amplitudes are determined by the maximum of the wave envelope via the Hilbert transformation of the respective wave packets in the measured voltage-time traces, which are time-gated, according to the expected arrival times. The A0-S0 ratio is computed from the Lamb mode amplitudes using equation (2.19) assuming $\alpha = 1$ for simplicity and represents the cable-to-cable performance.

2.2.4.2 Test on Aluminium Plate

The experiments on an aluminium plate allow the validation of the FE model for the Lorentz force excitation mechanism, as aluminium exhibits only negligible paramagnetic properties. The comparison of the experimental measurements and the simulation are illustrated in Figure 2.7, where the A0-S0 ratio, as well as the normalised A0 and S0 amplitudes, are shown.

From Figure 2.7(a), it can be seen that the A0-S0 ratio decreases with increasing centre frequency, for both simulation and two independent experiments. This is to be expected, as the average diameter of the coil is no longer well matched to half the wavelength, nor is the orientation of the body force matched to the mode shape of the A0 mode any longer. The comparison of simulation and experiment exhibits very good agreement for centre frequencies above 80 kHz. Above 80 kHz, the amplitudes of the A0 and S0 mode can be reliably

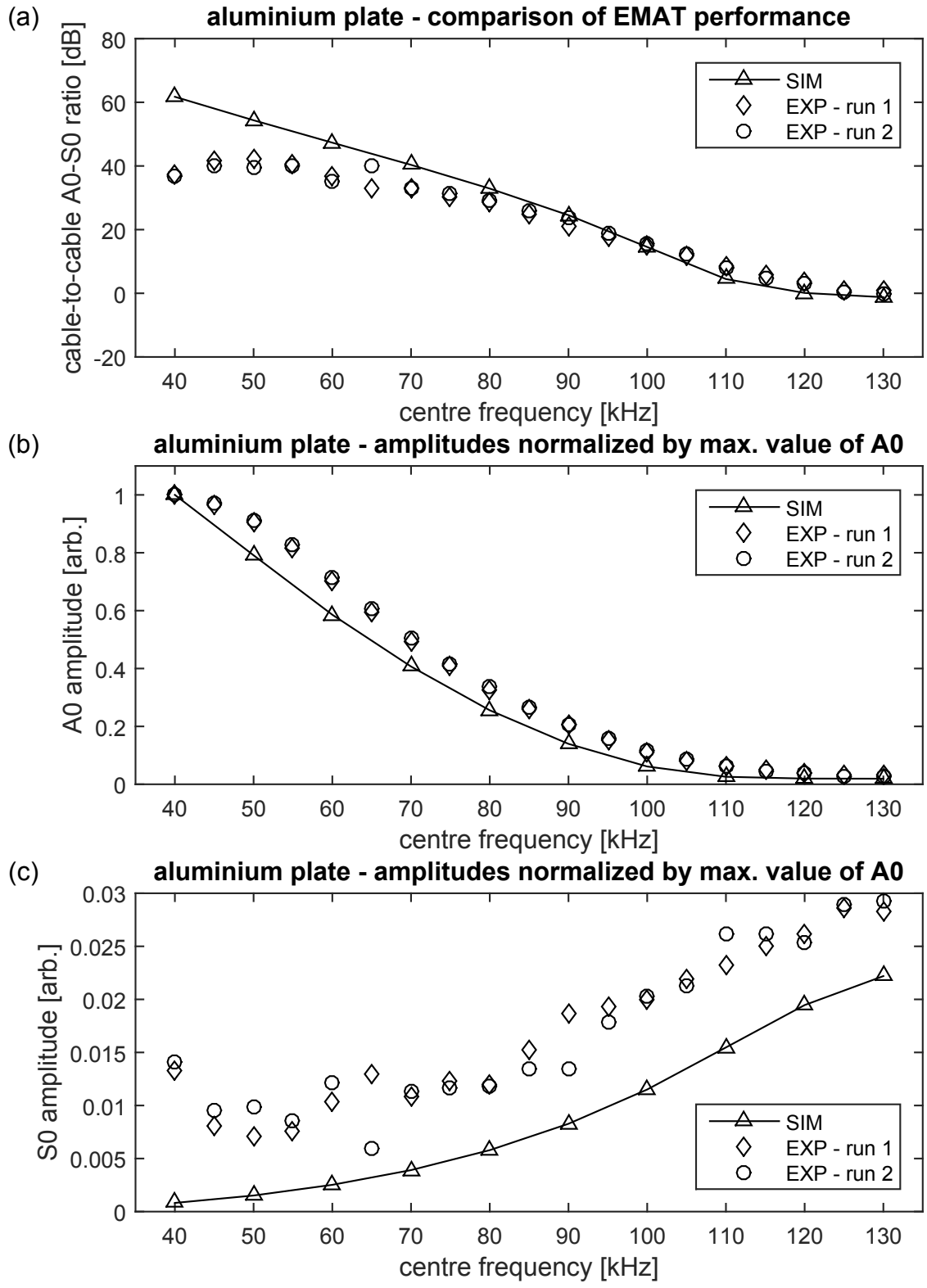

Figure 2.7: Comparison of cable-to-cable A0-S0 ratio (a), A0 amplitude (b) and S0 amplitude (c) between the COMSOL simulation and two independent experimental measurements for an aluminium plate, showing good agreement and rendering the modelling of the Lorentz force valid. The A0 and S0 amplitudes are scaled by the maximum of the A0 amplitude.

determined from the measured voltage-time traces and therefore the A0-S0 ratio can be reliably computed. Below 80 kHz, the experimental A0-S0 ratio tends to plateau at around 35 dB to 40 dB, whereas the simulated A0-S0 ratio continues to rise. This behaviour of the experimental A0-S0 ratio can be explained with the experimental noise that superimposes the S0 amplitude and therefore masks it for very low S0 amplitudes.

Figure 2.7 also shows the A0 (b) and S0 (c) amplitudes for both the simulation and two experimental datasets. Both the A0 and S0 amplitudes have been normalised with the maximum value of the A0 mode for the respective datasets, in order to facilitate an easier comparison. The maximum of the A0 amplitude is selected as the gauging condition, because it is least affected by experimental noise and therefore the most reliable quantity to consider. This can be argued by considering the relative variation between the two experimental datasets across the range of centre frequencies, also implying consistency of the measurements. The maximum A0 amplitude occurs at 40 kHz for both simulation and experiment and the normalised A0 amplitude drops with increasing centre frequency. This behaviour can be again explained with the argument above for the A0-S0 ratio. The experimental and simulated normalised A0 amplitudes show good agreement, especially for the higher frequencies, implying that the model approximates the A0 amplitude drop-off well. The normalised S0 amplitude increases slightly with increasing centre frequency for both simulation and experiment and the comparison between simulation and experiments exhibits a similar trend, however, the experimental S0 amplitudes are higher than the simulated ones. This may be due to the generally large A0-S0 ratio, as the S0 amplitude is very low (always below 3 mV and therefore barely above the experimental noise floor of around 1 mV) and therefore expected to be biased by the experimental noise.

In conclusion, it is found that the FE model matches the experimental data recorded on an aluminium plate well and is therefore a valid representation of the EMAT when the Lorentz force is the only excitation mechanism. Further, it is shown that the EMAT exhibits good A0 mode purity for centre frequencies of up to 70 kHz on a 10 mm thick aluminium plate.

2.2.4.3 Test on Steel Plate

Unlike the aluminium plate, the steel plate exhibits a high magnetic permeability and therefore this needs to be accounted for by the FE model. Additionally to the Lorentz force,

now the magnetisation force is present, as well as the influence of the relative magnetic permeability on the Lorentz force. For this, the simulated performance of the EMAT for the case of only the Lorentz force and the case of both Lorentz and magnetisation force are compared to the measured performance on a steel plate from eight measurements (the evaluation considers the experimental mean and standard deviation for representation only). The comparison is again achieved via a comparison of the A0-S0 ratio as a function of the centre frequency.

In Figure 2.8(a), the A0-S0 ratio is illustrated as a function of the centre frequency, where it can be seen that for both experiment and simulation the A0-S0 ratio drops with frequency. The drop can be again explained with the same argument as in the aluminium plate case. From Figure 2.8(a) it can also be seen that the case of only the Lorentz force as the excitation mechanism greatly overestimates the measured A0-S0 ratio, especially for lower frequency and the operation point. On the other hand, good agreement between simulation and experiment is found when the magnetisation force is considered on top of the Lorentz force as an excitation mechanism.

From the error bars of the experimental data it can be seen that for lower frequencies (<60 kHz) and higher frequencies (100 kHz<) there is an increased variation in the A0-S0 ratio, when compared to frequencies in the middle of the considered frequency range. One explanation for this is that for low frequencies the S0 amplitude and for high frequencies the A0 amplitude is affected by experimental noise, which can be seen from the variations of the measured A0 and S0 amplitudes at these frequencies in Figure 2.8(b) and (c) respectively. Also, the absolute amplitude values recorded for the respective modes at low and high frequencies (around 3 mV or less) are found to be on the order of the noise amplitudes of approximately 1 mV. For frequencies between 60 kHz and 100 kHz the A0 and S0 amplitudes can be reliably determined from the measured time traces, which leads to the small variations in the A0-S0 ratio.

In Figure 2.8(b), the normalised A0 amplitudes are compared and the same normalisation as in the aluminium plate case is used. From Figure 2.8(b) it can be seen that the A0 amplitude decreases with increasing centre frequency for both simulation and experiment. When comparing the experimental A0 amplitudes with those from both simulations, agreement with both simulations is found, implying that the A0 amplitude is not significantly influ-

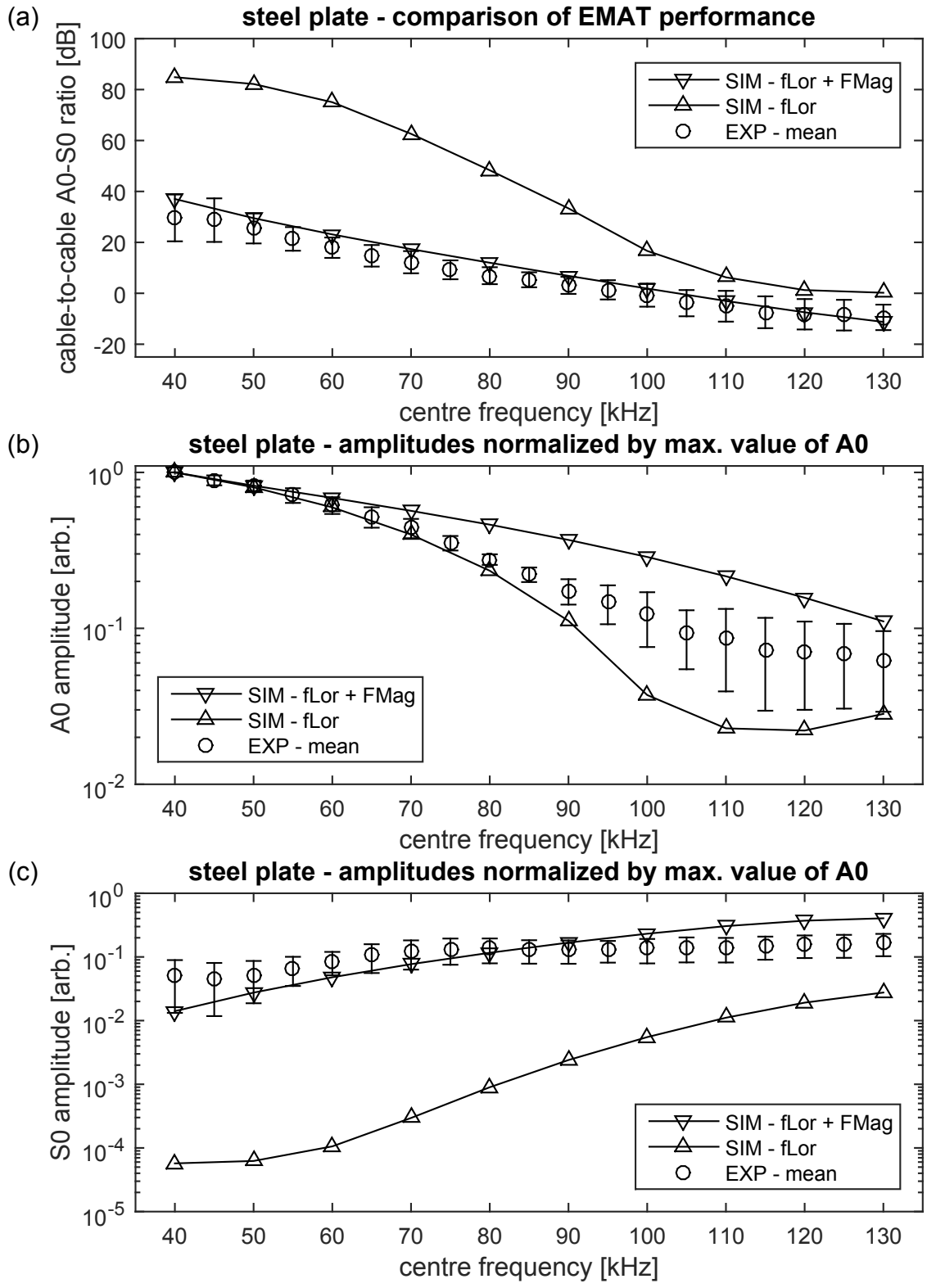

Figure 2.8: Comparison of cable-to-cable A0-S0 ratio (a), A0 amplitude (b) and S0 amplitude (c) between the COMSOL simulation and experimental measurements for a steel plate. The error bars indicate the standard deviation of the eight experimental measurements and the A0 and S0 amplitudes are scaled by the maximum of the A0 amplitude.

enced by the presence of the magnetisation force. Below centre frequencies of 90 kHz, the A0 amplitude is mostly explained with the Lorentz force excitation only. Above 90 kHz, the experimental A0 amplitude starts to vary strongly and takes values between the two curves of the simulated A0 data. Moving on to the normalised S0 amplitudes, Figure 2.8(c), good agreement between the experimental measurements and the case where both Lorentz and magnetisation force are considered is found. From this it can be concluded that the decrease in A0-S0 ratio, when additionally considering the magnetisation force, may be explained by the increase in S0 amplitude rather than the decrease in A0 amplitude.

As a conclusion from the comparison of the experiment on a steel plate with the FE model, good agreement is found when the Lorentz and magnetisation force are considered by the model, rending the model valid. The discrepancy between the model and simulation could be traced back to the experimental limitations of low signal amplitudes and a low signal-to-noise ratio, however, these may not be the only limitations. The remaining discrepancy may be attributed to the incomplete ferromagnetic material model in conjunction with magnetostriction, as this is not accounted for by the model due to the vast uncertainties in the material parameters. For a normal bias magnetic field shear wave EMAT, the amplitude caused by magnetostriction may be up to 30% of the amplitude of the Lorentz force, as discussed in [Ribichini, 2011]. Also the effect of magnetostriction may not be equal for the A0 and S0 mode due to the direction of interaction, explaining some of the discrepancy in terms the A0-S0 ratio. If the assumption is made that for the EMAT design considered in this experimental study with a less normal bias magnetic field, behaves similarly to the findings in [Ribichini, 2011], but less strongly pronounced, this could explain the remaining discrepancy between the simulation and experiment. From this it is also clear that this is one of the limitations of the finite element model, however, the predictions are still sufficiently accurate for the purpose of the model. Further, it is found that the EMAT exhibits an A0-S0 ratio that matches the requirements for A0 tomography of approximately 30 dB S0 suppression.

2.2.5 Numerical Robustness Study

There are a number of uncertainties associated with the EMAT, which will be present when it is manufactured and used. To study the effect of typical parameter variations on the

transducer performance, a numerical robustness study is conducted, using both the Lorentz and magnetisation force as excitation mechanisms. The goal is to evaluate whether the performance of the proposed realization at the designated frequency operation point breaks down for small variations of the design. The two aspects regarded in this study are the magnet lift-off and the uncertainty in the magnetic permeability.

2.2.5.1 Magnet Lift-off

The sensitivity of the EMAT to magnet lift-off is of importance for the practical realization, as it determines the necessary precision for the manufacturing of the EMAT. For this study, the lift-off distance is varied from 1.4 mm to 2.8 mm and the cable-to-cable A0-S0 ratio is illustrated as a function of this parameter in Figure 2.9. The triangles in Figure 2.9 denote the evaluation points for the lift-off and it can be seen that the A0-S0 ratio does not change significantly within the regarded interval. The A0-S0 ratio remains above 25 dB for the entire interval and decreases slightly with increasing lift-off distance. This is an expected result, as with increasing magnet lift-off distance the direction of the magnetic

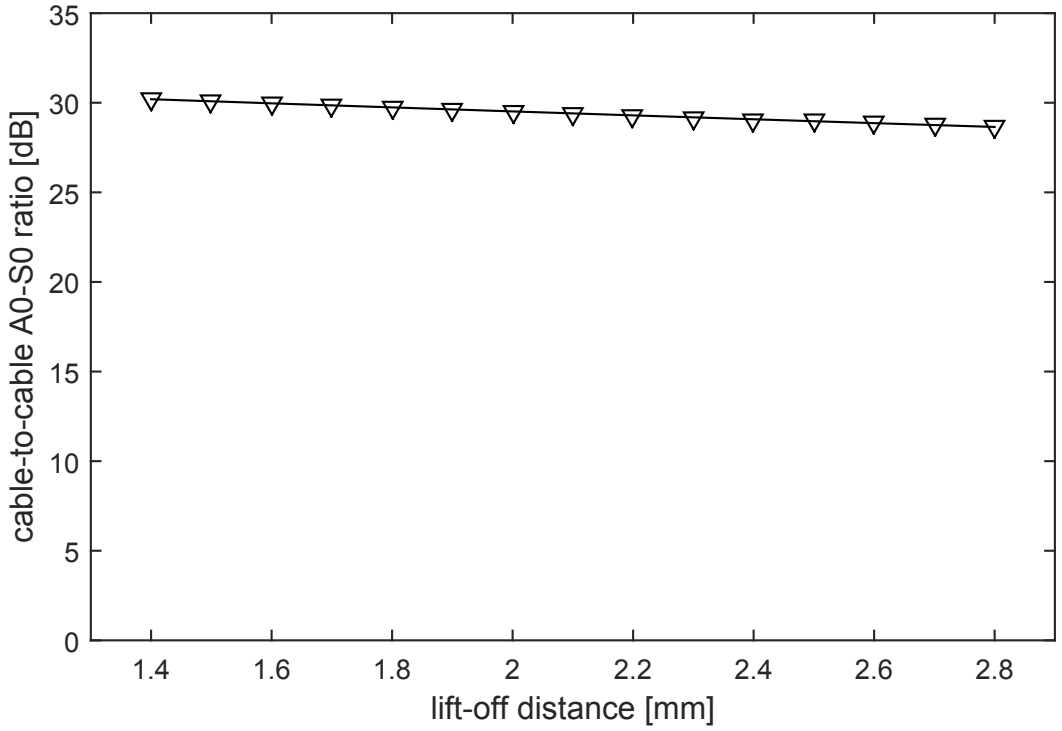

Figure 2.9: A0-S0 ratio as a function of the magnet lift-off for the proposed realisation. The triangles denote the evaluation points for the lift-off.

flux lines in the skin depth layer are slightly changed and therefore slight changes in the mode selectivity are expected. It needs to be noted that for an increase in lift-off distance, the magnetic flux density decreases and therefore the A0 mode sensitivity may decrease. For very small lift-off distances, eddy currents may form in the magnet that may negatively influence the sensitivity. Further, as discussed earlier, the magnet lift-off is not the dominant parameter in the optimization, which is shown by the only small change in performance over the interval of lift-off distances. These results imply robustness of the proposed realization of the EMAT design to a variation in lift-off distance. Therefore, the tolerances on the magnet lift-off for manufacturing can be relaxed.

2.2.5.2 Magnetic Permeability

There is a significant level of uncertainty in the relative magnetic permeability of the steel plate, as this may for example be influenced by the composition of the steel and the magnetization history of the material, additionally to the paramagnetic approximation of the ferromagnetic material. Therefore the influence of the magnetic permeability on the A0-S0

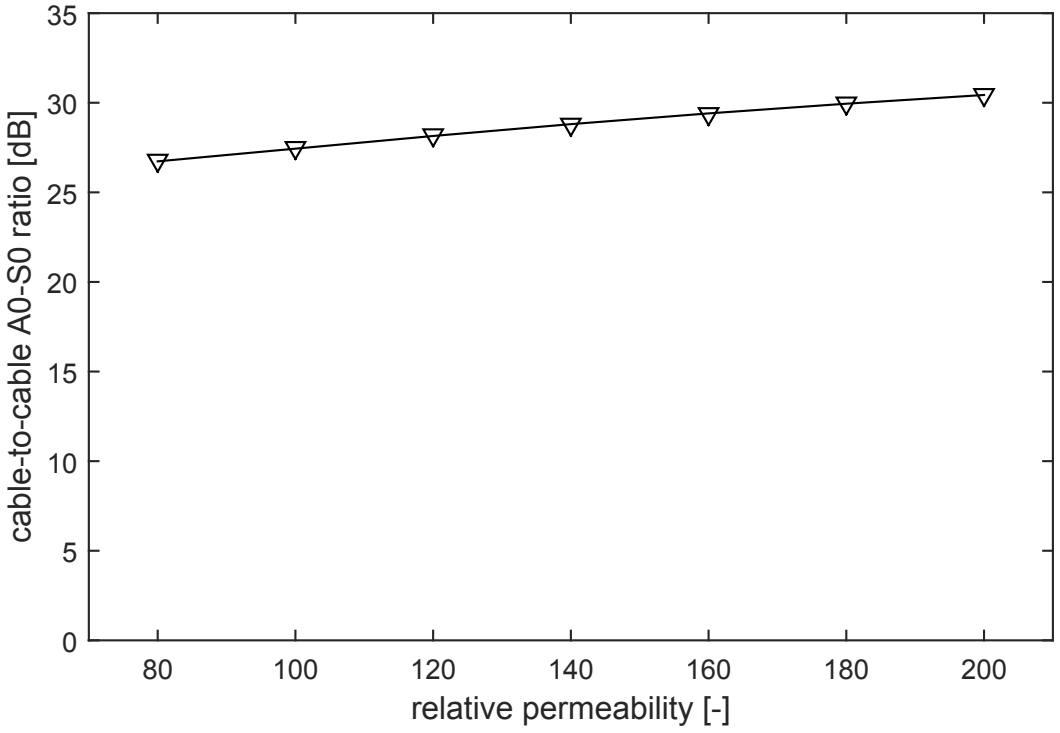

Figure 2.10: A0-S0-ratio as a function of the relative permeability of steel for the proposed realisation. The triangles denote the evaluation points for the various relative magnetic permeabilities.

ratio is studied within a range of 80 to 200 for the relative magnetic permeability, which is typical for steel [Ribichini et al., 2012]. In Figure 2.10, the cable-to-cable A0-S0 ratio is depicted as a function of the relative magnetic permeability within the aforementioned range. It can be seen that the A0-S0 ratio does not vary significantly within this range implying that the relative permeability exhibits negligible influence on the Lorentz and magnetization force excitation mechanism. This behaviour can be explained by the skin depth (equation (2.13)), which varies only slightly due to the change in the relative permeability, therefore only slightly modifying the region where significant Lorentz and magnetization forces are acting. Also, the skin depth is always much smaller than the acoustic wavelength ($\delta \ll \lambda$) for all values of relative magnetic permeability considered here, which suggest that only a negligible influence is to be expected. In conclusion, the influence of the magnetic permeability on the EMAT performance is found to be small for typical variations, implying robustness.

2.2.6 Model-based EMAT design

Having validated the FE model on an aluminium and a steel plate, the EMAT design strategy needs to be revisited. Based on the findings in the previous sections, the drop in A0-S0 ratio in case of the steel plate may be explained with an increase in the S0 amplitude rather than a decrease in A0 amplitude when additionally considering the magnetisation force in the model. Also, in Figure 2.4(a) it can be observed that when including both excitation forces, there is no clear maximum within the feasible range of magnet diameters, but the maximum occurs at the lower bound of the interval. Using an optimisation scheme to find the maximum A0-S0 ratio therefore converges to the minimum magnet diameter, which improves the mode selectivity, however, the mode sensitivity is greatly reduced (see Figure 2.4(b)), due to the reduced magnet size and subsequent reduction in excitation force amplitude. For a successful EMAT design, the duality of mode selectivity and sensitivity needs to be considered and this is clearly not the case when including the magnetisation force into the optimisation procedure, as the performance criterion only considers the selectivity.

A model-based design approach is therefore proposed whereby in a first step, only the Lorentz force is considered in the model and an optimisation is run to find the maximum A0-S0 ratio. Since this represents a severe overestimation of the transducer performance, in

a second step the magnetisation force is included in the model to calculate a more realistic estimation of the transducer performance for the previously optimised design, using the finding that the magnetisation force mostly affects the S0 amplitude.

The major disadvantages of this approach is that the optimisation may not yield the best possible A0-S0 ratio, as for example for a slightly smaller magnet diameter, the selectivity might be better, whereas the sensitivity might be only slightly influenced. An example of this is the comparison of a magnet of 15 mm diameter and of 20 mm diameter. From Figure 2.4(a) and for the case of both excitation mechanisms, it can be seen that there is an increase of around 6 dB in mode selectivity when going to the smaller magnet diameter. In parallel, the sensitivity only drops by 3 dB when considering the smaller magnet diameter, rendering the 15 mm magnet diameter design better, due to the small drop in sensitivity. However, the importance of selectivity over sensitivity needs to be decided on a case-by-case basis and here the balance of selectivity and sensitivity for the 20 mm diameter magnet is found to be sufficient. Since there is no easy way of arriving at the 15 mm magnet diameter design based on the optimisation, using the two step approach is the best modelling approach to determine an improved EMAT design, at the cost of sacrificing some selectivity and given the underlying uncertainty in accurately estimating the magnetic permeability. Another point that needs to be noted for this model-based design approach is that it relies on the wave mode under consideration to be uniquely determined. At higher frequencies, where the A1 mode may superimpose the A0 mode, the out-of-plane displacement is no longer a measure for only the A0 amplitude. However, this limitation may be overcome with approaches that allow for the unique determination of the A0 mode, such as the wavenumber spectrum in the far field and an adoption to performance criterion.

In case of non-magnetic materials such as aluminium, the approach of using the optimisation to find the peak performance (the magnetisation force re-evaluation step is omitted) will lead to the best possible compromise between selectivity and sensitivity, as there is a clear and unique maximum for the A0-S0 ratio, as shown in [Nagy et al., 2014] and found here.

The optimisation only looks at the magnet diameter and magnet lift-off as parameters, however, the model-based design approach is not limited to that. The optimisation may use other parameters, which are capable of shaping the magnetic flux, as this is the underlying physics which is to be used for optimisation. One example of this is for example given in

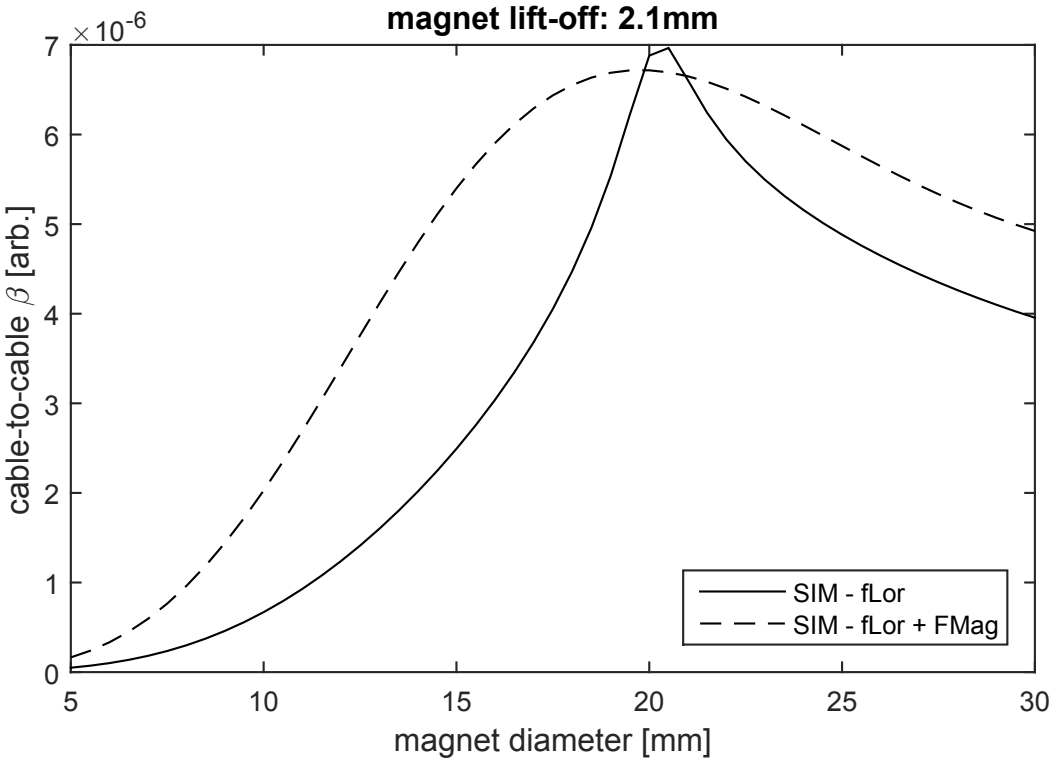

Figure 2.11: Comparison of performance measures β for a magnet lift-off of 2.1 mm as a function of the magnet diameter and under consideration of the wave excitation mechanisms on a steel plate.

the patent in [Instanes et al., 2014], where an optimised and an unoptimised design are compared, clearly showing that this is a feasible approach. Similarly, EMAT VII of [Wilcox et al., 2005] was available to the authors and uses the same coil as in the EMAT design here, but with a magnet of diameter 32 mm. In an experimental comparison, it is found that there is a clear improvement in terms of the A0-S0 ratio, for the EMAT with a magnet diameter of 20 mm, clearly showing the feasibility of the presented model-based design. The measured performance at 50 kHz also matches that presented in Figure 9(c) of [Wilcox et al., 2005].

Alternatively, a different performance criterion could be developed that considers both the mode selectivity and sensitivity simultaneously, for example by finding the maximum of the product of the A0-S0 ratio and the greater of the A0 and S0 amplitude values

$$\beta = \gamma \times \max(|A_0^*|^2, |S_0^*|^2). \tag{2.20}$$

In equation (2.20), the quantities $|A_0^*|^2$ and $|S_0^*|^2$ denote the cable-to-cable A0 and S0 am-

plitudes, obtained by power-normalising and squaring of the underlying amplitudes and the β-parameter represents an amplitude weighted version of the γ-parameter. The β-parameter is illustrated in Figure 2.11, where both the β-parameter is depicted as a function of the magnet diameter for the Lorentz force excitation and the joint excitation with both the Lorentz and magnetisation force on a steel plate.

When comparing the γ-parameter shown in Figure 2.4(a) with the β-parameter Figure 2.11, for the case of only the Lorentz force excitation mechanism, it is found that both exhibit a unique maximum at the same location, rendering both approaches equivalent. For the case of the joint excitation with Lorentz and magnetisation force, the γ-parameter takes its maximum value for the lowest magnet diameter as seen from Figure 2.4(a), whereas the β-parameter shows a unique maximum around a magnet diameter of 19 mm. This maximum roughly matches with that of the Lorentz force case, however, it is not as pronounced as the one for the Lorentz force case and only shows very small variations for a large range of magnet diameters around the maximum. The behaviour of the β-parameter with the magnet lift-off is similar to that of the γ-parameter, where only a small influence is found. The β-parameter has not been considered any further here, as no improvement to the two-step model-based EMAT design approach is achieved.

2.3 Tomography System Development

In the previous section, an EMAT transducer has been developed that matches the specifications for guided wave tomography at the given operation point and its performance has been experimentally verified. Based on the physical prototype (Figure 2.5) of the proposed realisation, the transducer is developed further for the application in guided wave tomography measurements. In the following, the integration of the developed EMAT into the guided wave tomography data capture system is presented.

2.3.1 Further Development of the EMAT for Guided Wave Tomography

The initial EMAT prototype from Figure 2.5 has been used in the previous section for the purpose of validating the model and establishing that the enhanced design features

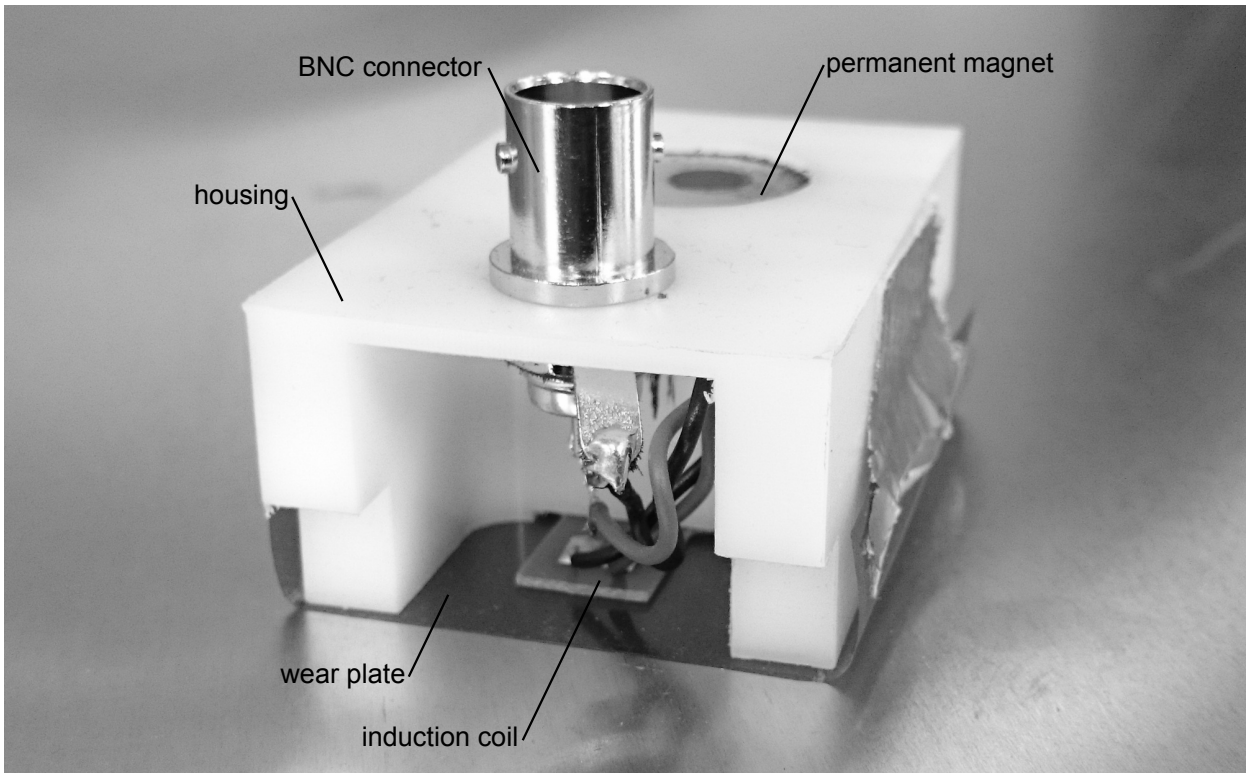

Figure 2.12: EMAT developed from the physical prototype (Figure 2.5) of the proposed realisation for the guided wave tomography system.

the targeted mode selectivity. However, the design has certain practical limitations, which prevent its effective deployment for data capture for guided wave tomography measurements.

The major limitation of the prototype in Figure 2.5 is that it exhibits various movable parts, such as the coil and wear plate assembly, the lift-off disc and the permanent magnet. For practical applications, there is no need for this and a housing is designed around the coil and permanent magnet in order to house all the components of the EMAT and improve concentric alignment of the coil and the permanent magnet. The EMAT used for the tomography data capture is shown in Figure 2.12 and it can be observed that additionally to the induction coil and permanent magnet, the BNC connector for the connection to the measurement electronics is also incorporated into the housing design, making the transducer very compact and easy to deploy. For easier handling, handling notches have been added, as the static magnetic force between the permanent magnet and the magnetic specimen may be quite large. Further, for better positioning, positioning notches have been incorporated into the housing to allow for accurate alignment of the centre of the coil with the desired location on the specimen.

2.3.2 Experimental Setup of the Guided Wave Tomography System

For the inspection of pipes with restricted access, an approach with two parallel ring arrays is selected here, as illustrated in the bottom half of Figure 2.13, where the experimental setup for the guided wave tomography data capture is depicted. All measurements are conducted on a pipe with 12 in (0.3048 m) diameter and a schedule 40 wall thickness (10.321 mm), that is made of STD ASTM A106-B steel and at a length of 2 m weighs about 200 kg. An artificial defect representing a smooth corrosion patch is milled onto the middle of the pipe and the two EMAT arrays are placed on either side of the defect separated by a certain ring separation distance. Each of the EMAT arrays consists of twenty-four EMATs (see Figure 2.12), that are spaced at about 43 mm from each other in circumferential direction. This spacing is slightly more than the A0 wave length (approximately 40 mm) at the operation frequency of 50 kHz and therefore under-sampling spatially (typical element separation distance of ultrasonic arrays is about half a wavelength or less), with respect to the Nyquist

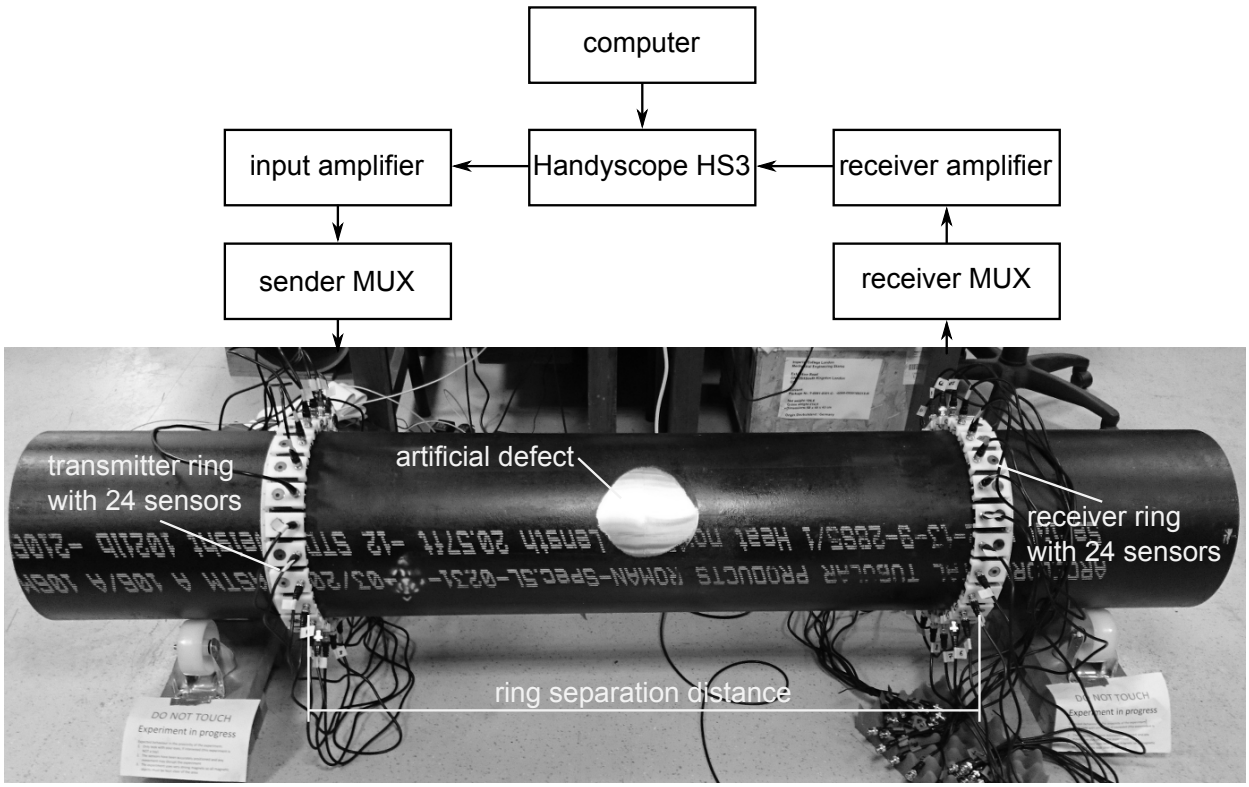

Figure 2.13: Experimental setup for the guided wave tomography measurements, showing the pipe specimen (12 in diameter schedule 40 made of STD ASTM A106-B steel), sensor arrays and schematic instrumentation.

criterion for which a sampling period of half of the wavelength is desired. The reason for the spatial under-sampling lies for once in the geometric dimensions of the EMAT and its casing, as well as the specifications of the project, which demand ring arrays. Also, if two EMATs are too close together, the performance may be negatively influenced, in terms of mode selectivity and directivity. The reason for this lies in the fact that the bias magnetic field of the permanent magnets might interact and therefore no longer be axisymmetric. This then leads to an alteration of the excitation force direction and a loss in performance. Further, the circumferential alignment of the two ring arrays is achieved via two aligned measurement tapes, which have been aligned using a sheet laser device.

Figure 2.13 also gives a schematic overview of the instrumentation used for the data acquisition, which is adapted from the one used for the experimental tests with the physical prototype sensors for the FE model validation in the previous section (Figure 2.6). Additionally to the previous setup, two multiplexers (MUXs) are included in order to allow switching between various send and receive combinations, as for the dataset for thickness reconstruction all possible send-receive combinations need to be captured between the sending and receiving EMAT array (576 in total). The MUXs consist of two 24 channel relay boards OME-DB-24R (OMEGA Engineering, INC., Stamford, Connecticut, USA), leading to a total of 48 relays. The reason for this is that in order to enhance the noise performance, one relay is used to switch the live and another the ground line. The wiring is achieved with twisted wire pairs to further enhance the noise performance. The relay boards are switched with an OMG-DIO96 (OMEGA Engineering, INC., Stamford, Connecticut, USA) controller, which is connected to the computer via a USB port. The data acquisition software is implemented in Matlab and automatically switches the send-receive channels and manages the measured data.

After initial tests with the setup of Figure 2.13, it is found that the MUX for the receiving array introduces significant noise levels, such that the ultrasonic signal can no longer be recovered. Since this issue is related to the receiver (Rx) MUX, because this phenomenon is not observed in the prototype tests, a study regarding the configuration of the order of the receiver amplifier (Rx AMP) and receiver multiplexer (Rx MUX) in the data acquisition chain is conducted. The tests are conducted on a defect free pipe with a ring separation distance of 1.2 m and all measured time traces are time averaged 1000 times to reduce the incoherent noise.

The results are shown in Figure 2.14, in which all A-scans between the transmitting array and one receiver are depicted for three experimental configurations; in (a) the Rx MUX is placed before the Rx AMP as in Figure 2.13, in (b) the Rx MUX is place after the Rx AMP and in (c) the Rx MUX is omitted and represents a reference case. From Figure 2.14(a), it can be clearly seen that the experimental noise is greater than the signal data, when compared to Figure 2.14(b), in which the first arriving wave front can be easily identified. In Figure 2.14(b), also the electromagnetic cross-talk can be observed between 0 and 100 μs. This suggests that the order of the Rx MUX and Rx AMP in the data acquisition chain matters and exhibits a nonlinear behaviour as switching the order of the Rx MUX and Rx AMP yields different results. The comparison of Figure 2.14(a) and Figure 2.14(b) with the reference case in Figure 2.14(c) clearly shows that the experimental noise levels are caused by the receiving multiplexer and the influence is more significant, if the Rx AMP is placed after the Rx MUX. From this, it can be concluded that the influence of the Rx MUX onto the signals is greater, if the input signal of the Rx MUX exhibits a (very) small amplitude.

As a conclusion from this study, the receiving array is multiplexed manually and therefore making the data capture semi-automatic. An alternative approach to work around this limitation to automatic data capture, is by using the configuration of Figure 2.14(b), in which the measured signal from the EMAT is amplified with the Rx AMP before being multiplexed. This however would require a total of twenty-four pre-amplifiers in the case here and is not feasible due to budget and various other constraints.

The analogue-to-digital discretisation of the pitch-catch measurements for the various send receive combinations uses a sampling rate of 1 MHz and 20000 samples are recorded (corresponds to about 60 m A0 propagation distance or 30 length of the pipe). In a study it was found that this combination of sampling rate and recorded samples yields the best compromise between data capture speed and signal quality, such that one send receive combination when averaged 1000 times can be measured in approximately 40 s and all 576 send-receive combinations for the whole dataset in 6.5 hours (if manual receiver multiplexing is not delayed). Further, this is sufficient to capture all the necessary information for the thickness reconstructions and helps to reduce the total amount of data that needs to be stored for processing.

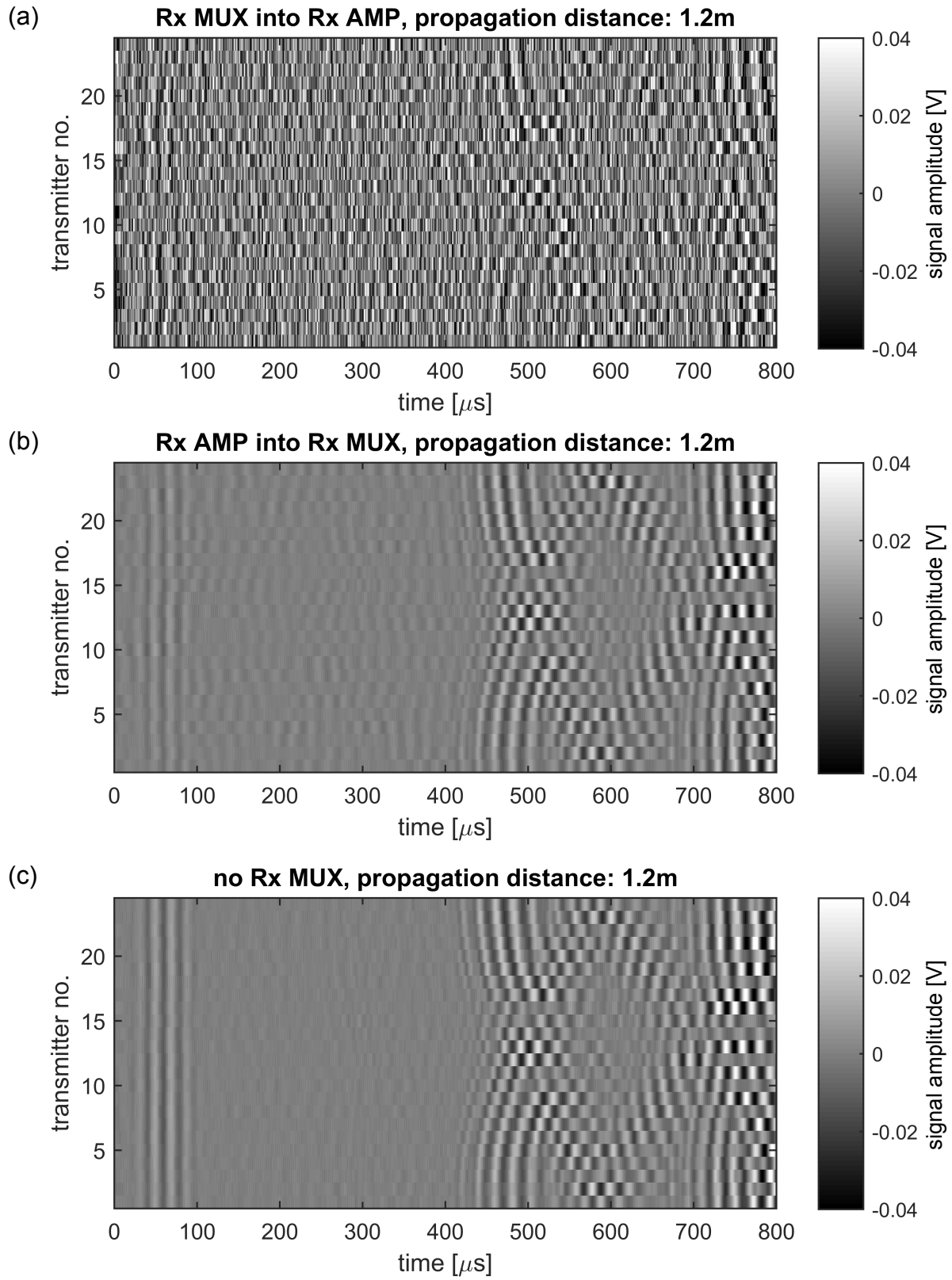

Figure 2.14: Experimental study of various receiver and reciver MUX configurations, showing the various time traces between all sensors on the transmitting EMAT ring and a single sensor on the receiving array. In (a) the receiver Rx MUX is placed before the receiver Rx AMP, in (b) the Rx AMP is place before the Rx MUX and in (c) the Rx MUX is removed for reference.

Chapter 3

Guided Wave Tomography on Pipes and System Robustness

In this chapter, first the theoretical background of guided wave tomography is presented and the employed tomography algorithm for the thickness reconstruction is illustrated. Because of the constraints imposed by the experimental setup, a limited-view problem arises and the techniques/algorithms used to treat its impact are discussed. The approach to guided wave tomography presented here is based on [Huthwaite, 2012] and the reader is pointed there for a more detailed description of various aspects of the algorithms. The data processing framework is then applied to experimental measurements and some experimental studies regarding its robustness presented. Further, some numerical studies concerned with electromagnetic-acoustic coupling and the limited-view problem are shown. In the last section, an enhanced data acquisition technique based on Golay complementary sequences is discussed, allowing for faster data capture and the feasibility of low voltage operation of the guided wave tomography system.

The studies presented in this chapter aim to establish the robust operation of the developed guided wave tomography system for the subsequent investigations of areas with restricted access on a laboratory scale. These robustness studies also represent the novelty contribution of this chapter.

3.1 Theoretical Background

In guided wave tomography, the estimation of thickness is of interest, as it allows for the estimation of the remaining service life. A useful simplification in guided wave tomography is to assume that the elastic scattering (fully three-dimensional elastic model, mode conversions are possible) of guided waves within a plate of varying thickness behaves in the same way as the scattering of acoustic waves (two-dimensional bulk wave model, no mode conversions possible) within a field with varying velocity. For the acoustic assumption, the dispersion relationship is exploited, whereby the velocity becomes a known function of thickness for a particular frequency. It needs to be noted that the dispersion curves are calculated for an infinite plate of uniform thickness and therefore thickness variations need to be relatively slow (and smooth).

The result of assuming acoustic scattering for the reconstruction of elastic scattering phenomena greatly simplifies the thickness reconstructions, as no computationally intensive forward model is required. However, there is a major drawback associated with this assumption, which is addressed in [Huthwaite, 2014]. It is found that when assuming an acoustic scattering model for the reconstruction of elastic scattering data, the achievable resolution for the reconstructions drops from 0.5 wavelengths, as given by the Born approximation [Born et al., 2000], [Kak and Slaney, 2001], to 1.5 to 2 wavelengths, when comparing to reconstructions from acoustic scattering data. The resolution limit is defined here as the wavelength corresponding to the highest spatial frequency that can be reconstructed for the given problem, such that for example, under the Born approximation and in a full view configuration, leads to 0.5 wavelength.

This drop in resolution is analysed for both an elastic guided wave and an acoustic scattering model, by comparing the scattered field from a flat bottom hole. The flat bottom hole is chosen to be very small and required to satisfy the Born approximation, such that it can be considered as “elemental” and the scattering from larger defects can be understood as the superposition of such “elemental” scatterers. The results show that both scattering models match for the through transmission case 0° up to an angle of approximately ±34°, relative to the through transmission direction. Under the Born approximation and from the Fourier diffraction theorem [Kak and Slaney, 2001], it is know that the transmission

accounts for the lowest wavenumber components, while the reflection corresponds to the highest components (up to the resolution limit of 0.5 wavelengths), with the intermediate angles corresponding to the wavenumber components in-between. Therefore, the inability to extract wavenumber components above an angle of $\pm 34°$ from the through transmission case from elastic scattering data, when using the acoustic assumption, effectively represents a low-pass-filtering of the image with a resolution limit of approximately 1.5 to 2 wavelengths.

The thickness reconstructions here employ the acoustic assumption, whereby for the inversion of the acoustic wave field, a map of velocities is calculated that subsequently convert into a thickness map using the known dispersion relationship. To reconstruct the velocity, the acoustic wave equation is employed and represented using the inhomogeneous scalar Helmholtz equation with the scalar potential Ψ

$$(\nabla^2 + k_u^2)\Psi = -O\Psi. \tag{3.1}$$

In equation (3.1), k_u represents the wave number in the defect free pipe wall (subscript "u" for uniform) and O the object function that accounts for the presence of the defect/thickness variation in the area of interest and is defined as

$$O = k_u^2\left[\left(\frac{c_u}{c}\right)^2 - 1\right]. \tag{3.2}$$

In equation (3.2), c_u expresses the wave speed in the defect free pipe wall, whereas c is the wave speed at a particular location in the region of interest, accounting for the thickness variation.

3.1.1 HARBUT Algorithm

The computation of the thickness map from the experimental measurements is achieved with the HARBUT algorithm (Hybrid Algorithm for Robust Breast Ultrasound Tomography) [Huthwaite and Simonetti, 2011], [Huthwaite, 2012], [Huthwaite and Simonetti, 2013], which was first developed for reconstructing velocity maps of the human breast to detect breast cancer and later extended to guided wave tomography for thickness mapping in plates and pipes. HARBUT is a two stage approach that combines a bent-ray tomography (BRT) algorithm with a diffraction tomography (DT) algorithm in order to combine the merits of

each algorithm and to counter the limitations of the (first order) Born approximation. The first order Born approximation assumes that the wave field scattered by, for example, a defect is a superposition of many small and independent "elemental" scatterers. This is obviously not accurate in reality, because the individual scatterers are not mutually independent and multiple scattering may occur. However, if the phase distortion due to the presence of the defect is small relative to the background, the Born approximation may be assumed [Born et al., 2000], [Kak and Slaney, 2001]. In HARBUT this concept of the Born approximation being valid relative to a background is realized by splitting up the object function from equation (3.1) into two parts such that

$$O = O_b + O_\delta \tag{3.3}$$

In equation (3.3), the object function is split into a background object function O_b and a small perturbation object function O_δ. The aim of this approach is to make O_δ as small as possible, such that it can be described well with the Born approximation and therefore it is crucial that the background object function O_b already represents a good approximation of the whole object function. The BRT algorithm is used to get a low resolution estimate of the thickness in the area of interest by fitting an arrival time model based on the eikonal equation [Sergey Fomel, 1997] to the experimentally measured arrival times. The BRT thickness map (or image, which is used synonymously) is then used in a second step as a background (O_b) for the DT algorithm and a higher resolution thickness map is obtained, as the Born approximation now only needs to be valid with respect to the background. The DT thickness map is based on a filtered beam-forming image [Simonetti and Huang, 2008], where the background is accounted for in the beam-forming step.

The reconstructions from using the BRT image as a background in the HARBUT algorithm can be improved in many cases by additional iterations. The idea for that is, that the initial image obtained with the HARBUT algorithm can again be used as a background for the next iteration such that $O_b^{(n+1)} = O^{(n)}$ with n being the iteration number and the zeroth iteration being based on the BRT image as the background. With an increasing number of iterations, this leads to a decrease in O_δ and an improvement in accuracy, since the Born approximation describes the scattering process better for small O_δ. A detailed description of the HARBUT, as well as, the BRT and DT reconstructions can be found in [Huthwaite

and Simonetti, 2013].

3.1.2 Limited-view Configuration and VISCIT Algorithm

The most accurate reconstructions with the HARBUT algorithm from the previous section are achieved when the region of interest is illuminated from all directions and the scattered field is recorded also from all directions, leading to what is known as a full view configuration. However, it is not always possible to measure with a full view configuration and in the experimental setup considered here, which is illustrated schematically in Figure 3.1(a), this is not the case, as the artificial defect is not surrounded by sensors, but rather two ring arrays, one on either side of the defect (see Figure 3.1(a)). By unwrapping the pipe into a flat plate Figure 3.1(b), the defect then lies between two parallel linear arrays and it can be clearly seen that the full view configuration does not apply. The influence of the pipe curvature when unwrapping the pipe can be disregarded in the present case, due to the large pipe radius relative to the wall thickness in accordance to [Liu and Qu, 1998], [Fong and Lowe, 2004], [Brath et al., 2014].

Limited-view configurations add additional challenges to the thickness reconstruction, as less information is available for the reconstruction and one approach to this problem is to use the Virtual Image Space Component Iterative Technique (VISCIT) algorithm [Huthwaite et al., 2013b]. VISCIT is a projection based regularization approach that uses adaptive thresholding to account for the missing viewing angles in a limited-view dataset. The idea of VISCIT is to split up the full view wave field dataset into two subsets, a set containing the measured viewing angles and a set containing the missing ones that are supposed to be estimated; the latter set is initially set to zero. The corresponding full view wave field dataset is then imaged (with a linear imaging algorithm) and the resulting image is regularized by applying a threshold to the image. The image contrast values (thickness or wave speed values here) above this threshold are retained, whereas anything below is set to the background value, in order to minimize the artefacts caused by the limited-view configuration. The assumption behind this regularisation approach is that true features exhibit higher contrast values than the artefacts, which appear at lower contrast values. Based on the regularized image, a linear forward model employing the scalar Helmholtz equation (equation (3.1)) is used to compute the updated full view wave field. The estimates of the measured subset

of the full view dataset are replaced with the actually measured wave field values and the whole process is then iterated, adjusting the regularization parameters within each iteration. In [Huthwaite et al., 2013b], it has been shown that the VISCIT algorithm can be coupled with the HARBUT algorithm, however, VISCIT clearly cannot perfectly replace the data capture that is achieved in full view configuration, so generally a small error between the full view configuration and the limited-view configuration enhanced with VISCIT is to be expected.

3.1.3 Helical Path Separation Algorithm

The circular-symmetric nature of the pipe geometry allows for an infinite number of propagation paths of different length between a sender and a receiver, as the waves may travel

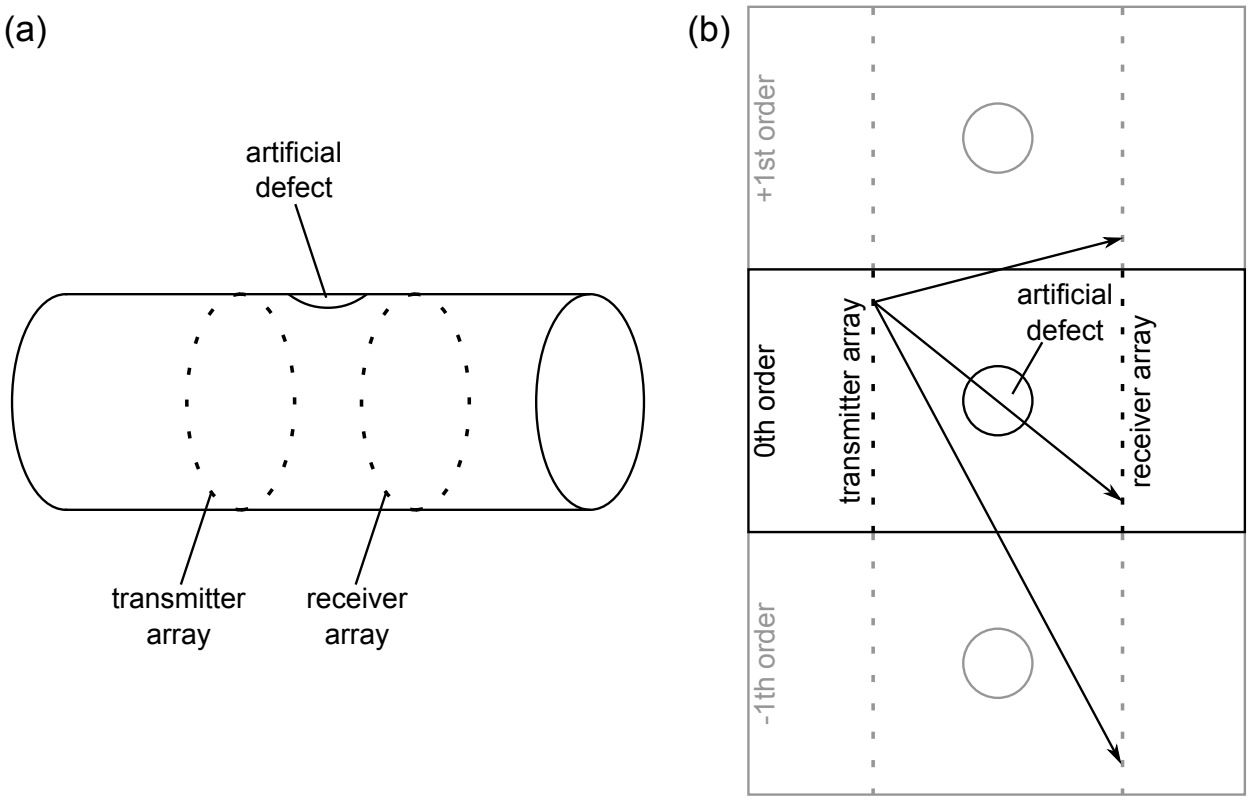

Figure 3.1: Schematic representation of the tomography setup in (a), showing the location of the two arrays on a pipe on either side of a defect and in (b) the flattened version. In (b) the 0th order (black) represents the unwrapped pipe and the higher orders (grey) are replications of the 0th order to account for the circular-symmetric nature of the pipe, as waves may travel across the edge, where the pipe is unwrapped. The artificial defect also replicates for the higher orders and the arrows indicate the various propagation path between one transmitter and a receiver, when considering the zeroth and first order helical paths.

many times around the circumference (azimuthal direction) of the pipe, before reaching the receiving sensor. These paths are termed helical paths due to their shape (if there is an axial offset between a sender and receiver) and are classified into orders for how often the wave travels around the circumference of the pipe, as well as, attributed with a sign, positive or negative, in accordance with the azimuthal direction of the wave path. This is illustrated in Figure 3.1(b) for the transmission between two sensors, showing the zeroth order, as well as the positive and negative first order paths for the unwrapped pipe. Additionally, the transmission path between a sender and a receiver, including its first helical orders, is illustrated. The measured amplitude-time trace can then be understood as the superposition of the amplitude-time traces between the sender and receivers of the respective helical order. It is also clear from Figure 3.1(b) that separating the various wave packets corresponding to the respective helical order, increases the length of the two linear arrays and the amount of missing view angles decreases, leading to a less ill-posed reconstruction problem.

In [Huthwaite and Seher, 2015], an algorithm is proposed that allows for the separation of the various helical paths into separate amplitude-time traces. It is only presented here briefly, as the method has been initiated by the lead author Dr. Huthwaite and does not represent a novelty in the scope of this research. The algorithm makes use of the known location of the transducers and subsequently the associated propagation distances, as well as the dispersion curves for the plate/pipe wall. In a first step, the measured amplitude-time traces for one transmitter and all receivers are replicated by twice as many times ($2N$) than the maximum order of helical paths to be extracted, which range from $-N$ to $+N$, i.e. two times for recovering up to the first order helical path, as illustrated in the case of Figure 3.1(b). The replicated signals then contain the wave front of interest and are backpropagated to the transmitter location, using the known receiver positions and dispersion curves, while assuming a uniform plate/pipe wall thickness. A non-uniform thickness may primarily arise from defects in the case considered here and it is assumed that the defect is sufficiently localised, such that it does not cause widespread distortions of the wave field. Also, the pipe wall thickness is found to be mostly uniform in accordance with Appendix A. Through this backpropagation step, the wave front of interest then aligns almost uniformly for all receivers at the time origin and is then windowed to remove some parts of the unwanted signal content. A low pass filter is applied over the receivers (in Fourier domain) and the filtered wave front is then forward propagated again to the original receiver locations. After

shifting the wave front to all the non-zeroth orders, the shifted wave fronts are subtracted from the original (replicated) signals, removing some of the unwanted signal content. This process is then iterated using the so obtained signals as the new original and adjusting the low pass filter with each iteration. For a detailed description of the algorithm, the reader is pointed to [Huthwaite and Seher, 2015].

The algorithm from [Huthwaite and Seher, 2015] has been tested on simulated and experimental data (measured with the tomography system presented in Chapter 2) in the presence of a defect and robustness of the algorithm has been established, rendering the backpropagation based on a uniform thickness valid.

3.2 Reference Measurement

The reference measurement represents the initial test for the developed guided wave tomography system as well as data processing framework and is used to establish the achievable performance when direct access to the defect is possible. In the following, first an overview of the two considered artificial defects is given, followed by the data acquisition framework and initial experimental results from both defects.

3.2.1 Overview of Artificial Defects

The experimental studies consider two artificial defects that are chosen to be of realistic size and assumed to have an axisymmetric Hann-shaped profile, mathematically described as

$$t(\mathbf{r}) = \begin{cases} \frac{d}{2}\left[1 - cos(\frac{2\pi}{l}|\mathbf{r}|)\right] - d + t_0 & \text{if } |\mathbf{r}| \leq \frac{l}{2}, \\ t_0 & \text{if } |\mathbf{r}| > \frac{l}{2}. \end{cases} \tag{3.4}$$

In equation (3.4), t denotes the thickness at a location $\mathbf{r}$, assuming that the defect is located at the origin of the reference frame. The defect is characterised by its depth d and lateral extend l and t_0 represents the nominal thickness. This is illustrated in Figure 3.2(a), where a thickness map of the unwrapped pipe for the deeper of the two considered defects is depicted. Figure 3.2(a) also shows the cut line for the deepest point cross-section along the axial direction, as the main interest is to determine the minimum wall thickness, which

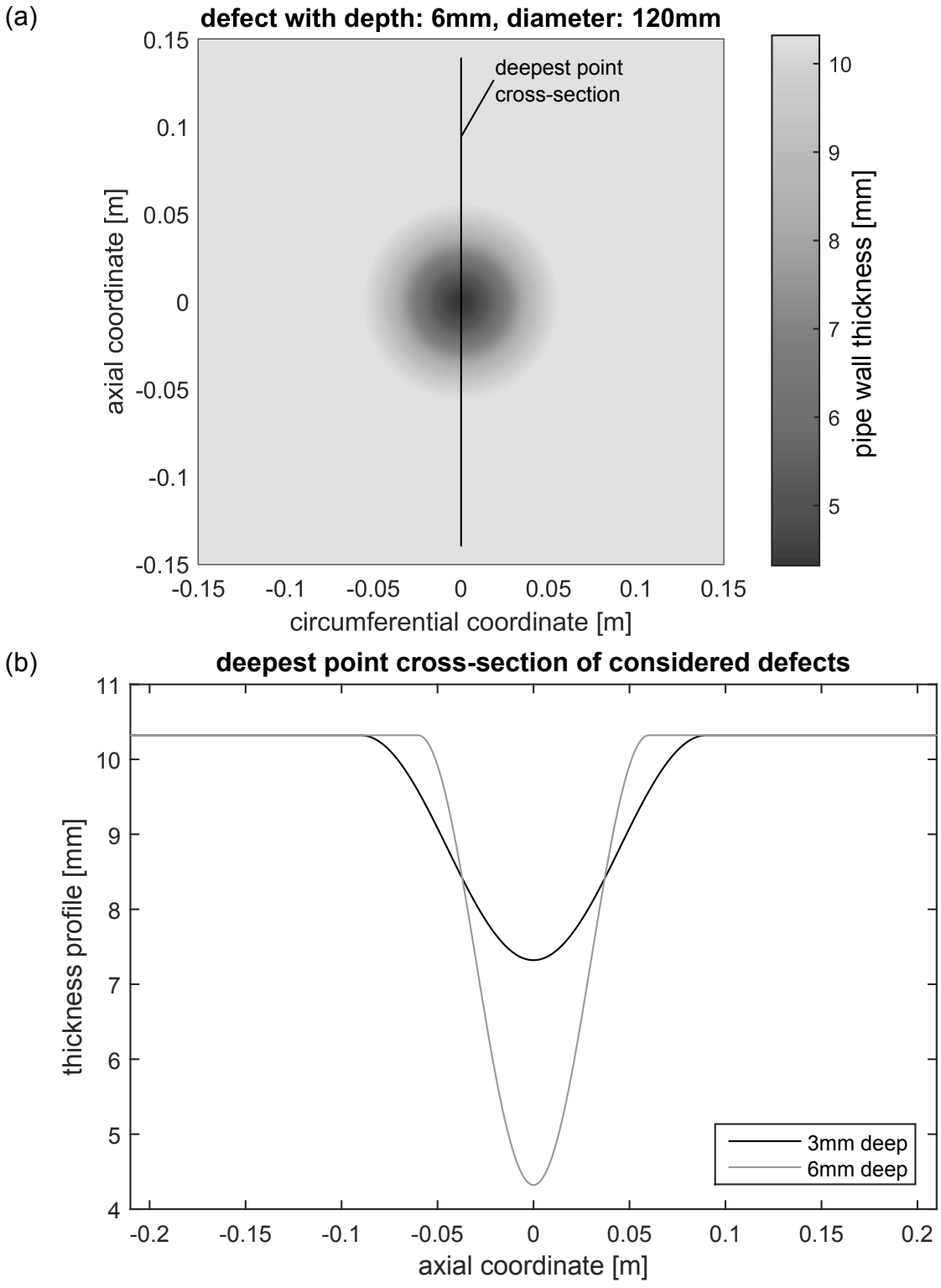

Figure 3.2: Overview of the considered pipe defects for the experimental measurements. In (a) the thickness map of the 6 mm deep defect is shown and the deepest point cross-section is illustrated, which is used for the comparison, as the deepest point is of interest. In (b) the deepest point cross-section (or also termed nominal thickness variation) for both considered defects, 3 mm and 6 mm deep, is pictured as a function of the axial coordinate.

Table 3.1: Overview of the two artificial defects considered for the experiments and the last column represents the lateral extend in terms of the A0 wavelength at the operation point. Defect 2 is also studied in [Huthwaite, 2014], where a reconstruction from experimental data, measured on a plate with a full view configuration is presented for the same operation point.

		lateral extent	
	maximum depth	absolute	rel. to A0 wavelength
defect 1	3 mm	180 mm	$4.8\lambda_{A0}$
defect 2	6 mm	120 mm	$3.2\lambda_{A0}$

is one critical parameter in judging the remaining service life. The axial cross-section is selected for the evaluation as a larger reconstruction error is expected along that direction. This is because of the limited-view array configuration and its orientation relative to the defect, such that along the axial cross-section, the effect of the missing viewing angles, which are estimated by the VISCIT algorithm, is greatest.

The deepest point cross-section for both defects considered here is pictured in Figure 3.2(b) as a function of the axial coordinate. From Figure 3.2(b), it can be seen that the defect exhibits a smooth variation of thickness and therefore allows for a better understanding of the performance and limitations of the tomography system, as the complexity of real defects is largely suppressed and therefore allowing for more fundamental insight. Also, no mode conversions (A0 to S0 mode) from sharp thickness changes are expected, favouring the acoustic assumption of the thickness reconstruction algorithm.

In the following, the deepest point cross-section of Figure 3.2(b) is also referred to as the nominal thickness variation and the dimensions of the two defects are listed in Table 3.1, where both the depth and diameter are listed. Defect 1 is 3 mm deep and has a lateral extent of 180 mm, which corresponds to about $4.8\lambda_{A0}$. Defect 2 is 6 mm deep with a lateral extent of 120 mm ($3.2\lambda_{A0}$) and is also featured in [Huthwaite, 2014], where a reconstruction from experimental data, measured on a plate using a full view configuration, is presented, allowing for a comparison with the limited-view reconstructions in this research. One thing to note about both defects is that their outer diameter is above the proclaimed resolution limit of approximately 1.5 to 2 wavelengths from [Huthwaite, 2014], for reconstruction of elastic waves fields with an imaging algorithm based on an acoustic wave propagation model.

3.2.2 Processing of Experimental Data

The measured experimental data is subjected to some signal processing before the tomography algorithm is run on the dataset for the thickness reconstruction. The measured time traces are first corrected for dispersion, using the algorithm presented in [Wilcox, 2003], where the amplitude-time traces are remapped to amplitude-distance traces, while removing the effects of dispersion to improve signal interpretation and reduce signal overlap (this is more helpful with strongly dispersive modes). The next processing step involves separating out the various helical orders that are to be used for the thickness reconstruction by employing the algorithm from [Huthwaite and Seher, 2015], that is briefly described earlier. Here, a total of seven orders are extracted from the original dataset, such that the 0th up to the ±3rd order are considered.

Having separated out the wave packets of the considered helical orders, in a next step a gradient-based minimisation scheme is used for calibration, which accounts for uncertainties in sensor positioning, phase shifts due to measurement electronics and material parameters. This approach is made possible as most wave paths between senders and receivers do not intersect with the artificial defect (or its replications for the higher order helical paths, see Figure 3.1(b)) and therefore should be unaffected by the defect. For these cases, the phase shift between the measured send-receive combinations and a simulated send-receive combination with uniform and nominal thickness should be zero. The calibration algorithm exploits this by fitting the sensor positions and phase velocity at nominal thickness of a uniform thickness plate model to the measured data starting off with the assumed positions and nominal phase velocity, minimising the phase shifts. This calibration is important, because the thickness reconstruction algorithm employs the phase shift relative to a pipe with uniform and nominal thickness for the computation and without the calibration, the reconstructions become corrupted. From a practical point of view, the question arises, when this calibration breaks down. The failure of the calibration is expected to depend on the number of send-receive paths which are affected by the defect. A large portion of the circumference would have to be covered by for example corrosion damage to significantly affect the calibration, as only a small number of send-receive paths are then unaffected and would yield a zero phase shift.

The thickness reconstruction algorithm HARBUT with VISCIT (because of the limited-view

problem) is applied to the calibrated data in the last step to determine the thickness map. The number of iterations for the HARBUT algorithm is selected to be six, as this yields the best compromise between the achievable result and the computational effort. The adaptive thresholding of VISCIT is adjusted automatically by the algorithm. The total time for one thickness reconstruction is found to take around 160 s on an Intel(R) Core(R) i7-3770 CPU and this is in vast contrast to the total time taken for the experimental data capture, which takes around 6.5 h, although it should be noted that neither process is optimised at present.

As a final remark, the dispersion curves used for the dispersion correction, helical path separation as well as, wave speed to thickness mapping in the tomography algorithm use standard steel parameters, which are also underlying for the dispersion curves illustrated in Figure 1.2. Experimental measurements of the dispersion curves have shown good agreement with the A0 mode dispersion curves from DISPERSE in the regarded range of frequencies.

3.2.3 Quantification of Thickness Reconstruction Quality

One implication of a smoothly varying and well defined artificial defect is that its location, shape and maximum depth are known apriori. This fact can be exploited to characterise and quantify the thickness reconstruction quality of the experiments relative to the known defect configuration and therefore some terms may be arbitrarily defined, which will be used later according to those definitions.

The term “detected” (“detection”) makes use of the fact that there is only one defect present within the area of interest and therefore there should only be one prominent feature in the thickness reconstructions. A defect is considered ”detected”, if there is one single feature with a maximum depth of more than 1.2 times of the wall thickness tolerance for the pipe (see [ASTM International, 2012]), which leads to a threshold value of approximately 1.4 mm.

The term “correctly located” (“location”) applies if the difference between the location of maximum depth in the reconstructed thickness map and the location of maximum depth of the artificial is less than 10 mm, as this is the grid size used in the thickness reconstruction. Another way to express this is to say that the maximum reconstructed depth is within one pixel from the maximum depth of the artificial defect.

The term “break down” of the thickness reconstruction refers to the state, for which the

defect is no longer correctly located. The criterion for detection may still be fulfilled as there now may be a single reconstruction artefact with a maximum depth of greater than 1.4 mm.

One mean to characterise the distortion of the thickness map due to reconstruction artefacts is to define a quality parameter for the deepest point cross-section, labelled as "cross-section" and for the whole thickness map labelled as "all pixel". Both are defined as the Frobenius norm, which is the square root the sum of the absolute squares of the matrix elements [Golub and Van Loan, 1996] (page 55), such that

$$||A||_F = \sqrt{\sum_{i=1}^{m}\sum_{j=1}^{n}|a_{ij}|^2}. \tag{3.5}$$

In equation (3.5), a_{ij} represents the difference between the nominal and reconstructed deepest-point cross-section or whole thickness map. For the computation of the quality parameter for the deepest-point cross-section, the second summation over j is omitted. The Frobenius norm can be used to measure the singularity of a matrix and will take lower values for matrices which are almost singular. This is exploited here, as the Frobenius norm converges to zero, when the discrepancy between nominal and reconstructed thickness decreases and therefore provides a measure for the quality of the reconstruction, where lower values are better with zero being a perfect reconstruction. The evaluation of the quality parameters looks at the discrepancy between the nominal thickness variation and the reconstructed thickness variation, however, only considers the discrepancy within less than 0.25 m of the deepest point in the reconstruction. The idea for this is that for any thickness map, the number of non-zero data points used in the computation of the Frobenius norm remains unchanged (given identical pixel sizes) and therefore eliminating the effect of an increasing number of data points with an increasing ring separations distance, which therefore leads to summing over more data points.

3.2.4 Initial Experimental Results

The reference measurements provide the ability to identify the achievable reconstruction quality and accuracy from experimental measurements in the absence of areas with restricted access, which can then be used to analyse their influence. The data capture is conducted

using the setup of Figure 2.13 with a nominal separation distance of the ring arrays of 1.162 m and the experimental results presented in this section are for both defects, which are listed in Table 3.1. It is to be noted that for the various other experiments where a different ring separation distance is considered, separate reference measurements have been conducted for the comparison.

The reconstructed deepest point cross-sections for both defects are illustrated in Figure 3.3(a) for the 3 mm deep defect and in Figure 3.3(b) for the 6 mm deep defect as a function of the axial coordinate, comparing the experimental reconstruction with the nominal thickness variation. From Figure 3.3 it can be seen that for both defects, the defect is detected and correctly located. When comparing the shape of the thickness reconstructions with the respective nominal thickness variations, good agreement is found in terms of the lateral defect extent near the surface between the reconstruction and the nominal thickness variation, in case of the 3 mm deep defect up to a depth of approximately 1.3 mm and in case of the 6 mm deep defect up to a depth of approximately 2.3 mm. However, the maximum depth, which is one parameter of interest, is underestimated for both defects, more severely for the 6 mm deep defect. This is also clear from Table 3.2, where the maximum depth (equal to nominal thickness minus deepest point thickness) is listed for both defect. The defect depth is underestimated by approximately 20% for the 3 mm deep defect and approximately 35% for the 6 mm deep defect respectively, when relating the error in the maximum depth to the nominal defect depth. From the quality parameter in Table 3.2, it can also be seen that the reconstruction quality is better for the 3 mm deep defect in comparison to the 6 mm deep defect, which is expected due to the smaller contrast and larger extent and should therefore be easier to reconstruct. This comparison also serves as a check for plausibility for the quality parameter.

Table 3.2: Overview of the reference measurements for both defects from Table 3.1 and a ring separation distance of 1.162 m. The maximum depth is the maximum reconstructed depth and the quality parameter uses the Frobenius norm [Golub and Van Loan, 1996] for the deepest point cross-section (cross-section) and the total thickness map (all pixel).

	maximum	quality parameters	
defect depth	depth	cross-section	all pixel
3 mm defect	2.4 mm	1.7	6.7
6 mm defect	3.9 mm	3.8	9.0

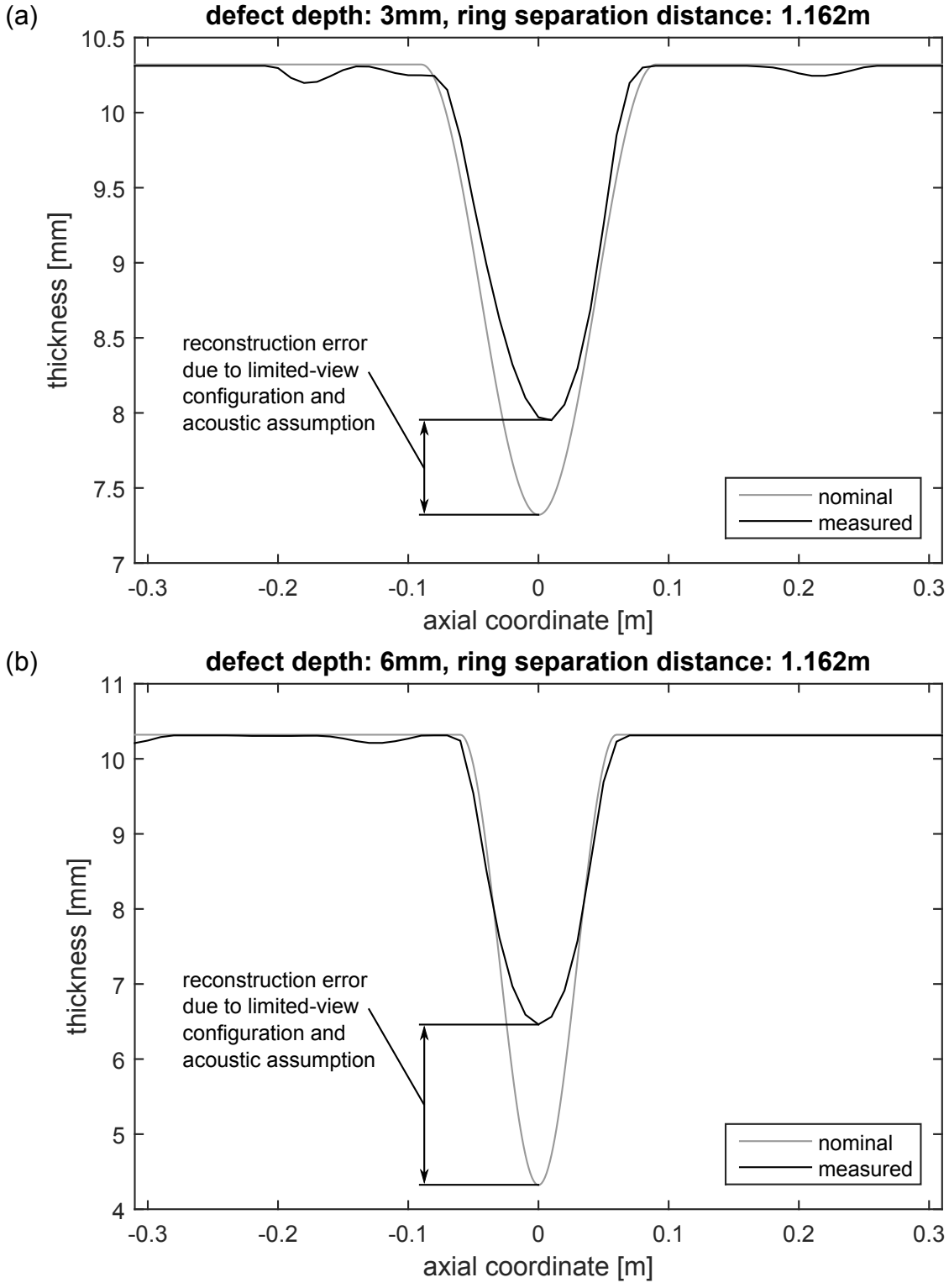

Figure 3.3: Deepest point cross-section for reference measurements, for defect 1 (3 mm deep) in (a) and defect 2 (6 mm deep) in (b), comparing the experimental reconstructions with the nominal thickness variation from Figure 3.2(b). For both reconstructions, the location and lateral extent is estimated accurately, however, the maximum depth is underestimated.

The main reason as to why the defect depth from the experimental reconstructions is underestimated is the limited-view configuration of the guided wave tomography system. The limited-view configuration occurs as the region of interest lies between two linear arrays and therefore certain viewing angles onto the defect are missing, as discussed earlier and illustrated in Figure 3.1(b). The implications of the limited-view configuration can be studied by a comparison to a full view reconstruction from experimental data as presented in [Huthwaite, 2014] for the 6 mm deep defect and the same operation point as regarded here. In [Huthwaite, 2014] a 6 mm deep defect with 120 mm lateral extent identical to the one considered here (see defect 2 in Table 3.1) is machined onto a 10 mm thick steel plate and a circular array of 64 sensors and with 180 mm radius is placed around the axisymmetric defect. The discrepancy in nominal wall thickness of 0.321 mm between the schedule 40 pipe wall considered here and the 10 mm steel plate is disregarded for the comparison and in an experimental study presented in Appendix A, it is found that the average wall thickness of the pipe is around 10 mm. From the deepest point cross-section (Figure 12(b) in [Huthwaite, 2014]), a defect depth of 5.35 mm is found, which corresponds to a reconstruction error of approximately 11% relative to the nominal defect depth. The remaining discrepancy there is attributed to the difference between the elastic and the acoustic scattering, as an acoustic reconstruction algorithm is employed to image elastic scattering data.

It is therefore expected that the limited-view configuration explains the additional reconstruction error relative to a full view configuration for which the spatial sampling criterion fulfilled. The direct comparison between the reconstructions of the same defect considered here and in [Huthwaite, 2014] shows that with the limited-view setup of this research, the reconstruction error increases by a factor of approximately three. A second source of error is the assumption of acoustic scattering to approximate the elastic scattering, which additionally contributes to the reconstruction error, as discussed earlier. Nonetheless, the defect is always detected and accurately located.

A potential further source of error in the thickness reconstructions that needs to be acknowledged is the plane wave assumption, which is made as part of the reconstruction algorithms. Since the array elements exhibit an omni-directional radiation pattern and at the point of interaction of the excited wave front with the defect, the plane wave assumption may not hold true. Further investigations into the reconstruction algorithms would be necessary, with potential adaptations of the algorithm, in order to quantify the effect of this source of

error, but are omitted here as these are beyond the scope of this project.

Another aspect that can be considered when comparing the reference measurement on the 6 mm deep defect with the study presented in [Huthwaite, 2014] is the spatial sampling of the wave field. In [Huthwaite, 2014], two adjacent sensors in the array are separated by less than half the A0 wavelength at the operation point and the spatial sampling criterion for circular arrays fulfilled [Simonetti et al., 2007] (a coarser spacing would have also been sufficient, given the dimensions of the defect and in accordance with [Simonetti et al., 2007]). For the study here, the distance between two sensors is just over one A0 wavelength and therefore the Shannon-Nyquist sampling criterion is violated. This generally leads to more reconstruction artefacts, because fewer data points within the Ewald limiting sphere (describes the wave number components space that can be obtained from the reconstruction from the measurement of the scattered field in a full view configuration) [Kak and Slaney, 2001] are available for the reconstruction in comparison to higher spatial sampling, rather than additional reconstruction errors.

3.3 Experimental Studies of Practical Issues

The experimental studies look at the aspect of robustness for the data capture, with focus on the repeatability of measurements, ring array separation distance and location of the defect relative to the ring arrays, which are important aspects for practical applications. Further, the robustness of the thickness reconstructions is explored for errors in the position of individual sensors within the ring arrays, as well as the misalignment of the whole array.

3.3.1 Repeatability of Measurements

The repeatability of measurements is important for practical applications, as it is desired to measure the same result for the same, but independent, experimental setup, with the aim to give confidence in the accuracy of the thickness reconstructions. The goal of this study is to understand the variation in the reconstructed thickness map, based on various datasets captured for the same experimental setup (identical nominal ring separation distance).

The experiments for this study are conducted on the pipe with the 6 mm deep defect (see Table 3.1) and the transducer rings are separated by 1.162 m with the defect located in

the middle between both ring arrays. For each repeat measurement, all transducers of both ring arrays are removed and reattached, in order to ensure independent experimental measurements and a total of eight independent datasets are captured for the analysis.

In Figure 3.4, the deepest point cross-section for all eight measurements is depicted in black and compared to the nominal thickness variation. From Figure 3.4, it can be seen that all eight curves line up on top of each other, implying good repeatability. This can be further investigated by comparing the maximum reconstructed depth and quality parameters for all eight measurements with each other, which are listed in Table 3.3. Both the maximum defect depth and the quality parameter for the deepest point cross-section are almost identical for all eight measurements and only vary marginally, 0.1 mm for the maximum depth and 0.2 for the deepest point cross-section. The quality parameter for the whole thickness map exhibits slightly larger variations of 0.9, however, this is an expected result, given the dependence of this parameter on the whole thickness map.

From these results it can additionally be concluded that a variation of 0.2 for the deepest

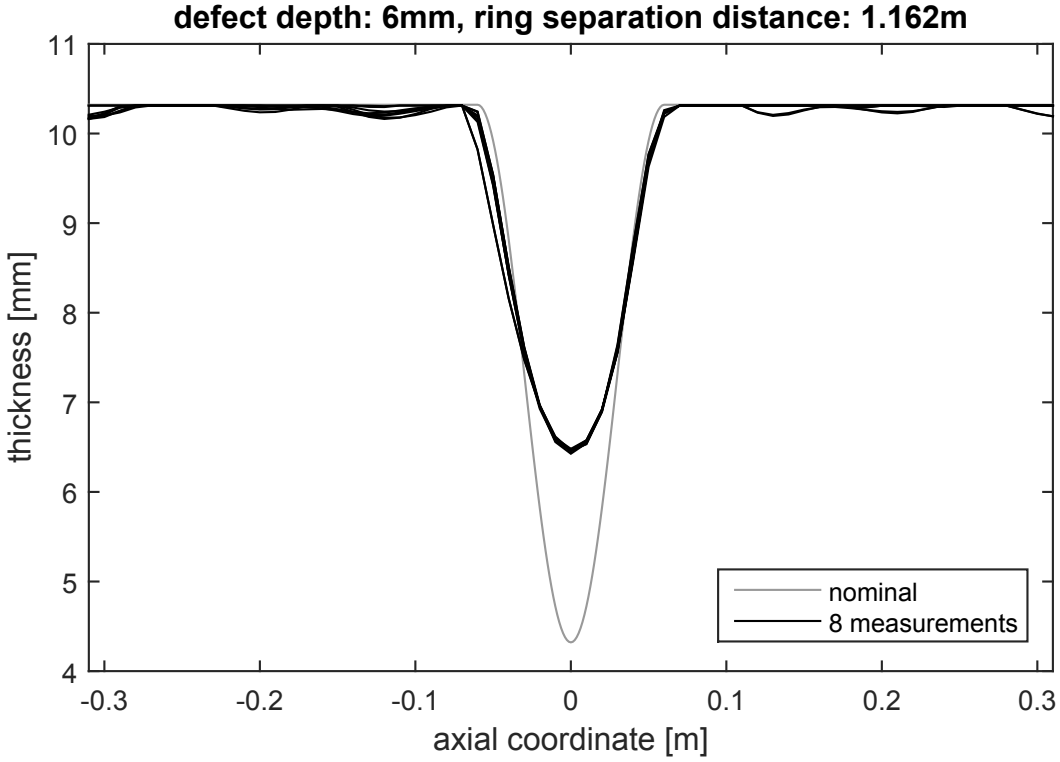

Figure 3.4: Deepest point cross-section for all eight repeatability measurements conducted on the 6 mm deep defect with a ring separation distance of 1.162 m and compared to the nominal thickness variation. The measured deepest point cross-sections are illustrated in black and only one label is listed in the legend for clarity.

Table 3.3: Overview and results of all eight repeatability measurements with 1.162 m ring separation distance on the pipe with the 6 mm deep defect. The maximum depth is the maximum reconstructed depth and quality parameter uses the Frobenius norm for the deepest point cross-section (cross-section) and the total thickness map (all pixel).

experiment number	maximum depth	quality parameters	
		cross-section	all pixel
#1	3.9 mm	3.8	9.0
#2	3.8 mm	3.9	9.2
#3	3.9 mm	3.8	9.2
#4	3.9 mm	3.8	9.0
#5	3.9 mm	3.8	9.2
#6	3.9 mm	3.8	9.1
#7	3.9 mm	4.0	9.9
#8	3.9 mm	4.0	9.9

point cross-section and 0.9 for the whole thickness map can be considered small, because this is the observed range of variation for the same experiment. This finding can be used as a threshold for understanding the influence of for example support locations on the thickness reconstructions, such that if the variation of the quality parameter is similar to that from the repeatability measurements, there is at most a small influence. It needs to be remarked that this threshold is established for a specific ring separation distance and may be slightly different for other ring separation distances.

As a result from this study, it is found that the measurements are very repeatable and further tests on the 3 mm deep defect pipe have shown the same result in terms of the repeatability. The good repeatability of the measurements is an expected result, because it is expected that the position calibration during the data processing accounts for potential position errors of various sensors in the arrays.

3.3.2 Sensor Ring Separation Distance

A range of ring separation distances may been considered for the experiments, mainly because of the nature of the areas with restricted access. In this section, the influence of the ring separation between the two ring arrays on the thickness reconstruction is studied, when the arrays are located symmetrically around the defect. The ring separation distance influences the extent of the limited view problem, as for shorter ring separation distances, there are more viewing angles available onto the defect for the reconstruction. At the same

time, the angular sampling worsens, since the angle between two consecutive transducers and the defect centre increases with decreasing distance between the defect and the arrays.

The experiments for this study are conducted on the 6 mm deep defect pipe (see Table 3.1) and the ring separation distance is varied between 0.562 m, 0.802 m and 1.162 m. The ring separation distances results from the dimensions of the EMAT housing (photograph see Figure 2.12) and help in the more accurate positioning of the transducers. This is because of the fact, that positioning and aligning the measurement tapes, for the precise positioning of the arrays, is achieved more accurately if the measurement tapes are separated by a full centimetre distance. The distance from the measurement tape to the centre of the EMAT coil is given by 19 mm and therefore resulting in these nominal ring separation distances.

Figure 3.5 shows the deepest point cross-section for the various ring separation distances considered and also the nominal thickness variation. From Figure 3.5 it can be seen, that with increasing ring separation distance, the reconstructed depth decreases slightly (by about 0.4 mm), however, the shape of the reconstruction is mostly uninfluenced. The decrease in the reconstructed depth as a function of the increasing ring separation distance is also

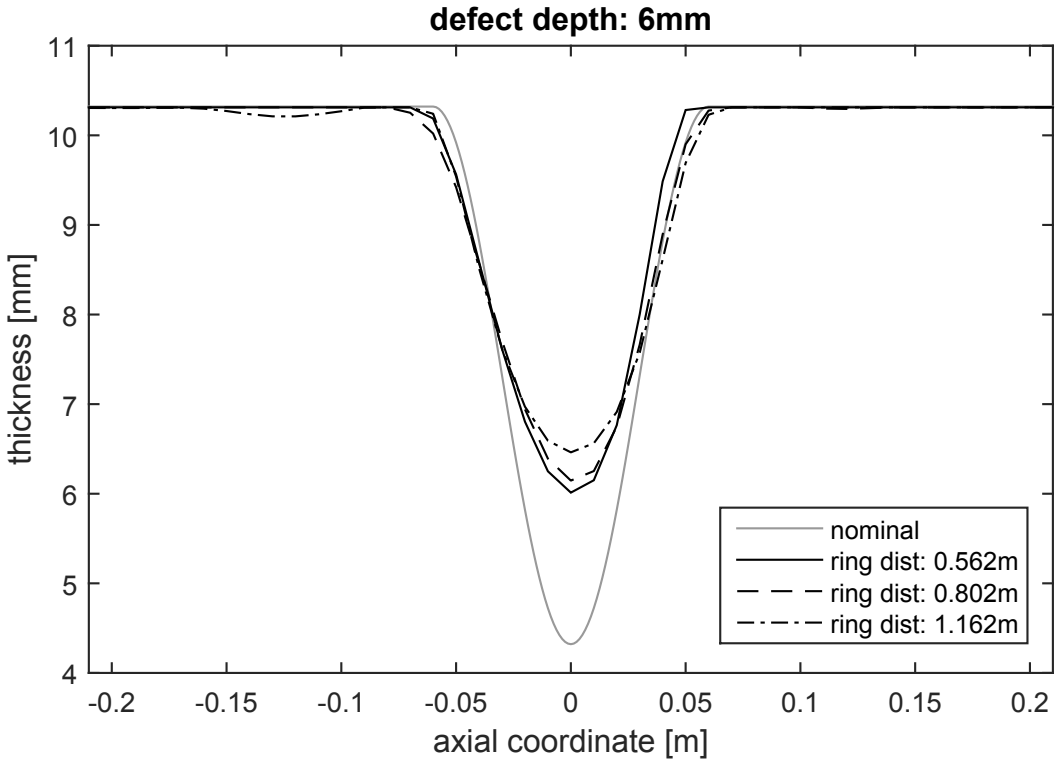

Figure 3.5: Deepest point cross-section for various ring separation distance experiments conducted on the 6 mm deep defect and compared to the nominal thickness variation.

Table 3.4: Overview and results of ring separation distance measurements on the pipe with the 6 mm deep defect. The maximum depth is the maximum reconstructed depth and quality parameter uses the Frobenius norm for the deepest point cross-section (cross-section) and the total thickness map (all pixel).

ring separation distance	maximum depth	quality parameters	
		cross-section	all pixel
0.562 m	4.3 mm	3.2	7.5
0.802 m	4.2 mm	3.4	8.5
1.162 m	3.9 mm	3.8	9.0

listed in Table 3.4 as well as the quality parameters for the various ring separation distances. The decrease in the reconstructed depth means an increase in the reconstruction error of the maximum depth relative to the nominal defect depth and in the case here, an increase from 28% for a ring separation distance of 0.562 m to 35% for a ring separation distance of 1.162 m is found. The increase in the quality parameters may also be explained with the increasing ring separation distance, as the viewing angle onto the defect decreases, causing further reconstruction errors, mainly due to a minor increase in reconstruction artefacts.

As a conclusion from this study, the shortest possible ring separation should be selected, within limits, in order to improve the accuracy of the thickness reconstructions. The limitations on the shortest ring separation distance may include the near field of the transducer, which should be far enough away from the region of interest in order to avoid near field effects. Another important limitation is that for short ring separation distances, the higher order helical paths may intersect multiple times with the defect, which may corrupt the signal processing (helical path separation and position calibration) and in turn corrupt the reconstructed thickness. A study on the 3 mm deep defect pipe with various ring separation distances has shown similar results to the 6 mm deep defect pipe.

3.3.3 Non-symmetric Location of Defect between Arrays

In all the previous studies, it is assumed that the two ring arrays are aligned symmetrically around the defect, such that the defect is in the middle between both arrays. For practical applications, this may not always be the case and in this section, the influence of the defect being closer to one of the two arrays on the thickness reconstruction is investigated.

The experiments for this study are conducted on the 3 mm deep defect pipe (defect charac-

teristics see Table 3.1) with a ring separation distance of 0.602 m. Three experiments with the same ring separation distance are considered: a reference measurement, where the defect lies symmetrically between the two arrays and two asymmetrical arrangements, where the centre of the defect is offset in the axial direction by 0.1 m towards both the transmitting and receiving array. This leads to a split distance of 0.201 m and 0.401 m between the centre of the arrays and defect respectively in the axial direction. The shortest distance between the array and the edge of the defect therefore is around 110 mm, which is just over one S0 wavelength at the operation point of the guided wave tomography system, or approximately two and three quarter A0 wavelengths. This is important, as in case the defect is too close to the transmitter array, the A0 Lamb mode may not have fully developed after the excitation at the transmitter location, and this is to be avoided when operating the guided wave tomography system. In case of the defect being too close to the receiver array, near field effects may be observed at the receiver location that may also complicate the signal

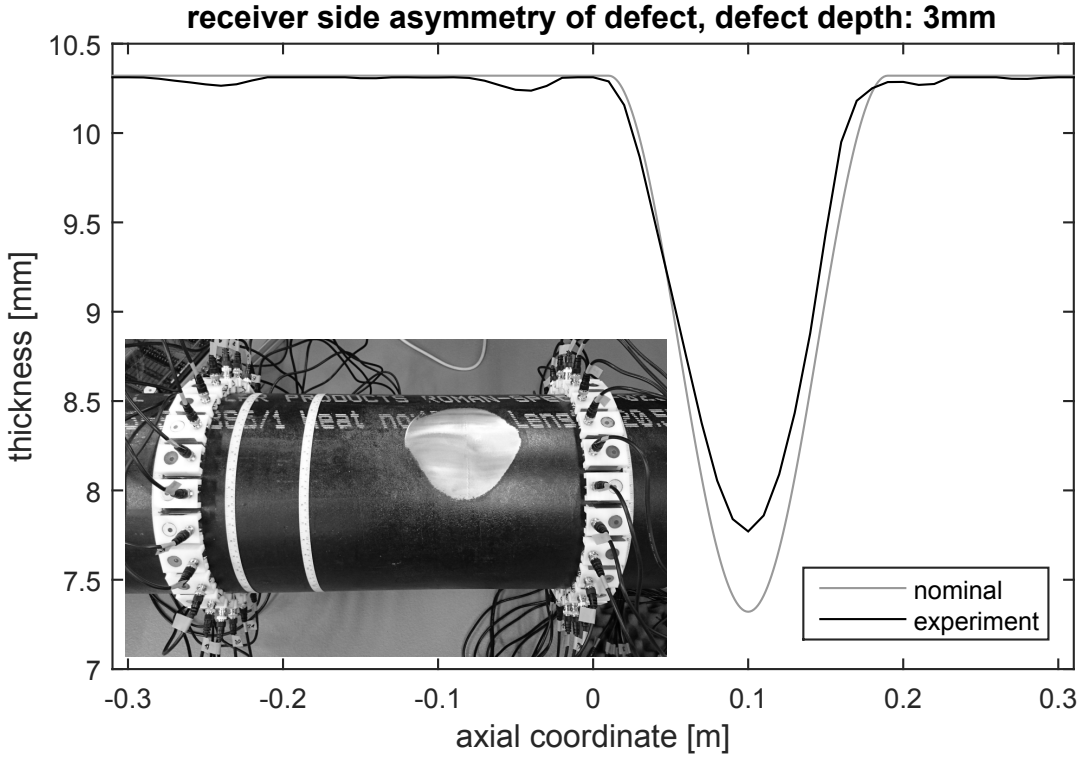

Figure 3.6: Deepest point cross-section for receiver asymmetry with a ring separation distances of 0.602 m, conducted on the 3 mm deep defect pipe and compared to the nominal thickness variation. The receiver array is located on the positive side of the axial coordinate and the origin of the axial coordinate symmetrically between both arrays (array axial coordinates of ±0.301 m). The inset shows a photograph of the arrangement of the two arrays from the experiment, with the receiver ring closer to the defect.

Table 3.5: Overview and results of measurements for an asymmetric location of the defect between the ring arrays on the pipe with the 3 mm deep defect and a ring separation distance of 0.602 m. The maximum depth is the maximum reconstructed depth and quality parameter uses the Frobenius norm for the deepest point cross-section (cross-section) and the total thickness map (all pixel).

symmetry condition	maximum depth	quality parameters	
		cross-section	all pixel
rx side asymmetry	2.6 mm	1.3	5.1
tx side asymmetry	2.6 mm	1.2	6.2
symmetric	2.6 mm	1.2	5.7

processing. For that reason, a minimum distance between the ring array and the defect of over two A0 wavelengths is proposed, in conjunction with the findings based on simulations illustrated in Figure 2.3.

In Figure 3.6, the deepest point cross-section for the case of a receiver side asymmetry is depicted as a function of the axial coordinate and compared to the nominal thickness variation. The reference frame for the discussions in Figure 3.6 is located symmetrically between the two arrays, such that the defect is located at an axial coordinate of 0.1 m. From Figure 3.6 it can be seen that the defect is detected and correctly located at 0.1 m. When comparing the shape of the thickness reconstructions with the nominal thickness variation, good agreement is found in terms of the lateral defect extent near the surface between the reconstruction and the nominal thickness variation up to a depth of approximately 1.3 mm. Similar to all previous experiments, the depth of the defect is underestimated and in Table 3.5 all three experiments considered for the comparison are listed, comparing the maximum depth as well as the quality parameters for the deepest point cross-section and whole thickness map. From Table 3.5 it can be seen that the maximum reconstructed depth for both asymmetric cases match that of the symmetric reference measurement and a similar behaviour is found for the quality parameters, which only exhibit a small variation.

From the findings above, it can be inferred that the influence of the location of the defect between the two arrays on the thickness reconstruction is small in terms of the variation of the maximum depth and quality parameters, given the size of the defect and the distance to the ring arrays. From a practical point of view, this finding is beneficial, however, in order to avoid any potential issues relating to corrupted reconstructions, a sensible aim should be to position the rings such that the defect lies symmetrically between the two ring arrays.

This is because of defects that cover larger parts of the circumference and therefore, if closer to either of the arrays (especially the transmitter array), will cause more send-receive paths to be affected by the defect than in the symmetric case. This may therefore corrupt the position calibration, which relies on a large number of send-receive paths to be unaffected by the defect.

3.3.4 Influence of Sensor and Array Misalignments

In the data processing of the measured datasets, the position calibration, which has been discussed in the previously, plays an important role for the robustness of the thickness reconstructions and in this section the limits of the ability to compensate for sensor misalignments within the expected experimental conditions are explored. This is important, because it allows for the determination of the required precision of the sensor positions within the array or the alignment of the array itself for the experimental measurements. Here, three experimental cases are considered, a single sensor position error, a systematic and an unsystematic misalignment of the sensors within an array.

3.3.4.1 Single Sensor Position Error

In this study, the influence of a position error of a single sensor on the thickness reconstructions is studied and the effectiveness of the position calibration to compensate for the position error is assessed.

The experiments are conducted using the 3 mm deep defect pipe (see Table 3.1) with a ring separation distance of 0.602 m and the position error is introduced by axially shifting one of the sensors on the receiver array towards the transmitting array, as seen from the inset in Figure 3.7. Since only one sensor is moved while the position for the other sensors remains unchanged, only the send-receive pairs for the shifted receiver need to be remeasured for every new dataset with a new position error. Based on the experimental setup here, the data capture is faster for a shifted receiver, because the transmitter array can be multiplexed automatically, unlike the receiver array. Nonetheless, it is expected that similar results would be obtained for a shifted transmitting sensor. The sensor position error is selected to be an axial shift for simplicity and due to the fact that there is only limited space available for a circumferential shift. The position error is varied from 0 mm in steps of 10 mm to 40 mm,

which corresponds to a maximum shift of one A0 wavelength at the operation point of the guided wave tomography system.

In Figure 3.7, the deepest point cross-section from the reconstructed thickness maps is illustrated for the various position errors and compared to the nominal thickness variation. From Figure 3.7, it can be seen that the curves for the no error case and the various position errors denoted by their shift generally match well (outside the defect region) and very well in the defect region. In comparison to the nominal thickness variation, the defect is detected and correctly located. Both the shape of the defect as well as the maximum defect depth show good agreement with the no error case, which can also be seen from Table 3.6. In Table 3.6, the maximum depth and the quality parameters for both the deepest point cross-section and total thickness map are listed and it can be seen that there is no significant variation (0.1 mm for the maximum depth, 0.2 for the cross-section quality parameter and 0.6 for the whole thickness map quality parameter) as a function of the axial shift. This implies that

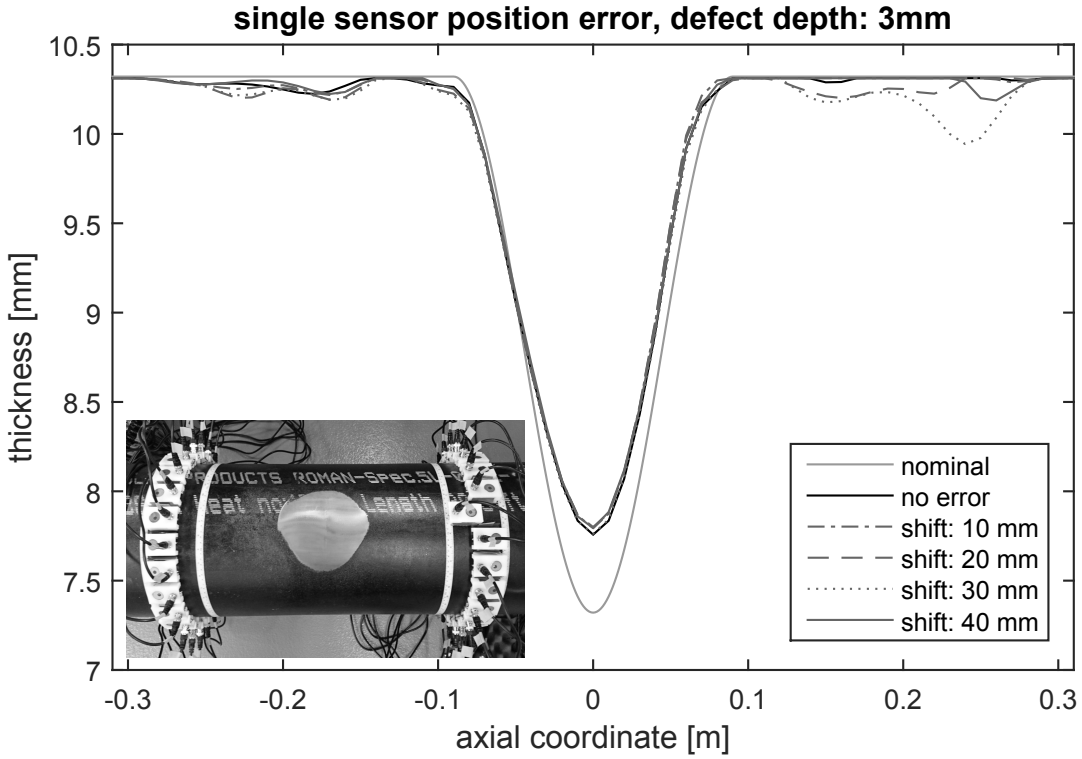

Figure 3.7: Deepest point cross-section for the single sensor position error measurements with a ring separation distances of 0.602 m, conducted on the 3 mm deep defect and compared to the no error case and nominal thickness variation. The inset shows a photograph of the experimental setup and the axial position of the shifted sensor is varied from 0 mm to 40 mm towards the transmitter array.

Table 3.6: Overview of single sensor position error measurements and results on the pipe with the 3 mm deep defect and a ring separation distance of 0.602 m. The maximum depth is the maximum reconstructed depth and quality parameter uses the Frobenius norm for the deepest point cross-section (cross-section) and the total thickness map (all pixel).

axial shift of sensor	maximum depth	quality parameters	
		cross-section	all pixel
no error	2.6 mm	1.2	5.3
shift: 10 mm	2.5 mm	1.4	5.3
shift: 20 mm	2.5 mm	1.4	5.4
shift: 30 mm	2.6 mm	1.4	5.8
shift: 40 mm	2.5 mm	1.3	5.9

in terms of the three analysed parameters, there is only a very small influence of position error for a single sensor on the thickness reconstruction, as the position calibration is able to compensate for the position error.

These results may be explained with the problem considered itself, as for a position error of a single sensor, only $(2N+1)^2M$ send-receive combinations out of $((2N+1)M)^2$ (M is the number of sensors per array, N is the highest helical order) are affected relative to the assumed "correct" sensor position (no sensor position error). In the case here this corresponds to less than 4.2% of the total send-receive combinations being affected and there are therefore enough unaffected send-receive combinations to overcome the single sensor position errors. In conclusion, the influence would be expected to be small, even for large position errors of approximately one A0 wavelength and the sensor position error can be compensated for by the position calibration.

3.3.4.2 Array Inclination - Systematic Misalignment

In the previous study, it is found that the influence of a position error for a single sensor is very small on the thickness reconstructions. In this study, the case of a systematic error in sensor position for the whole array is studied for the example of an inclined transmitter array and its influence on the thickness reconstruction is assessed under consideration of the position calibration. The array inclination is defined as the angle with the pipe axis (axial direction) with the normal vector of the plane on which all array sensors are located on the outside of the pipe.

The experiments are conducted on the 3 mm deep defect pipe and for the sensor positioning,

the array inclination is approximated with axial offsets for the various array sensors, neglecting the circumferential shifts in favour of higher position accuracy within the inclined configuration and to reduce additional unsystematic errors. The maximum axial shift of the inclined transmitter array is set to 40 mm, which corresponds to approximately one A0 wavelength at the operation point and represents an extreme case for the inclination. The inclined array is illustrated in the inset in Figure 3.8, where the misalignment of the array is clearly visible. The ring separation distance for the reconstruction of the experimental data assumes the mean axial position of the inclined array, which is half the maximum offset (20 mm) less than the largest ring separation distance between the array sensors of the transmitting array and the receiving array, such that the ring separation distance employed equals to 0.582 m.

Figure 3.8 shows the deepest point cross-section for the reconstruction with the inclined

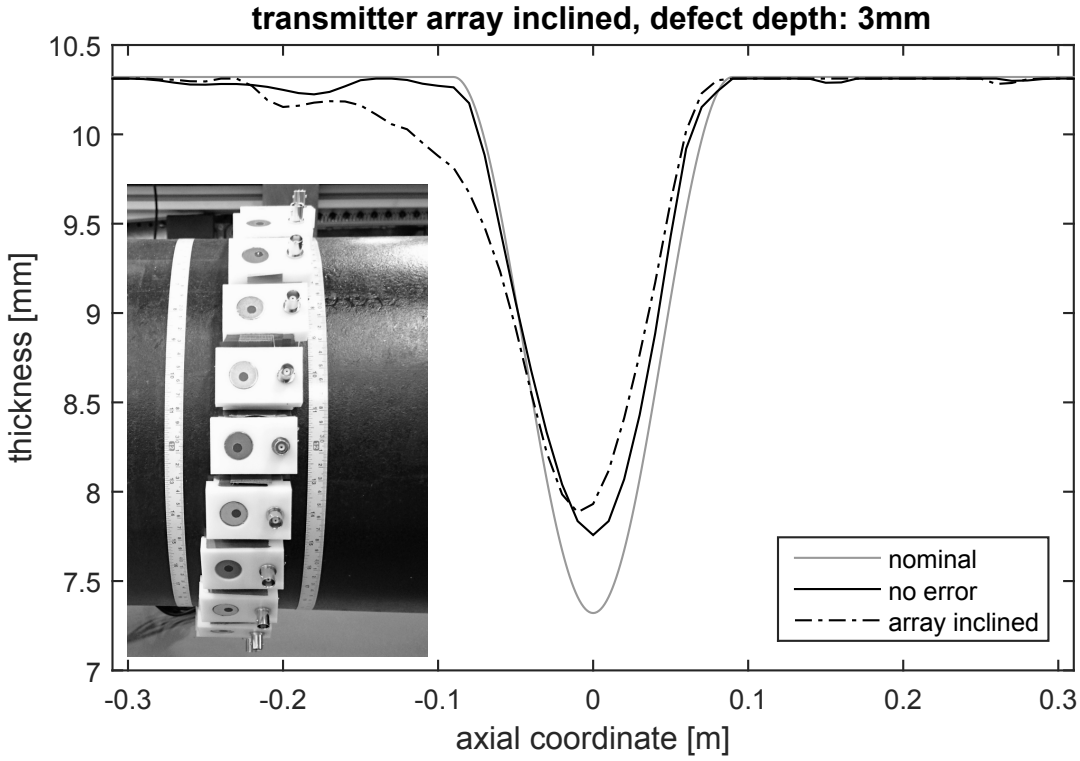

Figure 3.8: Deepest point cross-section for transmitter array inclination measurements with a ring separation distances of 0.582 m for the computation, conducted on the 3 mm deep defect and compared to the no error case (ring separation distance of 0.602 m) and nominal thickness variation. The maximum axial shift within the array is selected to be 40 mm, which corresponds to one A0 wavelength at the operation point. The inset shows a photograph of the experimental setup, before the cables are attached, and gives an idea of how strongly the array is inclined.

Table 3.7: Overview of array inclination measurements and results on the pipe with the 3 mm deep defect and a ring separation distance of 0.582 m for the computation and 0.602 m for the no error reference measurement. The maximum depth is the maximum reconstructed depth and quality parameter uses the Frobenius norm for the deepest point cross-section (cross-section) and the total thickness map (all pixel).

alignment error	maximum depth	quality parameters	
		cross-section	all pixel
no error	2.6 mm	1.2	5.3
tx array inclined	2.4 mm	2.2	8.1

array and a comparison to a reference measurement (0.602 m ring separation distance) and the nominal thickness variation.

From Figure 3.8, it can be seen that, when comparing the inclined array case with the nominal thickness variation, good agreement in terms of the shape up to a depth of 1.3 mm is found on the receiver array side (positive axial coordinate) and the thickness is underestimated slightly on the side of the transmitter array (negative axial coordinate). However, defect is detected and correctly located. In comparison to the no error reference case, further underestimation of the maximum depth is found for the inclined array case. This can be assessed further, when considering Table 3.7, where the maximum depth as well as the quality parameters for the deepest point cross-section and whole thickness map are listed. From Table 3.7, the slight decrease in the maximum depth of 0.2 mm can be seen, as well as the increase in the quality parameters by 1.0 for the deepest point cross-section (2.8 for the whole thickness map), also due to more reconstruction artefacts in the thickness map. This implies that, in terms of the three analysed parameter, there is a small influence of the systematic sensor position error due to the inclined array on the thickness reconstructions.

As a conclusion from this study and for practical considerations, a systematic sensor position error should be avoided, to ensure better accuracy of the reconstructions. Nonetheless, it needs to be noted that the thickness reconstruction only loses accuracy (in terms of maximum depth and quality parameters), but does not break down, relative to a no error reference measurement. The position calibration helps to reduce the errors in the reconstructions, however, cannot fully compensate for the position errors in comparison to the no error case. In theory, it should be possible to individually account for the various sensor positions, but this is not feasible from a practical point of view, as the individual sensor positions would have to be determined apriori, increasing the effort and complexity of data

capture. Since the array inclination is rather large and easily visible from the experiment, it is expected that with a smaller inclination, the error should be less pronounced. Similar results would also be expected in case the receiver array is inclined due to reciprocity.

3.3.4.3 Arbitrary Sensor Positions - Unsystematic Misalignment

The arbitrary sensor position test looks at unsystematic sensor position errors for all sensors within each array and their influence on the thickness reconstruction, similar to the inclined array study, where a systematic position error is considered. The starting point for this study is the case of two parallel arrays and each array sensor is superimposed with a position error in axial and circumferential direction to obtain a pseudo-random or arbitrary arrangement of both arrays.

The experiments for this study are conducted on the 3 mm deep defect pipe and the starting ring separation distance without the superimposed position errors is assumed to be 0.550 m, which is also the ring separation distance employed for the computation of the thickness map. Each sensor of both arrays is then shifted by up to ±10 mm in the axial and circumferential directions, which may lead to a maximum error in terms of the propagation distance of ±20 mm, when considering the position error in both arrays. This corresponds to approximately plus or minus half the A0 wavelength at the given operation point. The inset in Figure 3.9 shows a photograph of the experimental sensor arrangement for one of the arrays and illustrates the extent to which the various sensors are misaligned.

Figure 3.9 illustrates the deepest point cross-section for reconstruction of the arbitrary sensor position measurement, and a comparison with a no error reference measurement with 0.602 m ring separation distance as well as the nominal thickness variation is depicted. For the arbitrary sensor position case, from Figure 3.9 it can be seen that the defect is detected and correctly located. When comparing the shape of the thickness reconstructions with the nominal thickness variation, good agreement is found in terms of the lateral defect extent near the surface between the reconstruction and the nominal thickness variation up to a depth of approximately 1.3 mm. The comparison to the no error reference measurement shows a slight decrease in the maximum defect depth by 0.2 mm, but otherwise generally good agreement. This is also observed from Table 3.8, where the maximum depth and both quality parameters are listed for the arbitrary sensor position and the no error reference

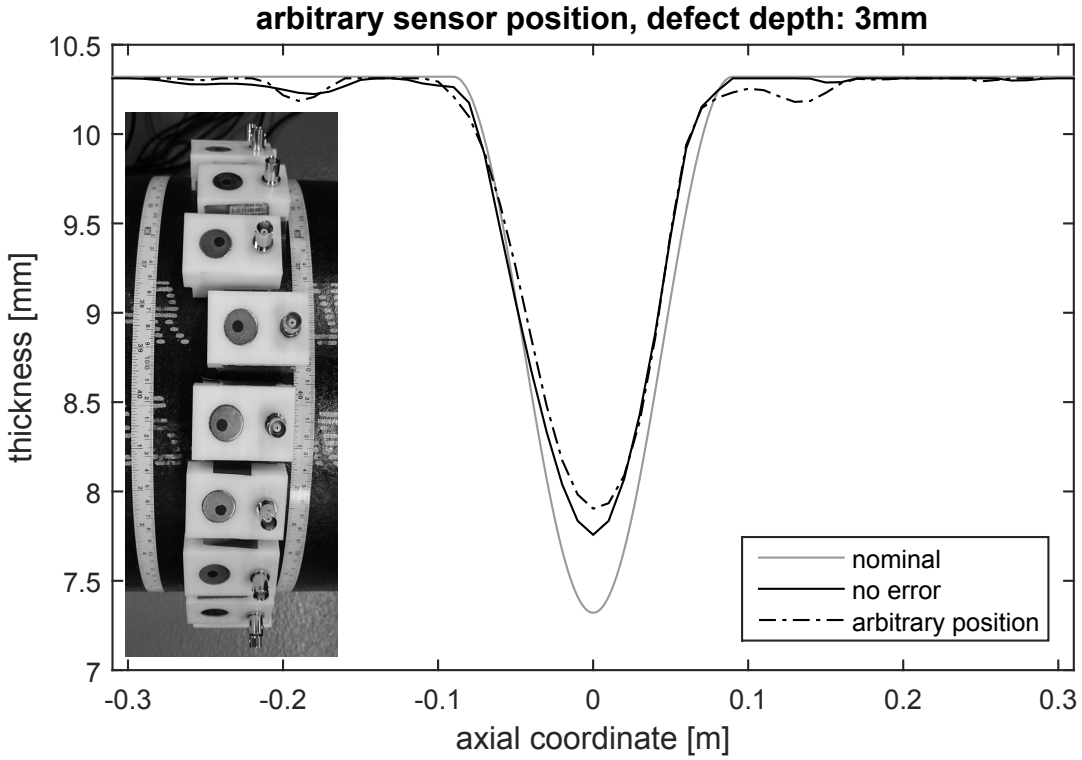

Figure 3.9: Deepest point cross-section for arbitrary sensor position measurements with a ring separation distances of 0.550 m for the computation, conducted on the 3 mm deep defect and compared to the no error case (ring separation distance of 0.602 m) and nominal thickness variation. The maximum position error may be ±10 mm in axial and circumferential direction. The inset shows a photograph of the experimental setup, before the cables are attached, and gives an idea of how strongly the sensors in the array are misaligned.

measurement. From Table 3.8 it can be seen that beside the decrease in the maximum defect depth, the quality parameters only increase slightly (deepest point cross-section by 0.2; whole thickness map by 0.9), as there are slightly more but only minor reconstruction artefacts.

These observations imply that in terms of the three analysed parameters, there is a small influence on the thickness reconstruction due to the sensor position errors relative to the no error reference measurement, which however does not lead to the breakdown of the reconstruction. The position calibration is able to compensate for some of the sensor position errors, but not as well as in the case of the no error reference measurement. The error in the maximum depth caused by the sensor position error relative to the reference measurement is similar to that of the inclined array study with a systematic position error. In case of the systematic position error, however, the reconstruction quality is slightly worse (larger increase in quality parameters) than in the case the unsystematic error. One possible ex-

Table 3.8: Overview of arbitrary sensor position measurements and results on the pipe with the 3 mm deep defect and a ring separation distance of 0.550 m for the computation and 0.602 m for the no error reference measurement. The maximum depth is the maximum reconstructed depth and quality parameter uses the Frobenius norm for the deepest point cross-section (cross-section) and the total thickness map (all pixel).

sensor position error	maximum depth	quality parameters	
		cross-section	all pixel
no error	2.6 mm	1.3	5.3
arbitrary sensor positions	2.4 mm	1.5	6.2

planation for this may be that the variance of the position error for the systematic position error study is larger than that of the unsystematic position error study.

Since the position error considered in this study are clearly visible, for practical purposes it is expected that an operator would notice errors in sensor position of that magnitude (see inset of Figure 3.9). Nonetheless, a successful reconstruction of the measured data is possible and it could be shown that the position calibration is robust to a maximum sensor position error of around plus or minus a quarter of the A0 wavelength. As a conclusion, for smaller sensor position errors, the influence on the thickness reconstructions is expected to be smaller and therefore the tolerance on the position accuracy may be slightly relaxed for practical purposes.

One drawback of the presented study is that only one configuration of arbitrary sensor positions has been studied and for statistical significance, more experiments would be necessary. These could also be conducted numerically (see later sections) under the constraint of the spatial extent of the transducers due to their housing, such that they do not overlap. However, it is expected that for most configurations based on the same statistical distribution in terms of the sensor position error, similar results as presented in the case above would be found.

3.3.4.4 Summary of Sensor Misalignment

The above presented studies for a single sensor misalignment as well as systematic and unsystematic array misalignments have shown that in terms of the three analysed parameters (maximum depth, deepest point cross-section and whole thickness map quality parameter), there is a small influence on the thickness reconstructions relative to a no error reference

measurement, only if the whole array is subjected to sensor position errors, due to a small change in the three analysed parameters. The position calibration greatly helps in compensating for sensor position errors and has displayed robustness for position errors on the order of plus or minus half of the A0 wavelength at the operation point.

As a practical recommendation, large systematic and unsystematic position errors for the whole array should be avoided, as they reduce the accuracy of the reconstruction in terms of the maximum reconstructed defect depth, when compared to a reference measurement with no position errors and also exhibit more reconstruction artefacts. However, due to the robustness of the position calibration, there is no need for very strict tolerances on the sensor positions. Since the defect is always detected and located correctly, depending on the importance of accurately quantifying the defect depth and size, the position tolerances can be further relaxed.

3.4 Numerical Studies on Experimental Data

All the experimental datasets captured for the presented studies can be further analysed by applying some numerical manipulations to investigate the influence of a variety of parameters on the thickness reconstructions, relative to a no error reference measurement. These may for example include amplitude and phase variations as well as sensor failures. For simplicity, the studies presented in this section only focus on the 3 mm deep defect pipe with direct access to the defect (no areas of restricted access) and a ring separation distance of 0.602 m. The numerical alterations may also be equally applied to all the measured datasets.

3.4.1 Amplitude and Phase Variations

Changes in the amplitude and phase may be caused by variations in transduction efficiency and other sources such as the measurement electronics. Phase shifts in particular may also be caused by varying thickness of the pipe wall (see Appendix A for actual thickness of the studied pipe here), or slight material anisotropies, both of which may be due to the manufacturing process. These changes are not easy to be accurately represented in experiment and in this study, the influence of variations of amplitude and phase on the thickness reconstructions are investigated and how the position calibration may aid in dealing with

these amplitude and phase changes. The amplitude and phase changes can be represented with a complex number, which is multiplied with the processed experimental dataset.

The experimental dataset of the 3 mm deep defect with a ring separation distance of 0.602 m forms the basis for this study. Since the thickness reconstructions here are all monochromatic reconstructions (evaluation at the centre frequency), every send-receive path is characterised by a complex number, which represents the amplitude and phase for the respective path and all of the send-receive combinations may be collected in a matrix of complex numbers, where the rows represent the senders and the columns represent the receivers. Starting from this complex matrix, amplitude and phase variations are easily introduced by multiplication with another complex number. It needs to be remarked though, that due to the helical path separation algorithm, certain send-receive pairs need to be scaled with the same complex number, as they originate from the same measured amplitude time trace and the influence of any distortion is expected to affect all wave packets within this time trace equally.

The complex scaling factor uses Euler's representation of complex numbers and is a joint distribution of two independent random variables $M(X, Y)$, one for the amplitude X and one for the phase Y, such that $M(X, Y) = X\, e^{iY}$. The amplitude scaling factor X follows a a ln-normal distribution with parameters $\ln\mathcal{N}(0, 0.25)$, with a mean of 1.03 and a variance of 0.69. A ln-normal distribution is selected, as this will avoid negative amplitude for the scaling factor and therefore also avoid possible covariance with the phase factor, as a negative amplitude corresponds to a 180 degree phase shift. The phase factor Y is based on a uniform distribution with parameters $\mathcal{U}(-\pi/8, \pi/8)$ and this phase shift represents a shift in sensor position of approximately ± 5 mm, when calculated via the wave number at the operation point of the guided wave tomography system. The uniform distribution is chosen as it ensures an "axisymmetric" joint distribution for the amplitude and phase scaling factor in the complex plane.

For the computations, five helical orders are extracted with the goal to reduce the computational time per thickness reconstruction, as a total of 100 thickness reconstructions are conducted. The scaling factor for each reconstruction is chosen at random from the joint distribution M and is applied in the data processing just before the position calibration.

From the thickness reconstructions, it is found that the defect is always detected and correctly located for all 100 trials. The performance metrics of maximum depth and quality

Table 3.9: Numerical study on amplitude and phase variations, based on experimental data (3 mm deep defect pipe with a separation distance of 0.602 m), compared to a no error reference measurement. The maximum depth is the maximum reconstructed depth and quality parameter uses the Frobenius norm for the deepest point cross-section (cross-section) and the total thickness map (all pixel). The values are based on 100 trails, listing the mean value and the standard deviation in brackets.

scaled test case	maximum depth	quality parameters	
		cross-section	all pixel
no error	2.6 mm	1.3	5.3
scaled amplitude and phase	2.5 mm (0.13 mm)	1.8 (0.38)	9.6 (0.74)

parameters for both the deepest point cross-section and whole thickness map for all 100 trials are listed in Table 3.9, where they are compared to the no error reference case, for which no scaling is used. The performance metrics for the scaled amplitude and phase case list the mean from 100 trials and the standard deviation in brackets. From Table 3.9 it can be seen that the influence of the scaling on the maximum depth is small in comparison to the no error reference case, as only a decrease in maximum depth of 0.1 m is found (standard deviation of 0.13 mm). This decrease in maximum depth is similar to the arbitrary sensor position study presented earlier, as the position error introduced by the phase factor causes a position error similar to that of the arbitrary sensor position test. The quality parameters increase relative to the no error reference case as more reconstruction artefacts are present, however, the standard deviation remains small (less than unity), implying a stable behaviour for all 100 trials.

The findings from this study suggest that in terms of the three analysed parameters, the influence of the amplitude and phase scaling within the range considered here on the thickness reconstructions is small in comparison to a no error reference case without scaling. This is because of the small change in performance metrics and the small standard deviation. The reason for the small standard deviation may be found in the position calibration, which is able to compensate for most of the phase variations introduced by the scaling. The position calibration achieves the desired effect in compensating for the numerically introduced phase shifts, since the original goal of the position calibration is to account for the misalignment of sensors which is equivalent to a phase shift.

Since robustness is found based on 100 trials for artificially introduced phase shifts, an argument can be made to transfer this finding to the arbitrary sensor position test, where the

analysis is only based on one experimental measurement. The phase shift of this numerical study makes no assumptions on its origin and it can therefore be argued that the phase shift is on the order of the expected phase shift from a sensor position error with a similar magnitude as in the arbitrary sensor position test. By realising this, it is expected that a similar result (small standard deviation) would be obtained if the experiments of the arbitrary sensor position test would be repeated 100 times. Nonetheless, when comparing the quality parameters in Table 3.8 and Table 3.9 with each other, it is found that the quality parameter is generally higher for the study here, which may be due to the additional amplitude scaling.

3.4.2 Increased Limited View Problem

A common issue for practical applications is the failure of one or more sensors in one of the ring arrays and it is important to understand how this influences the thickness reconstruction, as the loss of transduction in a sensor increases the limited view problem by reducing the number of available viewing angles. This is investigated in this section based on three examples.

The numerical studies are conducted on an experimental dataset captured on the 3 mm deep defect pipe with a ring separation distance of 0.602 m. In the various studies presented in this section, a sensor is "deactivated" by replacing the measured amplitude time traces for the send-receive combinations involving the inactive sensor by a series of values sampled from a normal distribution with parameters $\mathcal{N}(0, 0.25 \times 10^{-3})$. This distribution ensures that the amplitude-time traces of the inactive sensor are approximately on the same level as the noise levels from the experiments, as measured for an actually faulty sensor. The inactive sensors are deactivated before the helical path separation step in the data processing, as this represents the situation found in experiment. For the computations of the thickness reconstructions, a total of 5 helical orders are extracted from the data in order to reduce the computational effort. It is important to note that the computation of the thickness reconstruction, if not specified otherwise, assumes that both arrays still contain 24 sensors that are equally spaced along the circumferential direction.

3.4.2.1 Single Sensor Failure

The single sensor failure study assumes that only one sensor is inactive out of the 48 sensors in both arrays, such that less than 4.2% of all send-receive combinations are affected, which is also the case in the single sensor position error study previously presented.

For the analysis, each sensor in the transmitting and receiving array is deactivated in turn and a thickness reconstruction is performed, leading to a total of 48 thickness reconstructions. In all 48 thickness reconstructions, the defect is always detected and correctly located. In Table 3.10, the performance metrics for the single sensor failure study are listed and compared to a reference measurement with all sensors active. The values listed for the single sensor failure correspond to the mean and in brackets the standard deviation of all 48 trials. The comparison of the 48 single sensor failure trials shows that there is only a small variation around the mean value, as indicated by the small standard deviation. When comparing the single sensor failure cases with the reference measurement, it is found that there is no change in the maximum reconstructed depth and only a small change for both quality parameters (0.2 for the deepest point cross-section and 1.1 for the whole thickness map, considering the mean values). This suggests that for the three analysed parameters and in combination with the small standard deviation, the influence of a single sensor failure on the thickness reconstruction, relative to the reference measurement is very small. Based on the findings from the single sensor position error test, this behaviour is expected to be due to the small amount of affected send-receive combinations.

Table 3.10: Numerical study for a single sensor failure, based on experimental data (3 mm deep defect pipe with a separation distance of 0.602 m), compared to a no error reference measurement. The maximum depth is the maximum reconstructed depth and quality parameter uses the Frobenius norm for the deepest point cross-section (cross-section) and the total thickness map (all pixel). The values are based on 48 trials, listing the mean value and the standard deviation in brackets.

test case	maximum depth	quality parameters	
		cross-section	all pixel
no error	2.6 mm	1.3	5.3
single sensor failure	2.6 mm (0.02 mm)	1.5 (0.04)	6.4 (0.2)

3.4.2.2 Gap in Ring Arrays

The ring gap study is of interest to analyse the possibility of using fewer sensors for the data capture, as this means a shorter time for data acquisition. This scenario also occurs if the circumference of the pipe is larger than the array length at a spacing of one wavelength, as in the case of the setup considered here and the array spacing between the sensors is not to be increased.

For the analysis, three consecutive sensors on the sending and receiving array are deactivated, which corresponds to approximately four A0 wavelengths at the operation point. A thickness reconstruction is then performed, assuming that both arrays still contain 24 sensors to ensure equal spacing of sensors along the circumferential direction. Since the location of the defect is usually not known apriori, the study looks at the location of the defect relative to the array gaps. For that purpose all possible permutations for the ring gaps are considered, yielding a total of 576 thickness reconstructions.

From the thickness reconstructions it is found that the defect is always detected and correctly located for all 576 cases. The performance metrics are listed in Table 3.11, where the mean and standard deviation of the ring gap study are listed and compared to a no error reference measurement. When comparing all 576 thickness reconstructions, it is found that all show very good agreement, which is also seen from the low standard deviation of the maximum depth and quality parameters. This also implies that the influence of the location of the defect relative to the array gaps is small, given the small standard deviation. The comparison to the no error reference measurement shows a small increase in the quality

Table 3.11: Numerical study for a gap in both ring arrays, based on experimental data (3 mm deep defect pipe with a separation distance of 0.602 m), compared to a no error reference measurement. The maximum depth is the maximum reconstructed depth and quality parameter uses the Frobenius norm for the deepest point cross-section (cross-section) and the total thickness map (all pixel). The values are based on 576 trials (all possible permutations of 3 consecutive inactive sensors in both arrays), listing the mean value and the standard deviation in brackets.

test case	maximum depth	quality parameters	
		cross-section	all pixel
no error	2.6 mm	1.3	5.3
4 wavelength gap	2.4 mm (0.06 mm)	1.9 (0.22)	7.3 (0.5)

parameters (0.6 for the deepest point cross-section and 2.0 for the whole thickness map, in terms of the mean values) and decrease in maximum reconstructed depth of 0.2 mm, which, in conjunction with the low standard deviation, implies that, in terms of the three analysed parameters, the influence of the gap in the ring arrays on the thickness reconstructions relative to the no error reference measurement is small.

These findings suggest that the inspection of the area of interest for the given pipe could be achieved with an array of 21 by 21 sensors rather than the 24 by 24 sensor arrays used for the experimental measurements presented in the previous sections, which would yield a speed up in data capture, as less send-receive pairs need to be measured (here, data acquisition time would drop from 6.5 h to 5 h approximately). Likewise, for a larger pipe diameter, 24 sensors per array could be used leaving a gap in the the array.

3.4.2.3 Spatial Undersampling

In the previous study it is found that the thickness reconstruction is robust to a gap of three sensors in the ring arrays, which can be exploited to reduce the number of send-receive combinations that need to be captured for the thickness reconstructions. In this study, a further step towards reducing the number of send-receive combinations is taken whereby only 12 sensors per transducer ring are used for the thickness reconstruction. For this, data can be easily constructed from a measured 24 sensor dataset, by considering every second sensor in the array only (either beginning with the odd or even numbered sensor). This then leads to an increase in the circumferential distance between two sensors increases from one A0 wavelength to approximately two A0 wavelength at the operation point.

The deepest point cross-section for the 12 sensor case is illustrated in Figure 3.10, where it is compared to a reference case, which is based on the measured 24 sensor dataset and the nominal thickness variation. From Figure 3.10 it can be seen that for the 12 sensor case, the defect is detected and correctly located. In comparison to the reference measurement, which represents the best achievable result in this study, the 12 sensor case shows good agreement with the reference measurement in the region of the defect in terms of shape and maximum depth, however, exhibits more artefacts away from the defect. This is also seen from Figure 3.11, which shows the thickness map for the 12 sensor case, as a function of the axial and circumferential coordinate. From Figure 3.11 it can clearly be seen that there are

Table 3.12: Numerical study on spatial undersampling, based on experimental data (3 mm deep defect pipe with a separation distance of 0.602 m), compared to a no error reference measurement. The 12 sensor case is based on two 12 sensor arrays. The maximum depth is the maximum reconstructed depth and quality parameter uses the Frobenius norm for the deepest point cross-section (cross-section) and the total thickness map (all pixel).

scaled test case	maximum depth	quality parameters	
		cross-section	all pixel
no error - 24 sensors	2.6 mm	1.3	5.3
12 sensors	2.7 mm	2.3	12.1

more artefacts outside the defect region, when compared to a reference measurement, as for example in Figure A.1(b). The artefacts are however not severe enough (maximum depth similar to the actual defect) to mask the defect.

The performance metrics of the thickness reconstructions for the 12 sensor case and the reference measurement are listed in Table 3.12 and the observations from the thickness map and deepest point cross-section for the 12 sensor case are confirmed. The maximum reconstructed depth matches that of the reference measurement and the quality parameters

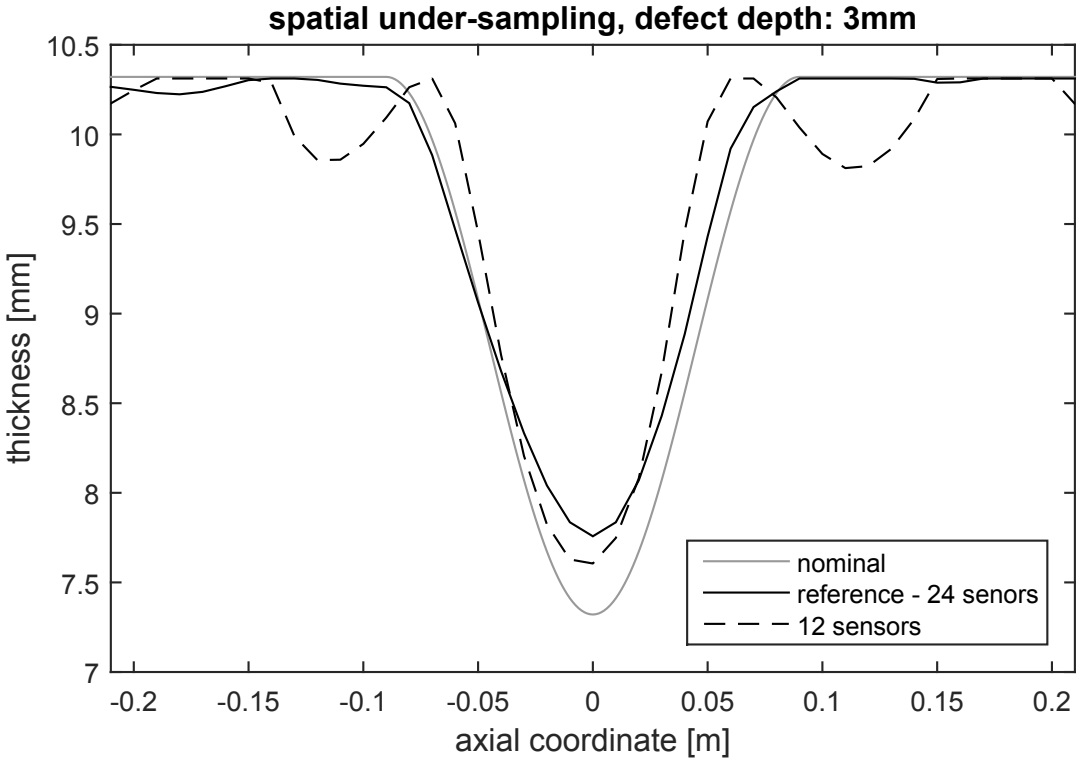

Figure 3.10: Deepest point cross-section for spatial undersampling (12 sensor case), based on experimental data (3 mm deep defect pipe with a separation distance of 0.602 m), compared to a 24 sensor reference measurement and nominal thickness variation.

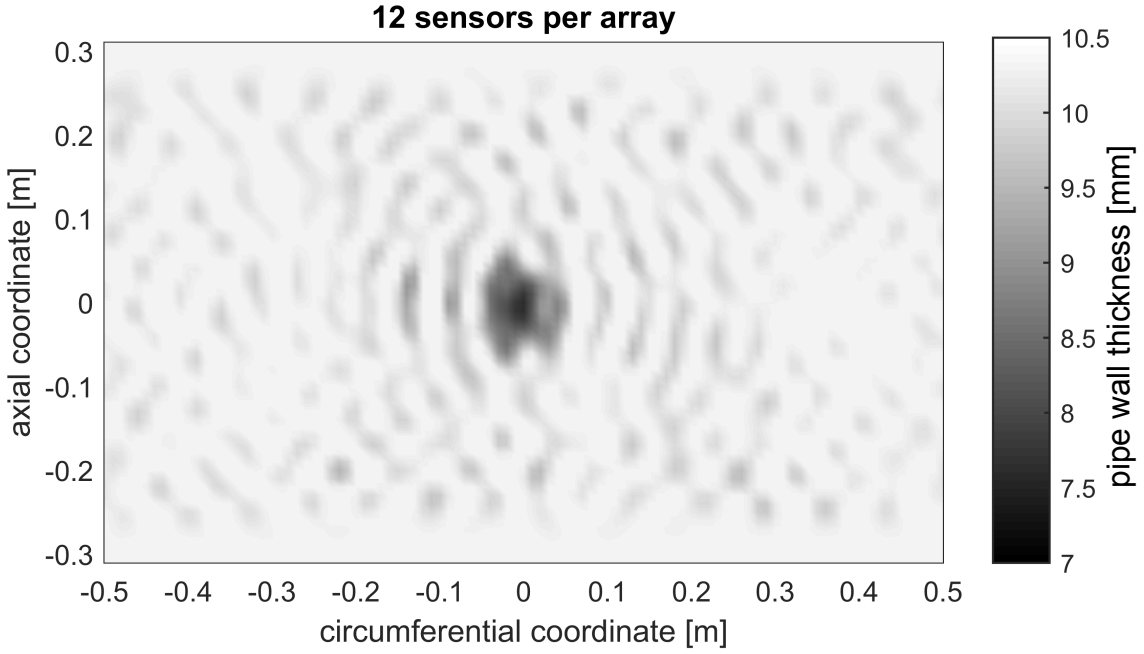

Figure 3.11: Thickness maps for spatial undersampling, based on experimental data (3 mm deep defect pipe with a separation distance of 0.602 m) for the 12 sensor case.

are increased as expected, especially the one for the whole thickness map by 6.8 (1.0 for the deepest point cross-section), which is caused by the presence of reconstruction artefacts.

The findings above suggest that spatial undersampling relative to the reference configuration leads to generally poorer reconstructions, which is obvious, as less data is available for the reconstructions. From these findings it is concluded that the maximum number of equally spaced sensors should be used for the measurements, if maximum accuracy is to be achieved, however, if only detection and location of the defect is desired, fewer sensors per array are necessary. Another test looking at reconstructions using 8 or 6 sensors per array is found to be unsuccessful, as the thickness reconstruction breaks down. As an explanation for this, the loss in resolution due to the extremely low spatial sampling rate (sensor spacing of three wavelength for the 8 sensor case and four wavelength for the 6 sensor case) leads to the background image in the HARBUT algorithm being a poor approximation of the defect, such that the Born approximation may no longer be assumed for the diffraction tomography stage of the HARBUT algorithm.

3.4.2.4 Discussion

In the studies presented for the increased limited view problem, it is always found that if a small number of sensors is inactive, then there is only a small influence on the thickness reconstruction, relative to a no error reference measurement and in terms of the three analysed parameters (maximum depth, deepest point cross-section and whole thickness map quality parameters). This behaviour may be explained with the helical path separation algorithm, which helps to smooth/interpolate missing send-receive combinations. The helical path separation algorithm performs a Fourier transformation along the receiver array, which is then iteratively filtered with a low pass filter with increasing cut-off for each iteration, starting from the lowest component. The data in the gaps of the array (inactive sensors) is therefore interpolated and partially removed by this filtering step, which is clearly seen in the single sensor failure study and the array gap study, due to the small influence onto the thickness reconstructions relative to a no error reference case.

3.5 Enhanced Data Acquisition

The data acquisition for all the previous experimental measurements uses time averaging for data acquisition, whereby the received signal is average 1000 times to reduce the incoherent noise present in the experiment, as discussed in Section 2.3.2. This large number of averages is necessary due to the generally poor signal-to-noise ratio of EMAT transducers and therefore significantly increases the duration for measuring one send-receive combination, which is determined by the sampling rate, number of recorded samples and number of time averages.

One way to enhance the data acquisition speed is to use Golay complementary sequences and in the following the feasibility will be discussed. The findings are then extended to low voltage applications of guided wave tomography, which may be used for hazardous environments.

3.5.1 Golay Complementary Sequences

Cross-correlation based techniques allow for fast data capture in environments with poor signal-to-noise ratio, as in the case of EMAT measurements, in comparison to time averaging. The aim thereby is to use the cross-correlation to identify the "pattern" of the sent signal in the "noisy" received signal. Applications of such techniques are reported in a range of fields such as non-destructive testing [Phang et al., 2008], [Challis and Ivchenko, 2011], [Challis et al., 2013] for fast measurement of phase velocity and attenuation via spectrometry or radar applications [Cook, 1960], [Craig et al., 1962].

The basic idea of cross-correlation based techniques is to transmit a signal and then cross-correlate the received signal with the transmitted signal, in order to for example identify the time-of-flight of the signal, or use the resulting cross-correlation function for further processing. One major drawback of the cross-correlation operation is that correlation noise may distort the signal processing and to overcome this issue, the cross-correlation based techniques chosen here uses Golay complementary sequences [Golay, 1961], for which two complementary pseudo-random sequences are required. The key property of this approach is that the sum of the auto-correlation function (cross-correlation with itself) of each pseudo-random sequence yields a spike (delta-function) at the origin and correlation noise is minimised. Other properties of Golay complementary sequences are presented in [Golay, 1961] and not further discussed here.

Generally, the two complementary sequences pseudo-random sequences consist of an array of binary states, however, for the implementation here, this is adapted. Each sequence element is represented by a five cycle Hann-windowed toneburst and the binary states are implemented via a phase shift of 0 and 180 degrees, such that 0 corresponds to a 0 degree phase shift and 1 to a 180 degree phase shift. For the measurements, in turn, each sequence is transmitted and recorded at the receiver location and then cross-correlated with the transmitted sequence, yielding a cross-correlation function for each sequence. These two received cross-correlation functions are then summed in order to yield the amplitude-time trace for the processing with the tomography algorithm.

One important aspect for Golay complementary sequence data acquisition is the presence of noise, especially in low voltage operation scenarios. This is because of the analogue-to-digital converter at the receiver stage, where the signal level may be smaller than the

quantization step size. This is not an issue for the cross-correlation based technique, as shown in [Challis and Ivchenko, 2011], [Challis et al., 2013]. The total signal, which is the superposition of the noise and measured signal, is spread over the whole dynamic range of the analogue-to-digital converter and therefore allowing the signal to be captured. This process is referred to as dithering and the optimal noise level for Golay complementary sequence data acquisition is studied in [Challis and Ivchenko, 2011], [Challis et al., 2013].

One drawback of this approach is the influence of dispersion on the signal propagation, which may cause the cross-correlation to break down for highly dispersive media. However, it has been verified that this limitation does not apply to the A0 mode with the operation point and range considered in the guided wave tomography system.

For the experiments, Matlab functions for the data capture with the Handyscope HS3 and Golay complementary sequences were readily available to the author, as part of the software resources of the research group [Corcoran, 2015].

3.5.2 Guided Wave Tomography with Golay Complementary Sequences

The Golay complementary sequence data capture approach is used for data capture on the 3 mm deep defect pipe with a ring separation distance of 0.602 m. In order to ensure that a more optimal noise level is used for the data capture, each sent sequence is averaged 5 times before cross-correlation.

The results from the thickness reconstructions are illustrated in Figure 3.12, where the deepest point cross-section is shown, comparing the Golay complementary sequence approach with the time averaging approach and the nominal thickness variation. From Figure 3.12 it can be seen that the curves for both averaging and Golay complementary sequences show very good agreement, implying the feasibility of the data capture approach. In comparison to the nominal thickness variation, the defect is detected and correctly located with the reconstruction error matching that of the time averaging acquisition. Table 3.13 compares both data acquisition approaches and lists the maximum depth, quality parameters and duration to acquire the amplitude-time trace for one send-receive combination. From Table 3.13 it can be seen that additional to the good agreement in terms of the maximum

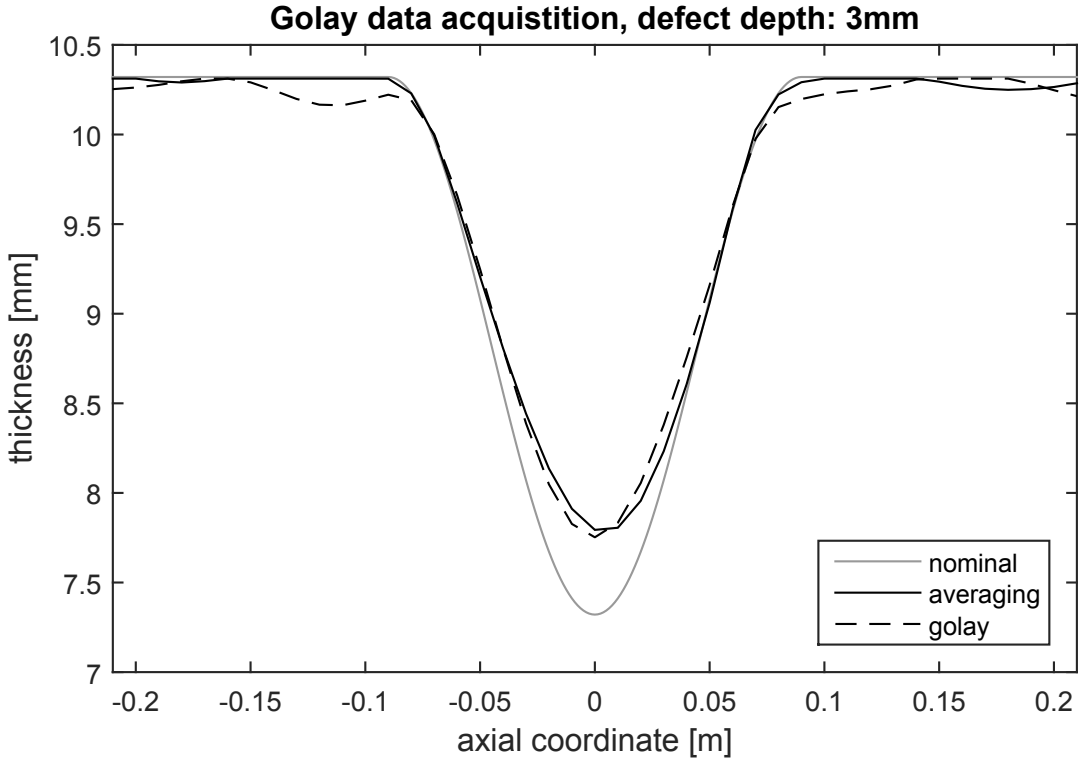

Figure 3.12: Deepest point cross-section for Golay complementary sequences data acquisition measured on the 3 mm deep defect pipe with a separation distance of 0.602 m, compared to the averaging data acquisition measurement and nominal thickness variation.

defect depth, both quality parameters also show good agreement (a difference of 0.1 for the deepest point cross-section and 1.4 for the whole thickness map), implying that both data acquisition approaches yield similar results. The comparison of data acquisition times for one send-receive combination shows however, that the Golay complementary sequence data capture is about six to seven times faster than the time averaging. Given that a total of 576 send receive combinations need to be measured, this means a significant improvement in terms of the data acquisition speed, reducing the data acquisition time for the whole dataset from over 6.5 hours with averaging data capture to about an hour with Golay complementary sequence data capture.

As a remark, in all previous experimental studies, the time averaging data acquisition approach has been selected, as it gives more insight into the signal used for processing and allows for easier debugging. The Golay complementary sequences data capture returns a cross-correlation function, which does not allow for this type of debugging. Nonetheless, it is found that the Golay complementary sequence data acquisition yields the same accuracy as the time averaging data acquisition in a six to seven times shorter time.

Table 3.13: Overview and results for various data acquisition techniques, comparing averaging and Golay complementary sequences data acquisition, measured on the 3 mm deep defect pipe with a separation distance of 0.602 m. The maximum depth is the maximum reconstructed depth and quality parameter uses the Frobenius norm for the deepest point cross-section (cross-section) and the total thickness map (all pixel).

data acquisition	measurement duration a-scan	maximum depth	quality parameters	
			cross-section	all pixel
averaging	40 s	2.5 mm	1.1	4.8
Golay	6 s	2.6 mm	1.2	6.2

3.5.3 Low Voltage Guided Wave Tomography

One motivation for the research presented in [Phang et al., 2008] is the usage of low voltages to drive an ultrasonic spectrometry system in order to operate in hazardous environments that do not allow for high voltages. Since the usage of low voltages in conjunction with time averaging is not feasible due to very long data acquisition times, low voltage Golay complementary sequences data acquisition is successfully demonstrated in [Phang et al., 2008].

In this study, the feasibility for low voltage guided wave tomography is studied, as this may allow for a low power consumption of the data acquisition hardware and therefore making a system design feasible, which may be portable or could be used for structural health monitoring. For that purpose, in the experimental setup illustrated in Figure 2.13, the input amplifier stage is removed. Further, the maximum amplitude of the send signal is set to 10 V and the received sequences are averaged 50 times to achieve a more optimal noise level for the cross-correlation step. The experiment is conducted on the 6 mm deep

Table 3.14: Overview and results low voltage data acquisition, comparing averaging, Golay complementary sequence and low voltage Golay complementary sequence data acquisition, measured on the 6 mm deep defect pipe at various ring separation distances. The maximum depth is the maximum reconstructed depth and quality parameter uses the Frobenius norm for the deepest point cross-section (cross-section) and the total thickness map (all pixel).

data acquisition	ring separation	measurement duration a-scan	maximum depth	quality parameters	
				cross-section	all pixel
averaging	1.162 m	40 s	4.2 mm	3.3	8.4
Golay	0.562 m	6 s	4.1 mm	3.7	7.9
low voltage Golay	0.802 m	25 s	4.1 mm	3.6	8.8

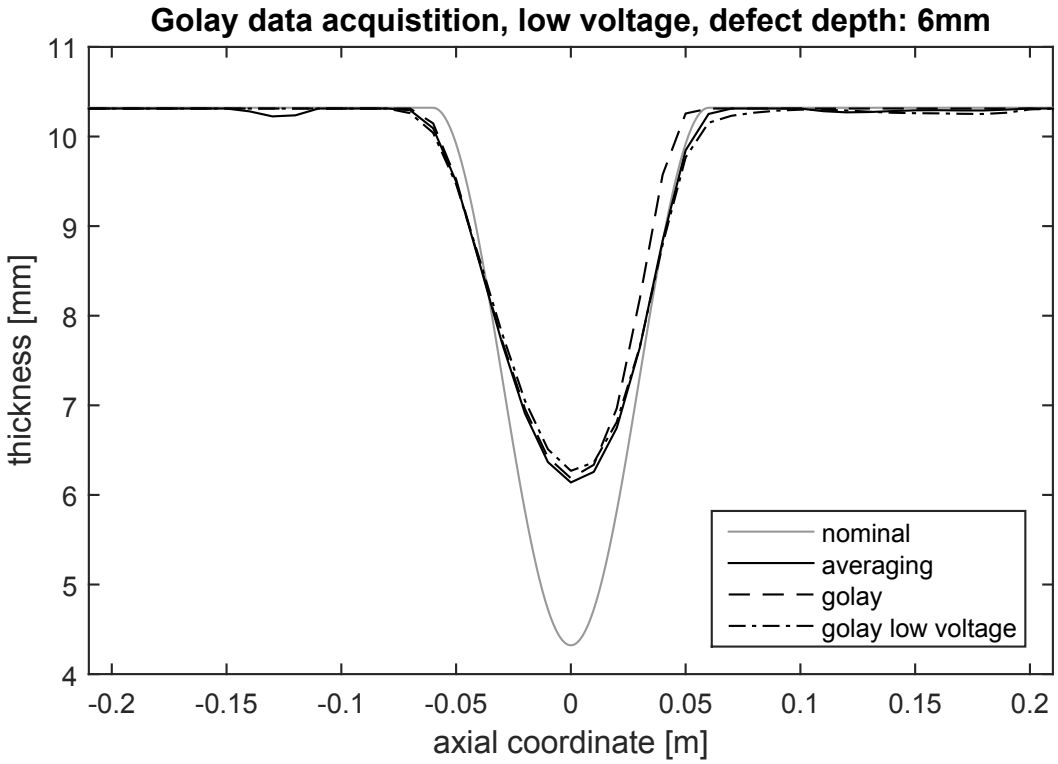

Figure 3.13: Deepest point cross-section for low voltage Golay data acquisition measured on the 6 mm deep defect pipe (ring separation distance 0.802 m), compared to the Golay complementary sequence data acquisition (ring separation distance 0.562 m), averaging data acquisition (ring separation distance 1.162 m) and nominal thickness variation.

defect pipe with a ring separation distance of 0.802 m. The results are then compared to thickness reconstructions from both time averaging and Golay complementary sequence data acquisition, also captured on the 6 mm deep defect pipe, but at different ring separation distances (see Table 3.14).

Figure 3.13 shows the deepest point cross-section for the low voltage Golay complementary sequence test and compares it to the deepest point cross-section of a time averaging and Golay complementary sequence data acquisition with the input amplifier as well as the nominal thickness variation. From Figure 3.13 it can be seen that all three experimental curves line up on top of each other, showing very good agreement. This implies that the same accuracy may be achieved without the input amplifier (operated with low voltages), when compared to both data acquisitions with the input amplifier. In Table 3.14, the three data acquisition techniques are compared regarding their duration to measure one send-receive combination, maximum reconstructed depth and quality parameters. From Table 3.14 it can be seen that the maximum reconstructed depth shows very good agreement for all three data

acquisition techniques (variation of 0.1 mm). Similarly, the quality parameters also show good agreement, with a slightly higher value for the low voltage case. The comparison of the measurement duration for one send-receive combination shows that the data acquisition for the low voltage Golay complementary sequences data acquisition ranks between the two input amplified cases, with the time averaging being the slowest, as found in the previous section.

In conclusion, it is found that the tomography system can be operated with low voltages, when Golay complementary sequences are used and the same accuracy may be achieved as with high voltage operation (input amplifier used), which is also one of the conclusions from [Phang et al., 2008].

Chapter 4

Inspection of Areas with Restricted Access

In the previous chapter, the robustness of the data acquisition process has been investigated within the limits expected to be encountered for the experiments when considering the inspection of areas with restricted access. With the main conclusion being that a sufficiently robust behaviour is found, in this chapter three different inspections problems, considering regions with restricted access are considered and their influence on the thickness reconstructions are discussed, since this represents the main interest of this research project. The three experimental studies of support locations, pipe clamps and STOPAQ(R) coatings also represent the novelty presented in this chapter.

4.1 Support Locations

Support locations are areas with restricted access that may have various designs and the ones considered here are typical examples of the petrochemical industry. They consist of a concrete block, on top of which an h-beam or rod is placed, that is in contact with the pipe. At support locations, corrosion mainly occurs at the metal-to-metal contact interface between the support location and pipe material, as both materials exhibit different chemical

compositions and therefore upon contact may form a galvanic cell. In this section, the influence of a support location on the guided wave tomography thickness reconstruction is studied. The experimental studies consider the 3 mm deep defect listed in Table 3.1 and two types of supports, an h-beam and a rod support, which are widely used in the oil and gas industry.

4.1.1 Overview

In order to study the influence of a support location on thickness reconstructions with guided wave tomography, a life-sized representation of the support location on a laboratory scale needs to be considered. The support locations are realised in the laboratory by using a material testing machine (Instron 8800 series servo-hydraulic testing machine, High Wycombe, Buckinghamshire, United Kingdom), whereby a three-point bending setup is chosen with the punch representing the support location (h-beam or rod). The experimental setup is illustrated in Figure 4.1, where in (a) the pipe is shown resting in the material testing

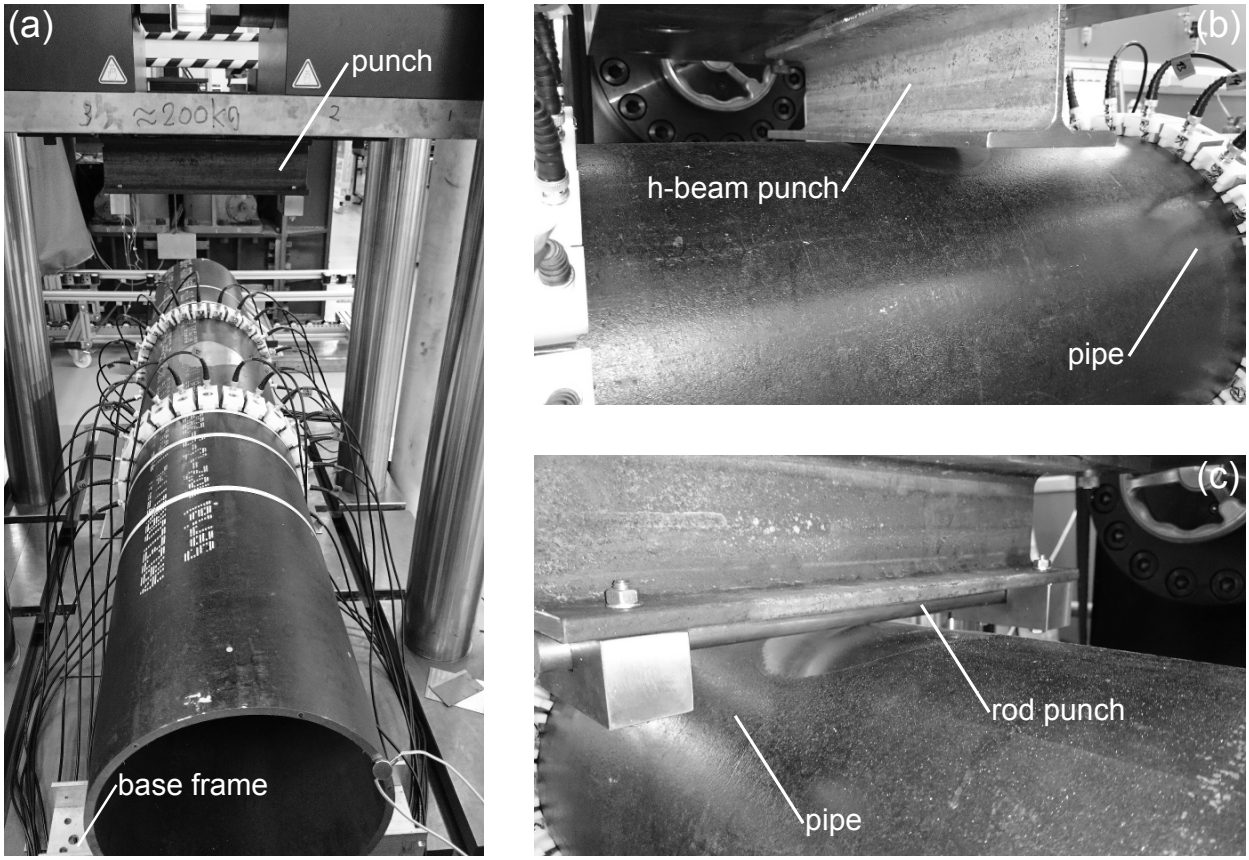

Figure 4.1: Experimental setup for the support location measurements (a) and the two punches (support locations) used in the experiments, h-beam in (b) and rod in (c).

Table 4.1: Overview of all conducted support location experiments on the pipe with the 3 mm deep defect and 0.602 m ring separation distance, considering two types of supports (h-beam and rod), as well as various contact forces and contact locations. The maximum depth is the maximum reconstructed depth and quality parameter uses the Frobenius norm for the deepest point cross-section (cross-section) and the total thickness map (all pixel).

support type	contact location	contact force	maximum depth	quality parameters	
				cross-section	all pixel
reference	none	-	2.5 mm	1.2	5.1
h-beam	on defect	5 kN	2.5 mm	1.4	5.3
h-beam	on defect	10 kN	2.5 mm	1.4	5.5
h-beam	on defect	20 kN	2.5 mm	1.5	5.6
rod	on defect	10 kN	2.5 mm	1.9	5.9
rod	on defect	20 kN	2.5 mm	2.0	6.0
rod	axial shift	20 kN	2.6 mm	1.2	5.2
rod	circumferential shift	20 kN	2.6 mm	1.2	5.0

machine. The upper half in Figure 4.1(a) shows the punch and the movable parts of the material testing machine and the pipe is placed on a base frame to secure it in place for the loading process, as well as counter the force exerted by the punch. The base frame is designed such that the counter points for the force are as far away from the sensor rings and defect as possible, to avoid interference with the measurement and a simplified safety calculation has been performed in order to establish safe operation. In Figure 4.1(b) and (c), the h-beam and rod punches/support types are shown as they are in contact with the defect. The main difference between these two support types is the type of contact. While the rod support exhibits a single point contact, the h-beam features a line contact, which when pressed onto the defect degenerates to two short line contacts. This is due to the axial defect profile with the deepest point of the artificial defect located in-between the two line contacts, which is also observed during the experiments. The magnitude of the contact force is also a parameter of study for the support location experiments and can be understood as a way of representing the distance between two support locations.

In Table 4.1 all the combinations of support type, contact location and loading force are listed in the first three columns, as well as the results from the thickness reconstructions in the later three. All experiments are conducted with a ring separation distance of 0.602 m and the sensor positions of the transducers in each array are identical for all the experiments. In the first two studies, each support type is pressed against the defect and the influence of the contact force is analysed, ranging from 5 kN to 20 kN, which corresponds to the weight

of 5 m to 20 m of the empty pipe (weighs 100 kg/m) considered here. A third study looks at the influence of a shifted contact point, both in the axial and circumferential directions for the rod support with a constant contact force. A reference measurement without a support location is also conducted to allow for a better understanding of the influence of the support locations on the thickness reconstructions. In the following, the results for the various studies are presented and discussed.

4.1.2 H-beam Support Pressed onto Defect

The first study considers the h-beam support where the defect is located in the contact zone and the contact force is varied between 5 kN, 10 kN and 20 kN. The deepest point cross-section for the thickness reconstructions is displayed in Figure 4.2, comparing the loaded cases with the no load case and nominal thickness variation. From Figure 4.2 it can be seen that the deepest point cross-sections for all experiments, loaded cases and no load case, line up on top of each other. Also, for the three parameters listed in Table 4.1, the

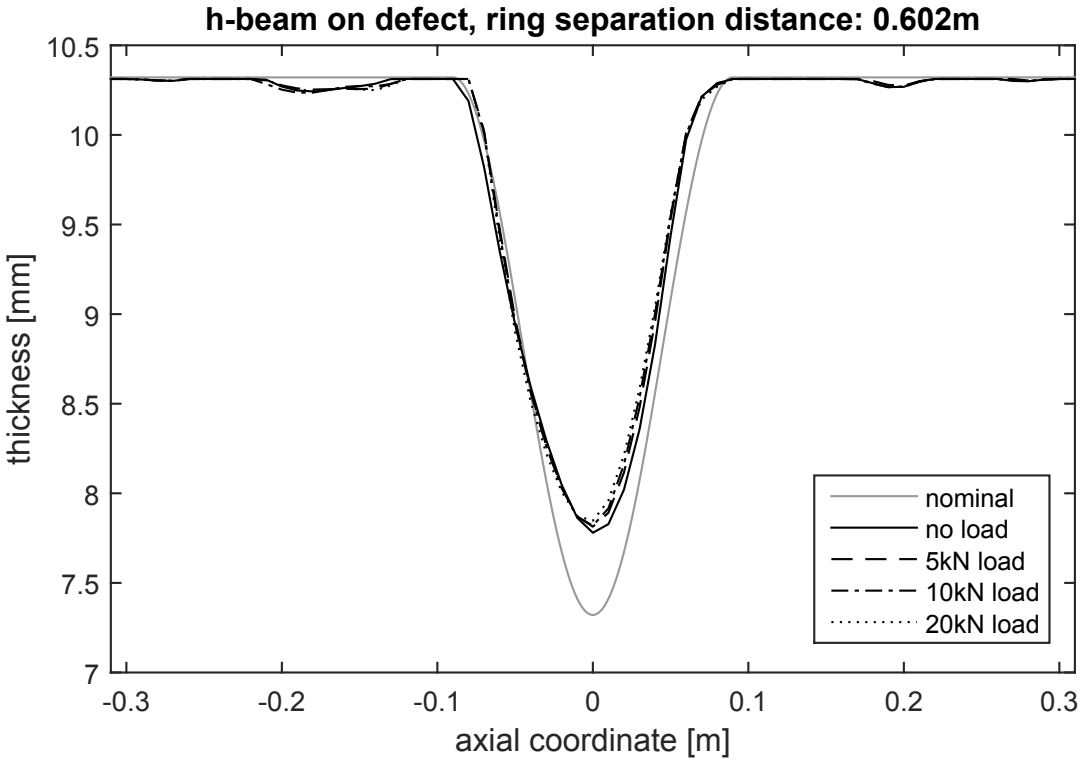

Figure 4.2: Deepest point cross-section for the h-beam support pressed onto the 3 mm deep defect, comparing experimental reconstructions for the loaded cases with the no load case and the nominal thickness variation. The ring separation distance is 0.602 m and no significant influence of the h-beam support on the thickness reconstructions is observed.

maximum depth does not change and only an increase of the deepest point cross-section quality parameter of up to 0.3 (0.5 for the whole thickness map) is observed, implying a good match between the loaded and no load cases. When comparing the experimental reconstructions to the nominal thickness variation, it is found that the defect is detected and correctly located. Further, when comparing the shape of the thickness reconstructions with the nominal thickness variation, good agreement is found in terms of the lateral defect extent near the surface between the reconstruction and the nominal thickness variation up to a depth of approximately 1.4 mm.

Since the various experimental curves for both the loaded cases as well as the no load case all line up on top of each other and the variation in the three analysed parameter is small (for values see Table 4.1), two conclusions can be drawn. Firstly, the magnitude of the loading force shows no significant influence on the thickness reconstructions, when comparing the various loaded cases among each other. Secondly, for the h-beam support type only a negligible influence on the thickness reconstruction in terms of the three analysed parameters is observed, based on the comparison with the unloaded case. The error in reconstruction depth relative to the nominal defect depth is found to be approximately 17% for all loaded cases and no load case. One explanation for this can be found by arguing that the contact conditions between the h-beam and the pipe are not sufficient to distort the wave propagating in the pipe wall, because the localised pressure of the support onto the pipe is not sufficient to serve as a localised thickness variation.

4.1.3 Rod Support Pressed onto Defect

The second study looks at a second support type, the rod support, and based on the findings for the h-beam case, the 5 kN load is omitted, as no significant influence is observed for the h-beam case in terms of the three analysed parameters, relative to a no load case. The deepest point cross-section is depicted in Figure 4.3, where the experimental reconstructions are compared to a no load reference measurement and the nominal thickness variation. From Figure 4.3 it can be seen that for the various loaded cases, the defect is detected and correctly located, as well as the same maximum defect depth and shape of the reconstructed thickness are obtained for both loads. In comparison to the nominal thickness variation, however, a slight deformation of the deepest point cross-section is found in the region where the rod is

in contact with the pipe, such that an increase in thickness is observed there. Figure 4.4 shows the corresponding reconstructed thickness map to the 20 kN load case and it can be clearly seen that the deepest point is shifted slightly off the centre of the defect in positive axial direction, when comparing with Figure 3.2(a). Apart from that, no further increase in the artefacts is registered. Since this deformation of the deepest point cross-section is not found for the no load reference case, the effect can be attributed to the presence of the rod support.

One possible explanation for this is that due to the sufficient contact pressure and therefore sufficient elastic coupling between the pipe and support, a localised thickness increase is observed. Also, the observation of minor plastic deformation at the contact point could confirm this hypothesis. In contrast to that, in the h-beam case, no plastic deformation is observed, as well as no localised thickness increase relative to the reference measurement is found in the deepest point cross-section. This suggests that with higher contact pressure, such as for the rod support, the coupling is improved and therefore a localised thickness

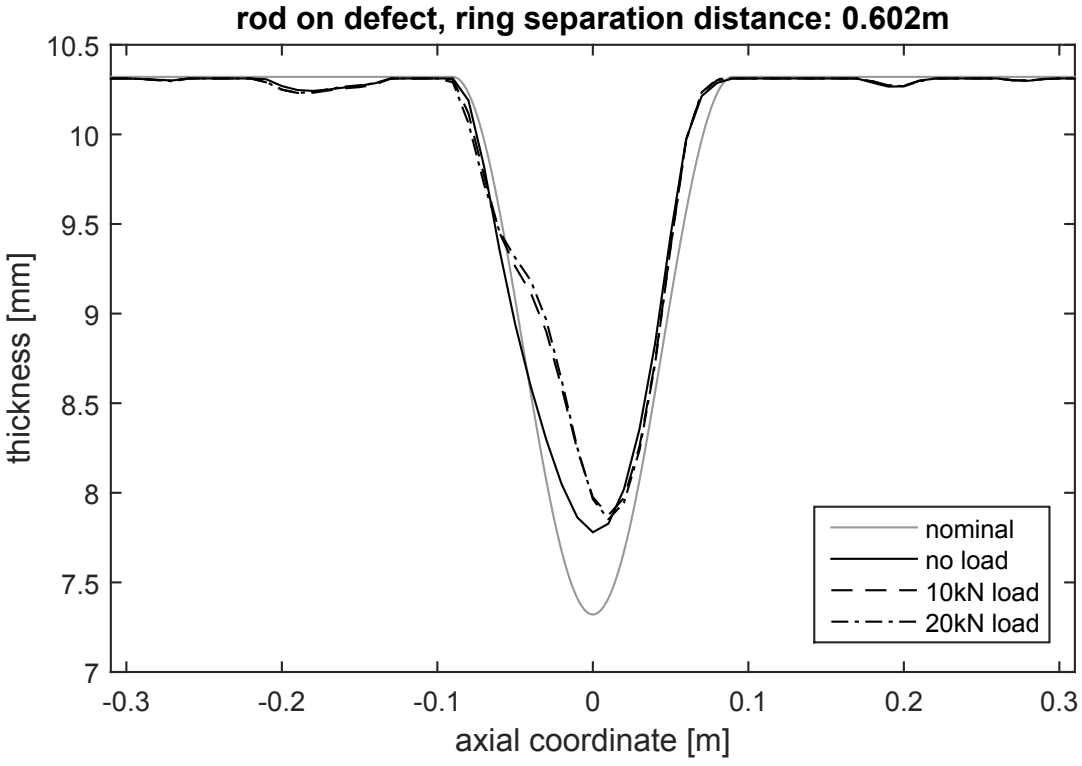

Figure 4.3: Deepest point cross-section for the rod support pressed onto the 3 mm deep defect, comparing experimental reconstructions for the loaded cases with the no load case and the nominal thickness variation. The ring separation distance is 0.602 m and only a small influence of the rod support on the thickness reconstructions is observed.

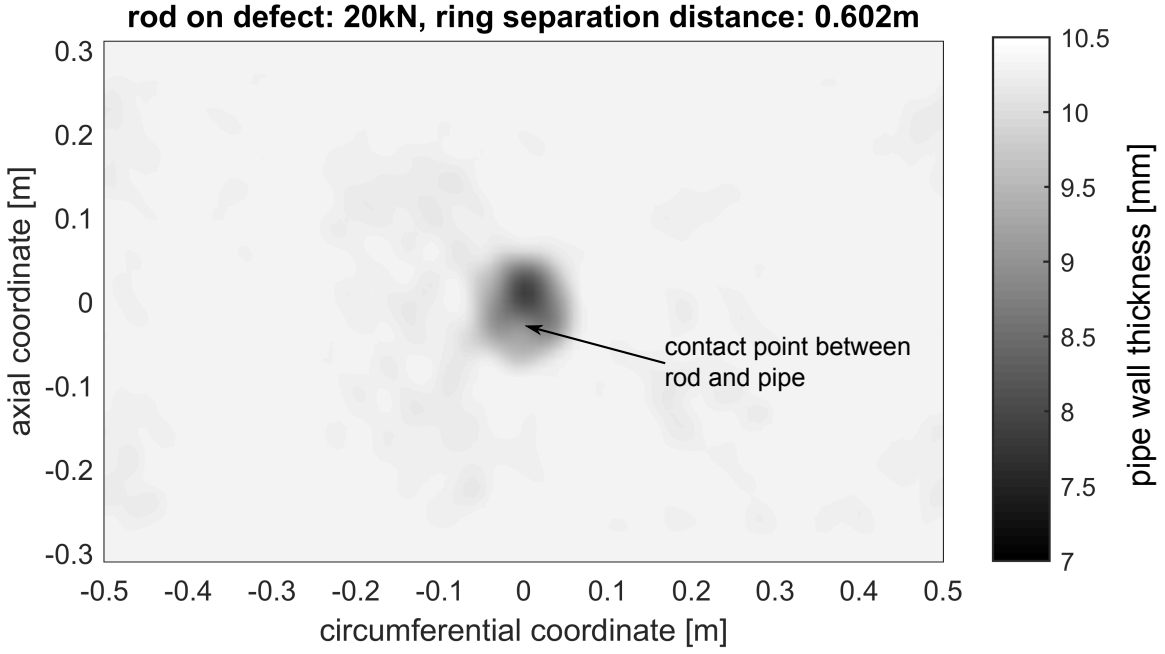

Figure 4.4: Thickness map for the rod support pressed onto the 3 mm deep defect with 20 kN. The ring separation distance is 0.602 m and the contact point between the rod and the pipe is marked. Only a small influence of the rod support on the thickness reconstruction is observed, whereby the maximum depth is shifted slightly in positive axial direction in accordance with Figure 4.3 and in contrast to Figure 3.2(a).

increase may be measured. The maximum depth of the defect is found to be identical with the no load case, when rounding to the tenth of a millimetre (Figure 4.3 shows a slight difference in maximum depth) such that the reconstruction error is 17% relative to the nominal defect depth. Similar to the h-beam case, no influence of the magnitude of the loading force is found on the thickness reconstruction. The comparison of the quality parameter (see Table 4.1) for the deepest point cross-section and the thickness map with the h-beam case shows that there is only a slight increase of 0.5 for the deepest point cross-section quality parameter (0.3 for the whole thickness map) relative to the loaded h-beam case.

4.1.4 Rod Support Pressed Next to Defect

The third case considered is the case where the rod support is pressed against the pipe with the contact point of rod and pipe not coinciding with the defect. This study aims to emulate

the condition under which there is a corrosion patch not at a support location, but near it. The contact point is shifted axially and circumferentially (two separate cases) relative to the defect, as illustrated in the inset of Figure 4.5. In Figure 4.5, the deepest point cross-section for an axially and circumferentially shifted contact point loaded with 20 kN is displayed and compared to the no load case and the nominal thickness variation. The support type is chosen to be the rod support, as in combination with the load, the maximum influence would be expected. From Figure 4.5 it can be seen that all the experimental curves line up on top of each other, showing very good agreement. When comparing the shape of the thickness reconstructions with the nominal thickness variation, good agreement is found in terms of the lateral defect extent near the surface between the reconstruction and the nominal thickness variation up to a depth of approximately 1.4 mm. Also, almost the same quality parameters are found for all the experiments and the typical error in the maximum depth of 17% is observed, similar to the previous support location studies. The comparison of the loaded cases with the no load case shows that there is no significant influence when shifting the loading point, as seen from comparing the maximum defect depth (variation of 0.1 mm) and quality parameters in Table 4.1, which take the same values as the no load reference measurement. This might be unexpected, as in the previous study, an influence has been found for the rod support when pressed onto the defect with the same loading force.

An explanation for this may be found when considering the implementation of the reconstruction algorithm, which uses a regularisation for the VISCIT step, for approximating the missing viewing angles. Since the localised thickness increase due to the contact point is very small relative to the nominal pipe wall thickness, as seen in the previous study, and the contact point is also very small compared to the A0 wave length as well as resolution limit, in the regularisation step of VISCIT, this localised thickness increase falls below the lowest regularisation threshold and is thus set to the nominal thickness. Nonetheless, plastic deformations are observed at the contact locations, similar to those of the previous study, where the rod is pressed against the defect on the pipe. For the case where the contact point coincides with the defect, the presence of the defect helps in preserving the localised thickness increase at the contact point with the rod during the thickness reconstruction. This is because the superposition of the defect and localised thickness increase due to the support lie above the regularisation threshold of VISCIT and are therefore not set to the

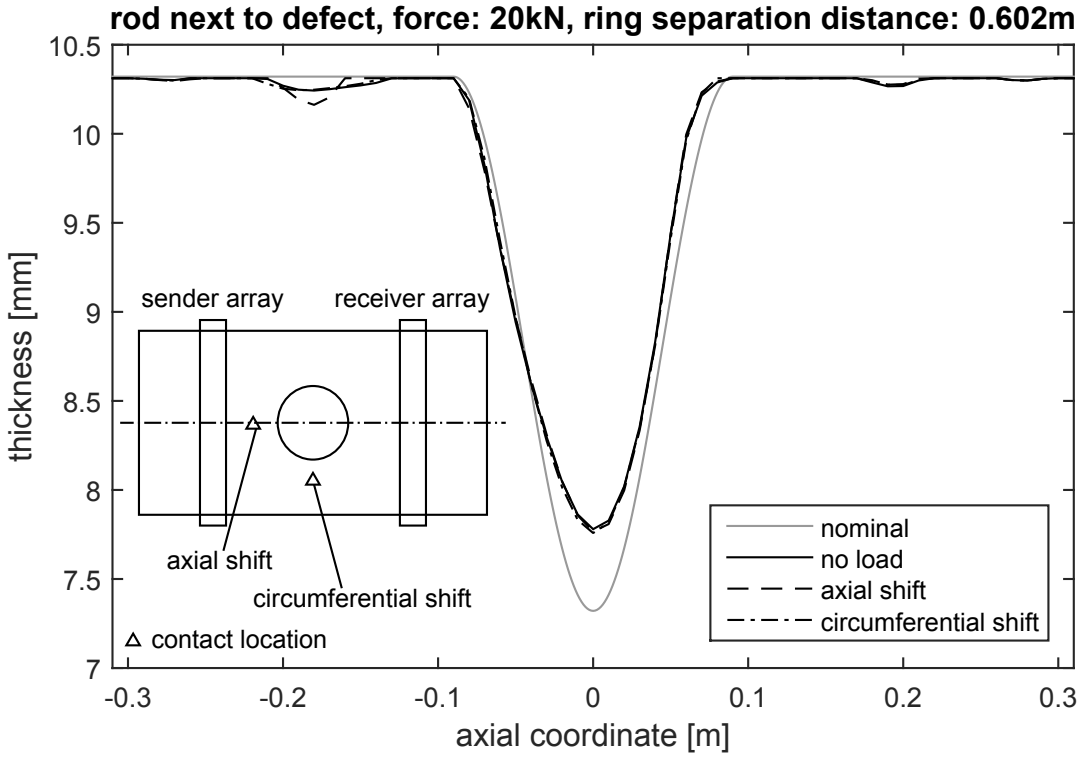

Figure 4.5: Deepest point cross-section for the rod support pressed next to the 3 mm deep defect, comparing experimental reconstructions for the loaded cases with 20 kN and an axial, as well as a circumferential shift in contact point with the no load case and the nominal thickness variation. The ring separation distance is 0.602 m and the inset shows the contact locations between the rod support and pipe. The reconstruction artefact at an axial coordinate of approximately -0.18 m does not correspond to the axial contact point of the rod punch, whose contact point is at approximately -0.12 m.

nominal thickness. This finding is beneficial from a practical point of view, as the thickness reconstruction is not sensitive to a support location when the contact point does not coincide with the defect, or if there is no defect at all.

4.1.5 Summary

As a conclusion from all the three conducted studies, it is found that the influence of a support location on the thickness reconstructions is small in terms of the three analysed parameters, relative to a reference measurement and can be assumed to be negligible for practical purposes. The maximum depth is shown to be independent of the load, the type of support and contact location, whereas the quality parameters for both the thickness map and deepest point cross-section exhibit a slight increase (of up to 0.9) relative to the no

load case for a contact point in the defect region. When comparing the two support types, h-beam and rod, with the contact point coinciding with the defect, in the case of the rod support type, the influence is more pronounced than for the h-beam support, as seen from the quality parameters for the rod support type, which is about 0.4 higher than the quality parameters of the h-beam support. This is due to the higher contact pressure and therefore sufficient coupling to act as a localised thickness increase. In the study, where the contact point of the rod support does not coincide with the defect, no influence on the quality parameters is found relative to the no load reference measurement, which may be explained with the regularisation of the VISCIT algorithm. Similar results as for the 3 mm deep defect are also expected when considering the 6 mm deep defect.

There are two main limitations of the support location experiment that is conducted here, the influence of corrosion products and the consideration of an empty pipe. The presence of corrosion products is expected to further increase the coupling, especially for the lower contact pressure cases, however it is not considered here, due to the vast uncertainty in the coupling conditions that may be present and are barely reproducible for laboratory experiments. To study the influence of corrosion products on the thickness reconstructions, a field trial would be necessary and is proposed for a future investigation.

Since the support location experiment is conducted on an empty pipe, for future studies, fluid filling can be considered and is recommended, as this would enable to understand if a fluid filling represents a limitation for the guided wave tomography system developed here. It needs to be noted that with a fluid filling, changes to the wave propagation paths and dispersion curves are to be expected. With a fluid filling, a wave path through the fluid becomes possible, which may complicate the signal processing of the measured data. Further, new dispersion curves might need to be assumed for the mapping between velocity and thickness, as the boundary conditions are different to those of an empty pipe.

4.2 Pipe Clamp

Pipe clamps are, for example, used in offshore oil extraction to hold the riser pipe in place and corrosion may form in the space between the clamp and the pipe. For the inspection of such features, it is desired that the clamp is not removed and this therefore represents an

area of restricted access. The aim of this study is to investigate the influence of such a pipe clamp on the thickness reconstruction and determine possible limitations.

4.2.1 Overview

The experimental setup for the clamp experiment is depicted in Figure 4.6(a), where a clamp is placed between the two ring arrays. The clamp is provided by project partners (Petrobras) and consists of two halves that are joined together by bolts. In order to avoid metal to metal contact and subsequently contact corrosion, a neoprene mat is placed between the pipe and the two halves of the clamp, which is common practice in the oil industry. This is illustrated in Figure 4.6(b), where a zoomed in view of the clamp is shown. From Figure 4.6(b) it can be seen that the neoprene mat extends beyond the length of the clamp and does not cover the whole circumference of the pipe, but features an air gap. The clamping force is exerted by the tension in the bolts and required to be more than half the yield strength of the bolt material, as specified by Petrobras, and the respective fastening torque has been determined and applied for the experiments. The ring separation distance between both arrays is selected to be 1.162 m, allowing for the neoprene mat and clamp to be placed between the two ring arrays.

Since the two halves of the clamp are joined together by bolts, the pressure exerted onto the neoprene mat by the clamp is not uniform over the circumference of the pipe, but rather features zones of high and low pressure, which are perpendicular to each other. In Figure 4.7(a-d), which shows the axial cross-section through the deepest point of the defect of the experimental setup in Figure 4.6(a), the high pressures zones are indicated by the large grey arrows. The experimental setup is symmetric along the axial direction, such that the defect and the clamp are aligned symmetrically between the two EMAT ring arrays. With the clamp experiments, the influence of the presence of the clamp on the thickness reconstructions is studied as a function of the location of the defect and the location of the air gap, relative to the pressure zones and considering both defects (see Table 3.1).

For that purpose, the location of the air gap and defect relative to the (high) pressure zone are classified into cases, which are illustrated in Figure 4.7(a-c), where the air gap in the neoprene mat is in the low pressure zone and in Figure 4.7(d), where the neoprene mat is rotated by 90 degrees and the air gap is in the high pressure zone. In Figure 4.7(a), “case

A" corresponds to the case where both the air gap and the defect are in the low pressure zone, in Figure 4.7(b) "case B" to where the defect is in the low pressure zone but under

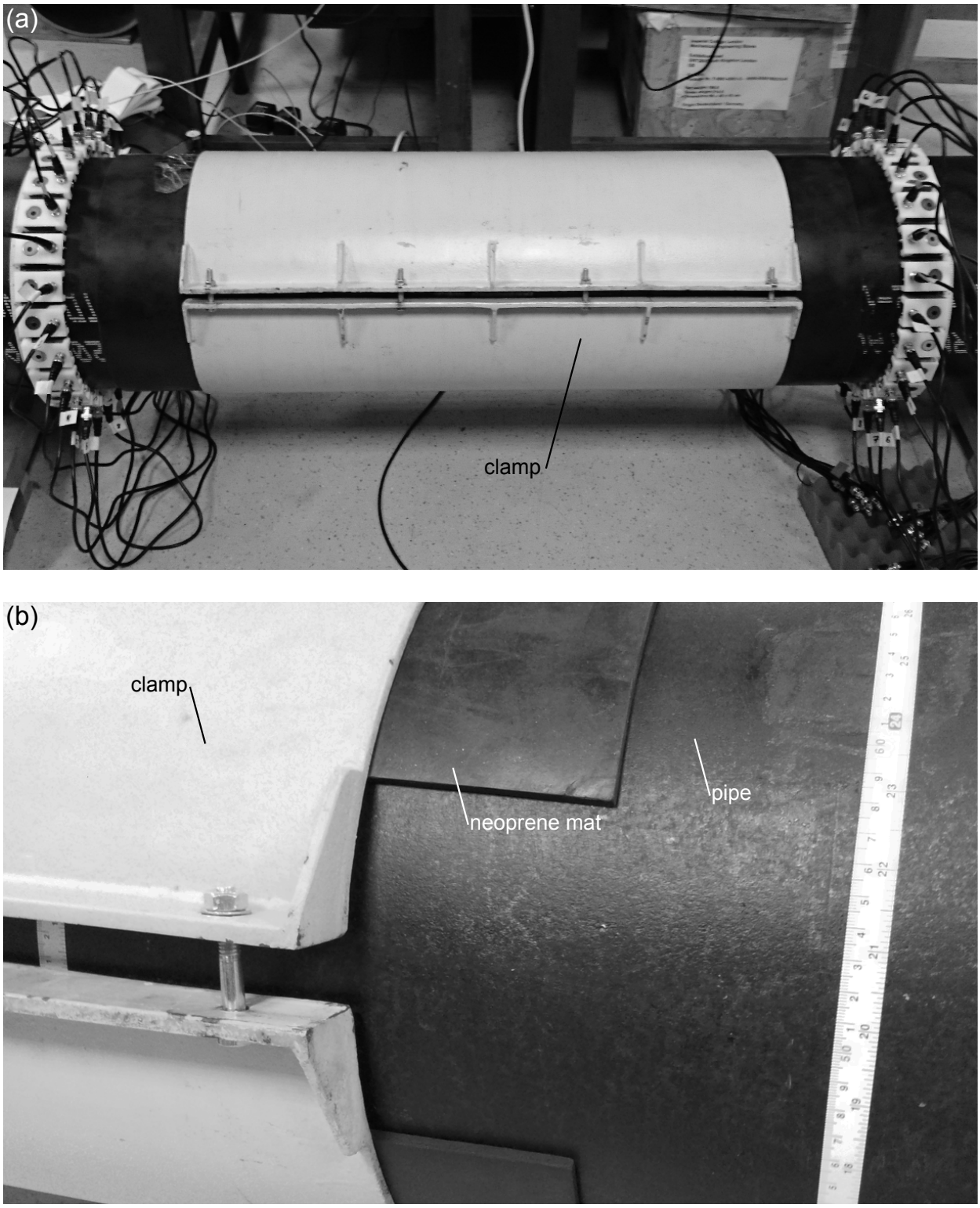

Figure 4.6: Experimental setup for the clamp measurements (a) with a ring separation distance of 1.162 m. In (b), zoomed in view on the air gap, which is located in the low pressure region, where both halves of the clamp are joined by bolts.

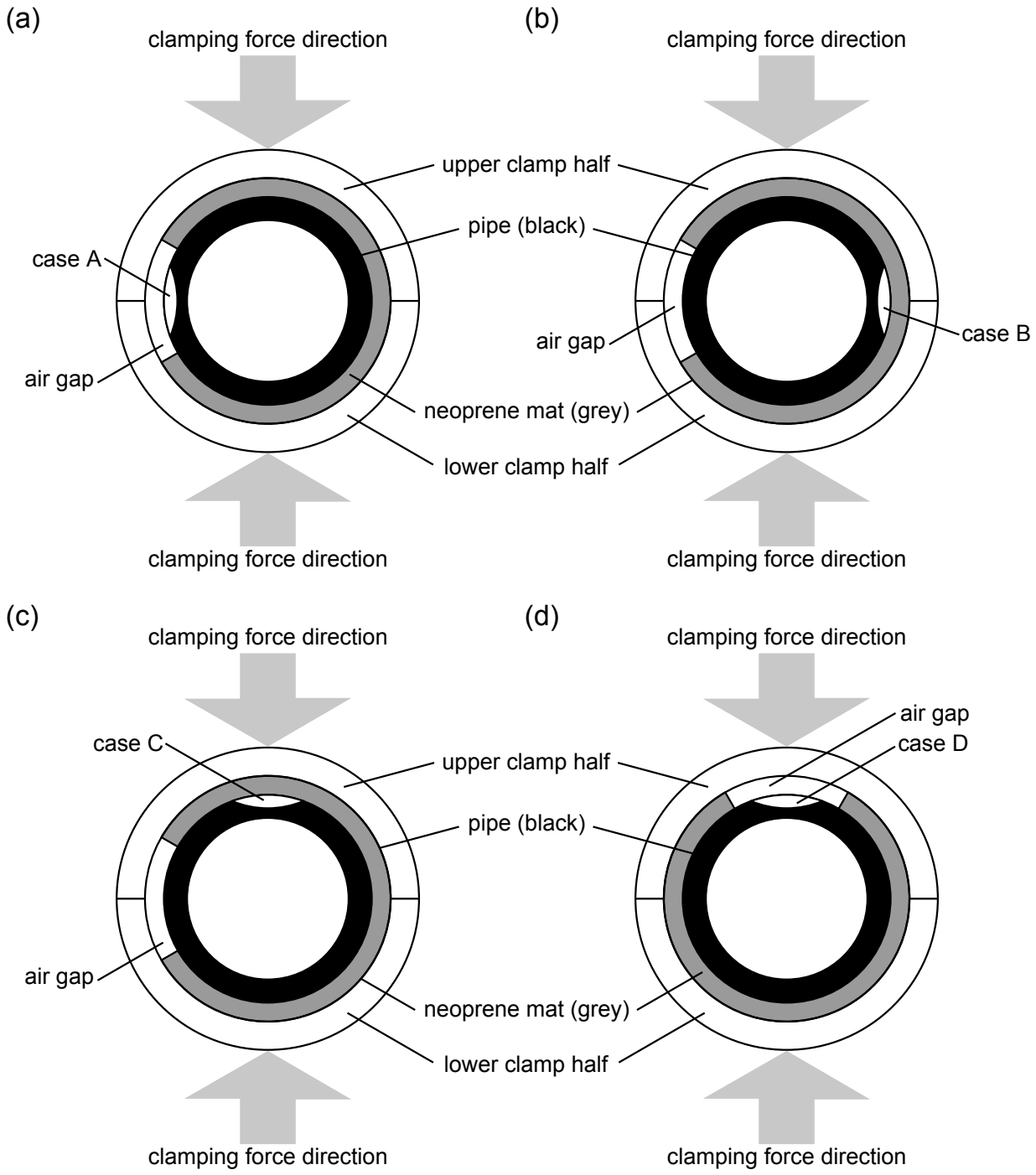

Figure 4.7: Cases considered for the clamp measurements with the air gap in the neoprene mat in the low pressure zone in (a-c) and the air gap in the high pressure zone in (d).

the neoprene mat (air gap in other low pressure zone) and in Figure 4.7(c) "case C" where the defect is in the high pressure zone under the neoprene mat (air gap low pressure zone). In Figure 4.7(d), "case D" is defined as both the air gap and the defect being in the high pressure zone. In Table 4.2, all the considered cases for each defect are listed in the second

column and for each measurement with the clamp a respective reference measurement in the absence of the clamp is performed for comparison, with identical sensor positions to the case with the clamp for better comparison.

4.2.2 Results and Discussion

The first observation, when comparing the measurements with the clamp to the respective reference measurements, is the attenuation of the raw signals for all send-receive combinations. The attenuation is expected, as the A0 mode exhibits mostly out-of-plane displacements for the given operation point (see Figure 2.1(a)) and by pressing a neoprene mat via a clamp against the pipe, the out-of-plane displacement is significantly attenuated. The attenuation can easily be quantified by comparing the measurements with the clamp to the reference measurements and therefore isolating the attenuation due to the clamp, even in the presence of the defect. The attenuation is estimated here for the direct path send-receive combinations only, as both the zeroth and first order helical path can be separated in time and therefore allow for time gating of the zeroth order helical path. By considering all clamp cases from Table 4.2, the attenuation is estimated based on at least 144 measurements and a statistical analysis has shown that the mean attenuation of all observed cases is found to be approximately 11 dB/m (standard deviation of 0.95 dB/m) at the operation frequency of 50 kHz.

The deepest point cross-sections for the various cases of the clamp measurements, listed in

Table 4.2: Overview of all conducted experiments pipe clamp experiments with 1.162 m ring separation distance for the various cases of defect and air gap relative to the pressure zone in Figure 4.7. The maximum depth is the maximum reconstructed depth and quality parameter uses the Frobenius norm for the deepest point cross-section (cross-section) and the total thickness map (all pixel). The values in brackets correspond to the various reference measurements, where the position of the arrays is identical to the case with the clamp.

		maximum	quality parameters (ref.)	
defect depth	clamp case	depth (ref.)	cross-section	all pixel
3 mm defect	case A	2.0 mm (2.4 mm)	2.9 (1.9)	11.6 (7.5)
3 mm defect	case B	2.2 mm (2.4 mm)	2.9 (2.0)	9.4 (7.7)
3 mm defect	case C	1.9 mm (2.4 mm)	3.0 (1.9)	10.7 (7.6)
6 mm defect	case A	3.2 mm (3.8 mm)	5.4 (4.0)	12.9 (9.7)
6 mm defect	case B	3.2 mm (3.9 mm)	5.4 (3.9)	12.4 (9.7)
6 mm defect	case D	3.5 mm (3.9 mm)	4.8 (3.9)	12.0 (9.5)

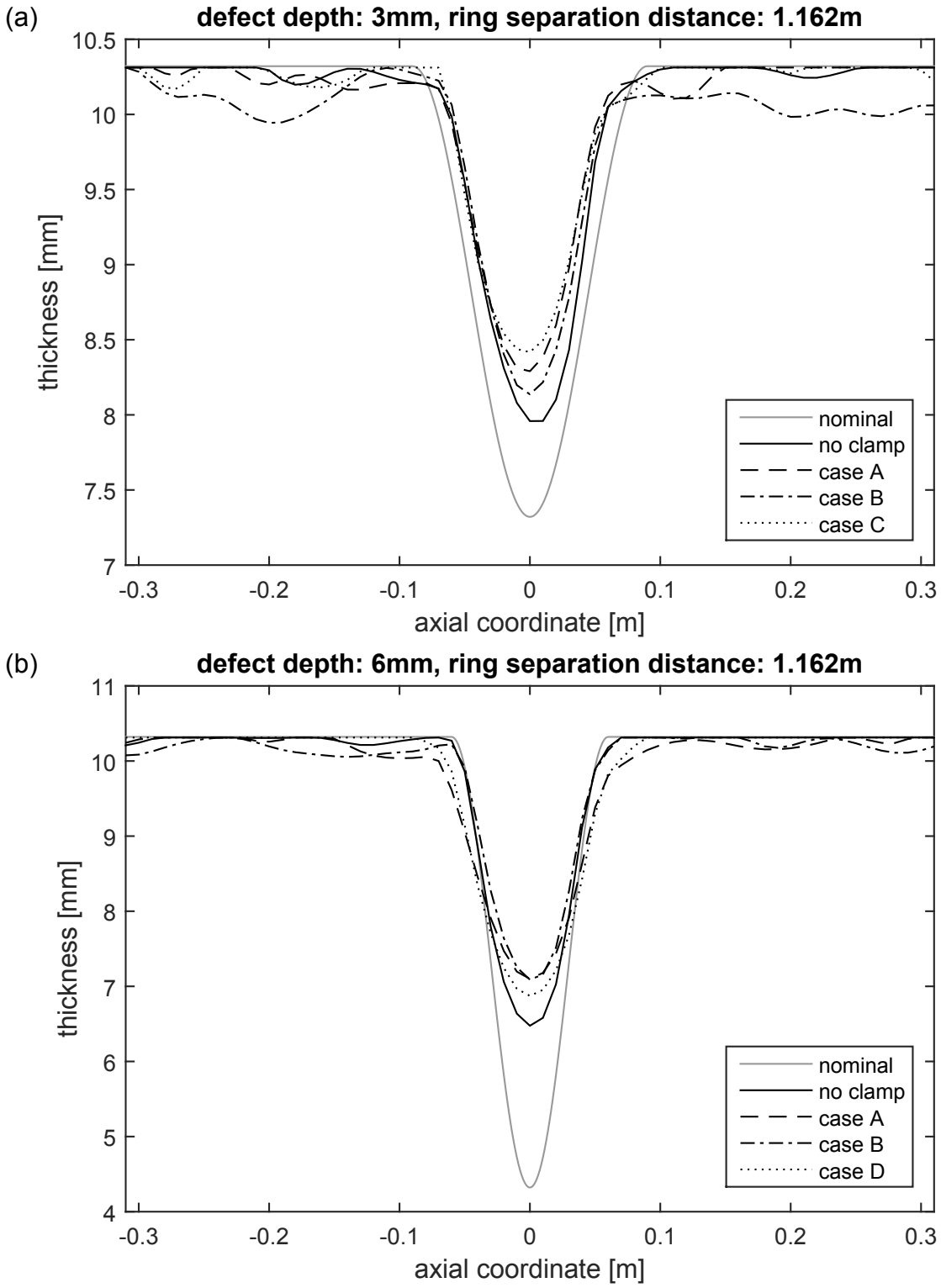

Figure 4.8: Deepest point cross-section for clamp experiments, listed in Table 4.2, in (a) for the 3 mm deep defect and in (b) for the 6 mm deep defect, compared to the reconstructions in the absence of the clamp and the nominal thickness profile. The ring separation distance is selected to be 1.162 m.

Table 4.2, are depicted in Figure 4.8, for the 3 mm deep defect in (a) and in (b) for the 6 mm deep defect. The first thing to note when comparing the reconstructions of the clamp cases for both defects is that the defect is detected correctly located and the shape as well as the depth of the defect are very similar for all clamp measurements. This implies that there is no significant influence of the location of the defect (and air gap) relative to the high pressure zone on the thickness reconstruction. This is of practical advantage, as there is no necessity to specifically account for the pressure zone, when inspecting a clamp location. When comparing the clamp cases for both defects with the nominal thickness variations, good agreement is found in terms of the lateral defect extent near the surface between the reconstruction and the nominal thickness variation up to a depth of approximately 1.3 mm for the 3 m deep defect and approximately 2.3 mm for the 6 m deep defect, however, the maximum depth is underestimated, similar to the previous studies. The error relative to the nominal depth for the clamp cases is found to be 26-37% for the 3 mm deep defect and 41-47% for the 6 mm deep defect.

The comparison of the clamp cases with the no clamp reconstructions, shows that there is an additional reconstruction error for the maximum depth (see Table 4.2) and that there are generally more artefacts present for the clamp cases. This is also seen when considering the quality parameters for the deepest point cross-section and the whole thickness map, where the quality parameter is larger by approximately 1.0-2.0 for the deepest point cross-section quality parameter (3.0-4.0 for the whole thickness map quality parameter) for the cases with the clamp. The increase in the quality parameters is also significantly larger than the increase for the support to no support comparison of the previous study. The main explanation of this is that the attenuation caused by the clamp reduces the signal-to-noise ratio, while the noise level remains constant and therefore the influence of the noise is greater on the reconstructions, causing artefacts and reconstruction errors. Also, as another explanation, the clamp does not exert a uniform pressure in the high pressure zone, but there are rather localised zones of increased pressure and therefore coupling between the neoprene mat and pipe, which may act as a localised thickness changes. It is expected that due to the adaptive thresholding in the VISCIT algorithm, some of the localised thickness changes due to the pipe clamp may fall below the lowest threshold. The remaining localised zones of increased thickness may also add to the artefacts. The thickness variations due to the artefacts, both due to the low signal-to-noise ratio and the presence of the clamp, are

however still within the 12.5% manufacturing tolerance for the pipe wall thickness [ASTM International, 2012]. Nonetheless, the ability to extract the necessary information for the thickness reconstruction is not lost, as the defect is detected and correctly located. As a final remark, the dispersion curves employed for the thickness reconstructions of the clamp cases disregard the neoprene mat, rather than accounting for it as a multilayer system. This can be argued via the coupling between the pipe and the neoprene mat, which is not perfect as observed in the experiments and contrary to the assumption of perfect coupling in a multilayer dispersive system.

4.3 STOPAQ(R) Coatings

The last area with restricted access considered concerns with coatings that are typically applied to pipes for corrosion protection or to prevent initial corrosion from growing further. One material that is used for that purpose and investigated here is STOPAQ(R) [STOPAQ B.V., 2015], which is manufactured for example in tape form and wrapped around the pipe, as illustrated in Figure 4.9.

Figure 4.9 shows the experimental setup for the STOPAQ(R) tests, where the 3 mm deep defect is covered with a layer of STOPAQ(R). The dots on the STOPAQ(R) coating indicate the location of the defect, which lies mid-way between the two EMAT arrays with a ring separation distance of 0.602 m. For the tests, first a reference measurement is conducted in the absence of the coating and then the coating is applied by carefully wrapping the STOPAQ(R) tape around the pipe, following the manufacturer's instructions. For the measurements with the coating, the sensor positions are identical to the reference measurement for better comparison. The experiment looks at the influence of the coating over time, as some sort of curing process is expected. The first measurement with the STOPAQ(R) coating is conducted after one day of application. Periodic data captures are conducted to analyse the influence of the STOPAQ(R) coating, however, only the results for one day and twenty-six days after application are shown due to lack of changes in the results.

Similar to the clamp experiment, some attenuation is expected from the STOPAQ(R) coating as it is expected to attenuate the A0 amplitude with its out-of-plane displacement. Based on the reference measurements and the measurements after application of the coating, the

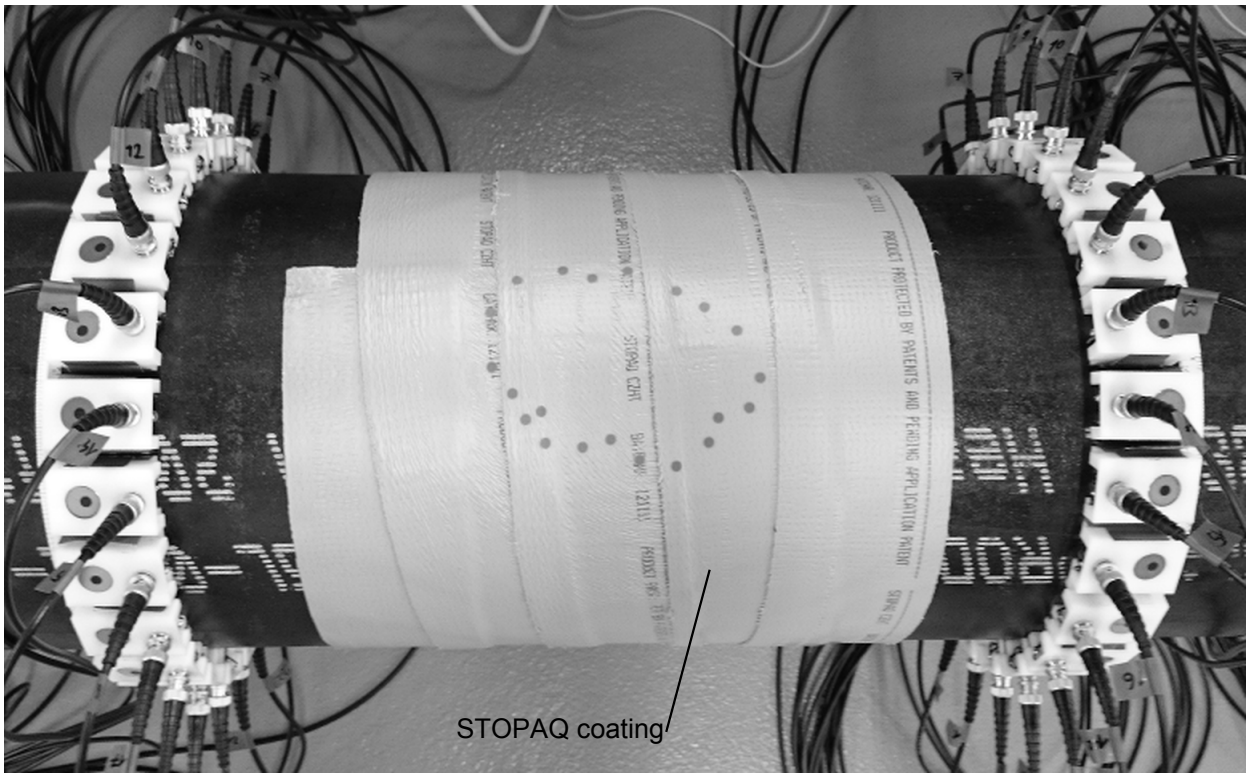

Figure 4.9: Experimental setup of the STOPAQ(R) measurements with a ring separation distance of 0.602 m. The dots on the STOPAQ(R) coating indicate the location of the defect.

attenuation is determined analogous to the calculation of the clamp experiment and found to be approximately 5.2 dB/m (standard deviation of 1.2 dB/m) at the operation frequency of 50 kHz. This value is approximately twice as large as the value given in [Huthwaite et al., 2013a], which has also been determined experimentally on a significantly smaller scaled experiment. With the attenuation for the STOPAQ(R) coating being less than in the case of the pipe clamp, similarly to the pipe clamp experiments, it is expected that the attenuation will not cause the thickness reconstruction to break down.

Table 4.3: Overview of all conducted experiments STOPAQ(R) coating experiments with 0.602 m ring separation distance for the various durations after the application. The maximum depth is the maximum reconstructed depth and quality parameter uses the Frobenius norm for the deepest point cross-section (cross-section) and the total thickness map (all pixel).

application duration	maximum depth	quality parameters	
		cross-section	all pixel
no STOPAQ(R)	2.5 mm	1.1	4.8
1 day	2.4 mm	1.5	5.9
26 days	2.5 mm	1.2	5.6

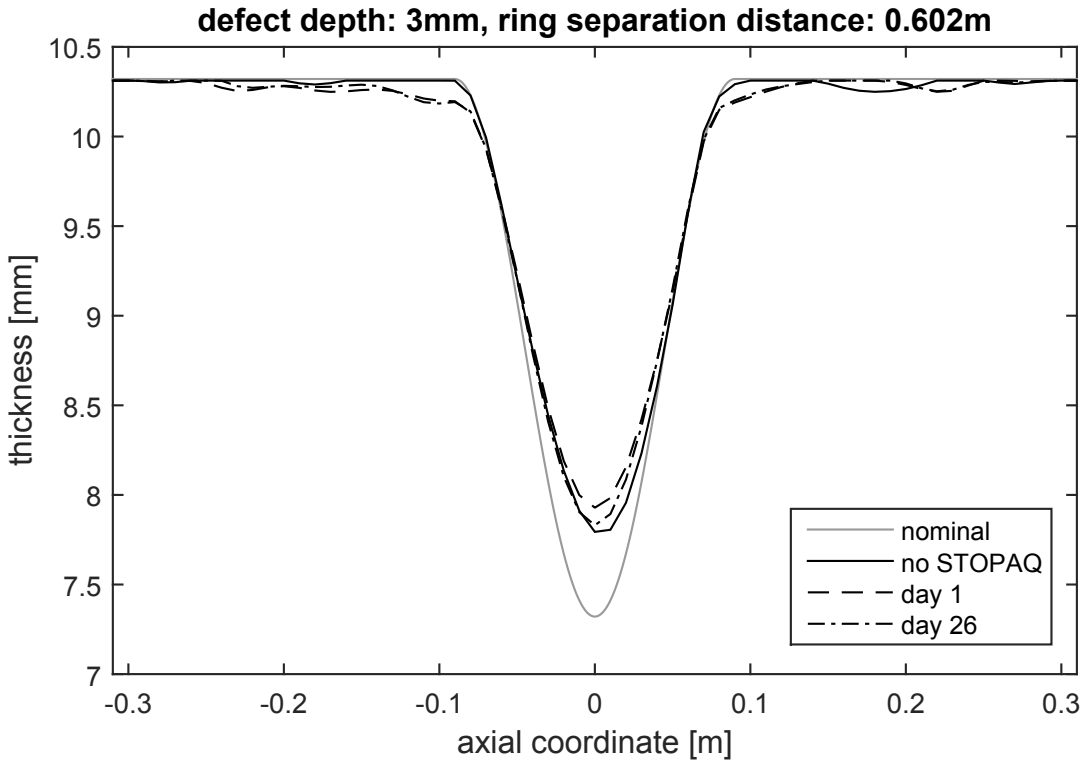

Figure 4.10: Deepest point cross-section for STOPAQ(R) coating experiments conducted on the 3 mm deep defect as a function of the time after application and compared to the nominal defect profile, as well as the uncoated reference measurement. The ring separation distance is selected to be 0.602 m and the dispersion curves used for the data processing disregard the presence of the STOPAQ(R) coating.

Figure 4.10 shows the deepest point cross-section for the STOPAQ(R) coating experiments, comparing them to the reference measurement and the nominal thickness variation. When comparing the cases with the STOPAQ(R) coating with each other, it can be observed that there is only a minor difference between day one and day twenty-six, for both the shape and maximum depth, as both deepest point cross-sections show good agreement. When comparing the STOPAQ(R) coating cases with the nominal thickness variations, good agreement is found in terms of the lateral defect extent near the surface between the reconstruction and the nominal thickness variation up to a depth of approximately 1.3 mm and the maximum depth is underestimated to a similar extent (by about 0.1 mm) as also found in the previous studies regarding the support location and clamp experiment. The maximum depth and the quality parameter for both the reference and STOPAQ(R) coating cases are also listed in Table 4.3. The error in the maximum depth for the STOPAQ(R) cases is found to be 17-20%, which is also the value found for the reference measurement (see Table 4.3). The quality parameter for the deepest point cross-section and the whole thickness map

are slightly higher than the reference measurement case (0.1 for the deepest point cross-section and 0.8 for the whole thickness map quality parameter), especially for the whole thickness map. From a practical point of view and based on the experimental measurements, no "curing process" of the STOPAQ(R) coating is observed in the measurements.

From the above findings, it can be inferred that there is only a small influence of the STOPAQ(R) coating on the thickness reconstructions, as the reconstructed thickness variations for both the STOPAQ(R) cases and reference measurements show very good agreement, in terms of the three analysed parameters. These results may be explained with the insufficient coupling between the STOPAQ(R) coating and the steel pipe, where not enough energy is transferred between the STOPAQ coating and pipe wall to actually cause some distortions in form of a thickness increase. In comparison to the clamp experiments, where there is an additional force involved that assists in improving the coupling between the neoprene mat and pipe wall, some measurable influence is found. For the STOPAQ(R) experiment, the STOPAQ(R) tape is merely wrapped around the pipe and the coupling relies solely on the adhesion (this is also the reason for taking measurements at various times after application due to potential curing processes) at the material interface and potentially additional thickness reconstruction errors would be expected if some force would be present. Also the attenuation due to the STOPAQ(R) is not found to interfere with the thickness reconstructions and interference would only be expected for longer propagation distances under the coating. This would lead to even smaller signal amplitudes and therefore an increased influence of the noise level on the reconstructions, similar to the clamp case. As a final remark, the dispersion curves used for the data processing do not account for the presence of the STOPAQ(R) coating in a multilayer dispersive system, but rather disregard it, similar to the clamp experiment study from the previous section.

4.4 Summary of All Experiments

In the previous sections, various inspection scenarios with restricted access are considered in an experimental study using guided wave tomography and their influence on the thickness reconstruction within the area of interest, relative to a reference measurement are regarded. The general conclusion from the previous studies is that there is an influence of the various scenarios on the thickness reconstructions relative to the reference measurements in terms

of the three analysed parameters (maximum depth, deepest point cross-section and whole thickness map quality parameters), however, the influence is not sufficient enough for the thickness reconstructions to break down. Generally, the regions of restricted access cause a decrease of the maximum reconstructed depth of the defect as well as an increase in the quality parameters in comparison to the reference measurement. Further, the defect could always be detected and located at the correct location.

The study of the support locations has shown that with sufficient contact pressure in the defect area, a localised thickness increase is observed in the reconstructions. This is not found when the contact point does not coincide with the defect. From the clamp experiments it is found that the thickness reconstructions are independent of the location of the defect relative to the high pressure zone of the clamp and the location of the air gap. Further, the attenuation due to the clamp, which reduces the signal-to-noise ratio at a constant noise level and the non-uniform contact conditions between the neoprene mat and the steel pipe do not corrupt the measured data enough for the reconstructions to break down and the defect depth is underestimated further, when compared to the no clamp reference measurements. Similar observations are made for the STOPAQ(R) coating tests, where the attenuation is not significant enough for the reconstructions to break down and only a minor influence of the STOPAQ(R) coating on the thickness reconstruction is found relative to the reference measurement in terms of the three analysed parameters. As a final remark, for all data processing, the dispersion curves are based on the dispersion curves illustrated in Figure 1.2 for a steel plate, disregarding the presence of for example the neoprene mat and STOPAQ(R) coating.

Chapter 5

Summary

5.1 Thesis Review

In this research, an EMAT based guided wave tomography system employing the A0 Lamb mode and operated at 0.5 MHzmm has been developed and experimentally tested. Various aspects around the robustness and repeatability of measurements are considered and established for the operation within the limitations of the experimental conditions on a laboratory scale. The main focus of this research in terms of the inspection scenario is the inspection of areas with restricted access, such as support locations, pipe clamps and coatings, as these represent the targeted application of the guided wave tomography system.

5.1.1 EMAT and Guided Wave Tomography System Development

An omni-directional low frequency A0 Lamb wave EMAT operating on a steel plate has been developed with a target A0-S0 ratio of approximately 30 dB. In a first step, a parametric FE model of the design concept has been implemented in COMSOL, where the bias magnetic field is calculated initially, then combined with the eddy current caused by the induction coil to produce a force. In a second step, a numerical optimization process employing a

genetic algorithm has been set up and the EMAT design is optimized to yield an improved A0 mode selectivity. The parameters subjected to optimization are the magnet diameter and the magnet lift-off, which control the direction and magnitude of the exciting forces in the skin depth layer and therefore the mode selectivity.

For the initial optimisation process, only the Lorentz force is considered for the wave excitation besides the magnetisation force and from the optimised design a physical prototype has been built. The FE model is validated for measurements on an Aluminium plate for the Lorentz force excitation mechanism and on a steel plate for both the Lorentz and magnetisation force. For the steel plate, it is found that only considering the Lorentz force leads to a significant overestimation of the mode selectivity, as the S0 amplitude is underestimated by the Lorentz force, but the A0 amplitude remains mainly uninfluenced. Further, it has been found that additionally including the magnetisation force into the optimisation process leads to a better mode selectivity, however, the optimisation drives the optimum to the minimum magnet diameter and therefore reduces the sensitivity. A numerical robustness study is conducted and robustness is found for fairly large variations of the magnet lift-off and the magnetic permeability. Based on these findings, a two-step model-based design approach is proposed whereby in the first step, the Lorentz force is used for excitation and an optimised design is found. In the second step, a realistic estimate of the mode selectivity of the optimised design is obtained by additionally considering the magnetisation force.

The developed EMAT prototype is integrated into a guided wave tomography system, which consists of two ring arrays of 24 sensors each. The data acquisition is computer controlled, allowing for automatic switching of the transmitting sensor. The receiving sensors are multiplexed manually, as in an experimental study it is found that, when placing the multiplexer before the receiver amplifier, the experimental noise is greater than the signal level. Placing the receiver amplifier before the multiplexer is one solution to overcome this issue, but is not pursued here.

5.1.2 Guided Wave Tomography and System Robustness

The developed guided wave tomography system is used in experimental tests on a 12 in schedule 40 pipe specimen with a smoothly varying and well defined artificial defect. The experiments consider two defects (3 mm and 6 mm deep), which are chosen to be unaffected

by the resolution limit of around two wavelengths, such that the influence of the areas with restricted access can be studied better. The thickness reconstructions are based on the HARBUT algorithm, which has been shown to be suitable for guided wave tomography. Due to the nature of the experimental setup, where two ring arrays are placed on either side of the area of interest, a limited view problem arises, for which the VISCIT algorithm is employed. The effect of the limited view problem can be partially facilitated by considering the helical paths between a sender and a receiver, which exist due to the circular symmetry of the pipe geometry. A robust algorithm is employed to extract the higher order helical paths, which effectively increases the array length of two parallel arrays, when regarding the unwrapped pipe.

As an initial test of the system and to analyse the expected performance in terms of the thickness reconstructions, a reference measurement is conducted, whereby direct access to the area of interest is possible. From the reference measurements, it is found that the limited view configuration adds a reconstruction error in terms of the maximum depth, relative to a full view problem for an identical defect machined onto a plate as found in the literature. Despite this additional reconstruction error relative to a full view configuration, the defect is detected and correctly located.

Further, several practical aspects of guided wave tomography measurements have been considered to evaluate the robustness of the guided wave tomography system for the experimental studies on areas with restricted access, within the limits of the expected experimental conditions on a laboratory scale. The repeatability of measurements is evaluated for measurements on both defects considered here and are found to be very repeatable. The influence of the ring separation distance between the two ring arrays on the thickness reconstruction is also assessed and it is found that in terms of the three analysed parameters (maximum reconstructed depth, deepest point cross-section and whole thickness map quality parameters), with increasing ring separation distance, the reconstruction error and the quality parameters increase. For practical applications it is therefore inferred that the shortest possible ring separation distance within limits should be employed. Similarly, no significant influence on the thickness reconstruction is found for the cases in which the defect is located closer to one of the two arrays, in terms of the three analysed parameters and relative to a symmetric experimental setup. For experiments, it is however recommended to consider a symmetric layout around the area of interest with the two ring arrays.

The influence of sensor position errors on the thickness reconstruction is also studied and it is found that for a position error of a single sensor, no significant influence is found, in terms of the three analysed parameters and relative to a no error reference measurement. This is attributed to the fact that only a very small number of send-receive combinations are compromised by the shifted sensor position. A systematic misalignment is studied considering an inclined array, whereby all array sensors in the transmitter array are shifted axially. The thickness reconstructions have shown that there is an influence, whereby the reconstruction error as well as the quality parameters for the deepest point cross-section and whole thickness map increase slightly due to the inclined array (maximum depth for example decreases by 0.2 mm relative to the no error reference measurement for the 3 mm deep defect). However, the ability to detect and correctly locate the defect is not lost. An unsystematic misalignment of both arrays is considered by superimposing each sensor with a sensor position error and it is found that in terms of the three analysed parameters and relative to a no error reference measurement, there is an change in the the three analysed parameters (maximum depth for example decreases by 0.2 mm relative to the no error reference measurement for the 3 mm deep defect). This increase of the quality parameters and decrease of the maximum reconstructed depth, however, is not significant enough to cause a break down of the thickness reconstructions. The reason for this may be attributed to the position calibration, which is able to correct for most of the deliberately introduced sensor position errors, implying robustness of the guided wave tomography system to such position errors of up to ± 20 mm (half the A0 wavelength). This also means that there is no need for a very strict tolerance on the sensor position, but for practical purposes, large sensor position errors should be avoided to avoid losses in accuracy.

Based on the experimental data, numerical alterations of the experimental data are performed in order to study further influences on the thickness reconstructions. Based on a statistical analysis, it is found that by scaling the experimental datasets in terms of their amplitude and introducing a phase shift, the position calibration is able to compensate for this kind of manipulation. The failure of one or more sensors within both arrays is studied by setting the measured data of the failed sensor to one corresponding to experimental noise (normally distributed). The results show that the failure of a single sensor does not exhibit a significant influence on the thickness reconstruction, in terms of the three analysed parameters and relative to a no error reference measurement. Likewise, the increase in re-

construction error for a gap of four A0 wavelength (≈160 mm) is not found to be significant, for the reconstruction to break down. By increasing the array spacing to two A0 wavelength (≈80 mm), it is found that the maximum depth is not severely influenced (change of 0.1 mm relative to the reference case), however an increase in reconstruction artefacts is recorded. Further increases in the array spacing leads to the breaking down of the thickness reconstructions.

Another signal processing technique based on Golay complementary sequences is studied, as this allows for faster data capture over time averaging. It is found that Golay complementary sequences may reduce the data capture duration by six to seven times at the same accuracy. Also, the application of Golay complementary sequences in conjunction with low voltage excitation is tested, which may allow for battery operation of the guided wave tomography system. All thickness reconstructions obtained with Golay complementary sequences match the performance of the averaging data acquisition in terms of the three analysed parameters, making them feasible for future applications.

5.1.3 Inspection of Areas with Restricted Access

Having established the robustness and repeatability of measurements within the limits of the expected experimental conditions, three areas with restricted access, regarding support locations, pipe clamps and STOPAQ(R) coatings are investigated in further experimental studies. These studies of the influence of these inspection scenarios on the thickness reconstruction represent one of the key findings here and consider the changes relative to a reference measurement in the absence of the area with restricted access.

For the experimental study regarding the influence of support locations on the thickness reconstruction, two support types are considered, a h-beam and a rod support, which are typical supports occurring in the petrochemical industry and are loaded with up to 20 kN. The comparison to the reference measurements show that for the h-beam, no significant influence on the thickness reconstruction is found in terms of the three considered parameters. For the case of the rod support, only an influence is found when the contact point is within the defect region, however the thickness reconstruction remains uninfluenced for contact points outside the defect. This behaviour has been attributed to the VISCIT algorithm that uses an adaptive thresholding approach, which removes the effect of the localised

thickness increase that lies beneath the lowest threshold, as in the case of the contact point located outside of the defect region. In the case of the contact point within the defect region, the localised thickness increase lies above the lowest VISCIT threshold, because of the superposition with the defect.

The experimental studies on the pipe clamps looks at influence on the thickness reconstructions of the circumferential location of the defect under the pipe clamp. From the thickness reconstructions, it is found that there is no significant influence of the location of the defect under the clamp on the thickness reconstructions. An increase in the thickness reconstruction errors as well as quality parameters is observed in the presence of the pipe clamp, when compared to the reference measurement, which could be mainly explained by the strong attenuation (of around 11 dB/m) due to the pipe clamp, allowing for a reduced signal-to-noise ratio at a constant noise level and therefore enhancing the influence of the noise and causing reconstruction artefacts. A further explanation may be found in the non-uniform coupling conditions, which may act as localised thickness increases, further adding to the reconstruction artefacts.

The experimental study with the STOPAQ(R) coating looks at the influence of the coating over a time on the thickness reconstruction and it is found that there is no significant influence of the three analysed parameters relative to a reference measurement. Further, an increased attenuation of 5 dB/m relative to the reference measurement is measured, which is however not sufficient for the thickness reconstruction to break down.

5.2 Areas of Future Work

There are multiple opportunities for future work that are identified based on the findings from this research project.

The first area of future work concerns the development of the guided wave tomography system and the EMATs within the guided wave tomography system. Since the EMAT development only focuses on the shaping of the magnetic flux and maintaining the coil parameters (dimensions and turn numbers) constant, these can be considered for further enhancement of the EMAT. Improvements may be achieved regarding the signal-to-noise performance, by tailoring the coil impedance and electronics specifically to the transmission

or reception purpose. An improved signal-to-noise performance will enhance the data acquisition speed, as fewer time averages could be used. Another consideration is the EMAT model itself, since it employs a linear approximation of the ferromagnetic material and therefore constrains model to a small range of magnetic flux densities. By employing a more realistic ferromagnetic material model, EMAT designs which are capable of operating in the region of magnetic saturation can be considered, for example based on a design as presented in [Koch et al., 2008]. A higher magnetic flux density in the skin depth layer leads to higher Lorentz forces (and magnetisation forces) and in turn to larger excitation amplitudes in the elastic displacement field. Also, magnetic saturation in the skin depth layer reduces the perceived magnetic permeability, which is another parameter that is able to change the direction of the magnetic flux density and subsequently the direction of the excitation force.

The second area of future work regards the deployment of the guided wave tomography system. Having established the robust operation within the limitations imposed by the expected experimental conditions on a laboratory scale, initial practical issues have been eliminated and in a further step, the actual performance bounds (potentially defined as the breakdown of the thickness reconstructions) of the guided wave tomography system can be studied, regarding the whole parameter space (such as for example a phase variation study using the STOPAQ(R) experimental data), which may influence the overall system performance.

The two main parameters influencing the performance bounds of the guided wave tomography system that are considered here are the EMAT arrays and the defect itself. The performance bounds may not be limited to those two parameters and in order to identify further parameters, a parameter identification study may be conducted, in order to identify for example, whether environmental conditions may limit the performance of the guided wave tomography system. The studies regarding the EMAT arrays consider for example sensor position errors in the presence of areas with restricted access and can be investigated via simulations or experiment, however, for experimental studies, parallel data capture on the receiving array should be considered, in order to enhance the efficiency of the research process.

Since only smoothly varying and well defined defects are considered here, tests on more

realistic defects could be conducted to study the influence of rough corrosion defects onto the thickness reconstructions, also considering defects, which are smaller than the two wavelength resolution limit of the algorithm due to the difference in scattering of acoustic and elastic waves. In [Huthwaite and Seher, 2015], it could be shown that for a simple defect, the simulation and experimental measurements show very good agreement, and therefore a numerical approach should be chosen as a first instance for the studies. As real corrosion defects tend to be gradual thickness changes with a rough surface and potentially deep spikes, it is likely that these deep spikes may not be correctly approximated with the thickness reconstruction algorithm due to the resolution limit. Other numerical studies that may help in determining the limitations of the tomography system and thickness reconstruction algorithms included the presence of multiple defects as well as corrosion over larger areas. The latter may also pose challenges for the position calibration, since a larger percentage of send-receive combinations may be affected.

References

[Achenbach, 1973] Achenbach, J. D. (1973). *Wave Propagation in Elastic Solids*. North-Holland Pub. Co.

[Achenbach and Xu, 1999] Achenbach, J. D. and Xu, Y. (1999). Wave motion in an isotropic elastic layer generated by a time-harmonic point load of arbitrary direction. *The Journal of the Acoustical Society of America*, 106:83–90.

[Arnold Magnetic Technologies Corporation, 2009] Arnold Magnetic Technologies Corporation (2009). Datasheet of N42 Nd-Fe-B Magnets.

[ASTM International, 2012] ASTM International (2012). A530 / A530M-12, Specification for General Requirements for Specialized Carbon Steel and Alloy Steel Pipe.

[Auld, 1990] Auld, B. A. (1990). *Acoustic Fields and Waves in Solids*. Krieger Publishing Company.

[Belanger, 2010] Belanger, P. (2010). *Feasibility of thickness mapping using ultrasonic guided waves*. PhD thesis, Imperial College London.

[Belanger, 2014] Belanger, P. (2014). High order shear horizontal modes for minimum remnant thickness. *Ultrasonics*, 54:1078–87.

[Belanger et al., 2010] Belanger, P., Cawley, P., and Simonetti, F. (2010). Guided wave diffraction tomography within the Born approximation. *IEEE Transactions on Ultrasonics Ferroelectrics and Frequency Control*, 57:1405–1418.

[Bellac and Levy-Leblond, 1973] Bellac, M. and Levy-Leblond, J. M. (1973). Galilean electromagnetism. *Il Nuovo Cimento*, 14:217–234.

[Born et al., 2000] Born, M., Wolf, E., Bhatia, A. B., Clemmow, P. C., Gabor, D., Stokes, A. R., Taylor, A. M., Wayman, P. A., and Wilcock, W. L. (2000). *Principles of Optics: Electromagnetic Theory of Propagation, Interference and Diffraction of Light*. Cambridge University Press.

[Bozorth, 1951] Bozorth, R. M. (1951). *Ferromagnetism*. Van Nostrand.

[Brath et al., 2014] Brath, A. J., Simonetti, F., Nagy, P. B., and Instanes, G. (2014). Acoustic formulation of elastic guided wave propagation and scattering in curved tubular structures. *Ultrasonics, Ferroelectrics, and Frequency Control, IEEE Transactions on*, 61:815–829.

[British Standards Institution, 2011] British Standards Institution (2011). BSI 9690, Non-destructive testing, Guided wave testing, General guidance and principles.

[Brown, 1953] Brown, W. F. (1953). Magnetic energy formulas and their relation to magnetization theory. *Rev. Mod. Phys.*, 25:131–135.

[Brown, 1966] Brown, W. F. (1966). *Magnetoelastic Interactions*. Springer.

[Carandente and Cawley, 2012] Carandente, R. and Cawley, P. (2012). The effect of complex defect profiles on the reflection of the fundamental torsional mode in pipes. *NDT & E International*, 46:41–47.

[Challis et al., 2013] Challis, R., Ivchenko, V., and Al-Lashi, R. (2013). Ultrasonic attenuation measurements at very high SNR: Correlation, information theory and performance. *Journal of Physics: Conference Series*, 457:012004.

[Challis and Ivchenko, 2011] Challis, R. E. and Ivchenko, V. G. (2011). Sub-threshold sampling in a correlation-based ultrasonic spectrometer.

[Chari and Reece, 1974] Chari, M. V. K. and Reece, P. (1974). Magnetic field distribution in solid metallic Structures in the vicinity of current carrying conductors, and associated Eddy-current losses. *IEEE Transactions on Power Apparatus and Systems*, 93:45–56.

[Chian and Moon, 1981] Chian, C. T. and Moon, F. C. (1981). Magnetically induced cylindrical stress waves in a thermoelastic conductor. *International Journal of Solids and Structures*, 17:1021–1035.

[COMSOL Inc., 2012] COMSOL Inc. (2012). Documentation of COMSOL 4.3a. http://www.comsol.com/.

[Cook, 1960] Cook, C. E. (1960). Pulse Compression-Key to More Efficient Radar Transmission. *Proceedings of the IRE*, 48:310–316.

[Corcoran, 2015] Corcoran, J. (2015). Personal Conversation.

[Craig et al., 1962] Craig, S. E., Fishbein, W., and Rittenbach, O. E. (1962). Continuous-Wave Radar with High Range Resolution and Unambiguous Velocity Determination. *Military Electronics, IRE Transactions on*, MIL-6:153–161.

[Drozdz, 2008] Drozdz, M. (2008). *Efficient finite element modelling of ultrasound waves in elastic media'*. PhD thesis, Imperial College London.

[Engdahl, 2000] Engdahl, G. (2000). *Handbook of Giant Magnetostrictive Materials*. Academic Press.

[Fong and Lowe, 2004] Fong, J. and Lowe, M. J. S. (2004). Curvature Effect on the Properties of Guided Waves in Plates. *AIP Conference Proceedings*, 700:126–133.

[Golay, 1961] Golay, M. J. E. (1961). Complementary series. *Information Theory, IRE Transactions on*, 7:82–87.

[Golub and Van Loan, 1996] Golub, G. and Van Loan, C. (1996). *Matrix Computations*. The John Hopkins University Press, Baltimore and London.

[Hirao and Ogi, 2003] Hirao, M. and Ogi, H. (2003). *EMATs for Science and Industry: Noncontacting Ultrasonic Measurements*. Kluwer Academic Publishers.

[Hou et al., 2004] Hou, J., Leonard, K. R., and Hinders, M. K. (2004). Automatic multi-mode Lamb wave arrival time extraction for improved tomographic reconstruction. *Inverse Problems*, 20:1873–1888.

[Huthwaite, 2012] Huthwaite, P. (2012). *Quantitative imaging with mechanical waves*. PhD thesis, Imperial College London.

[Huthwaite, 2014] Huthwaite, P. (2014). Evaluation of inversion approaches for guided wave thickness mapping. *Proceedings of the Royal Society A: Mathematical, Physical and Engineering Sciences*, 470(2166).

[Huthwaite et al., 2013a] Huthwaite, P., Ribichini, R., Cawley, P., and Lowe, M. J. S. (2013a). Mode selection for corrosion detection in pipes and vessels via guided wave tomography. *IEEE Transactions on Ultrasonics, Ferroelectrics and Frequency Control*, 60:1165–1177.

[Huthwaite and Seher, 2015] Huthwaite, P. and Seher, M. (2015). Robust helical path separation for thickness mapping of pipes by guided wave tomography. *IEEE Transactions on Ultrasonics, Ferroelectrics, and Frequency Control*, 65:927–938.

[Huthwaite and Simonetti, 2011] Huthwaite, P. and Simonetti, F. (2011). High-resolution imaging without iteration: a fast and robust method for breast ultrasound tomography. *The Journal of the Acoustical Society of America*, 130:1721–1734.

[Huthwaite and Simonetti, 2013] Huthwaite, P. and Simonetti, F. (2013). High-resolution guided wave tomography. *Wave Motion*, 50:979–993.

[Huthwaite et al., 2013b] Huthwaite, P., Zwiebel, A., and Simonetti, F. (2013b). A new regularization technique for limited-view sound-speed imaging. *IEEE Transactions on Ultrasonics, Ferroelectrics, and Frequency Control*, 60:603–613.

[Instanes et al., 2014] Instanes, G., Nagy, P. B., Simonetti, F., and Willey, C. L. (2014). Measuring wall thickness loss for a structure. *Patent*, (US20140208852 A1).

[Instanes et al., 2015] Instanes, G., Pedersen, A. O., Brath, A., Willey, C. L., Nagy, P. B., and Simonetti, F. (2015). Ultrasonic Computerized Tomography for Continuous Monitoring of Corrosion and Erosion Damage in Pipelines. *NACE International Corrosion*.

[Jackson, 1998] Jackson, J. (1998). *Classical Electrodynamics Third Edition*. Wiley.

[Jansen and Hutchins, 1990] Jansen, D. P. and Hutchins, D. A. (1990). Lamb wave tomography. *Ultrasonics Symposium, 1990. Proceedings., IEEE 1990*, 2:1017–1020.

[Jiles, 1998] Jiles, D. (1998). *Introduction to Magnetism and Magnetic Materials*. Chapman and Hall.

[Kak and Slaney, 2001] Kak, A. C. and Slaney, M. (2001). *Principles of Computerized Tomographic Imaging*. Society for Industrial and Applied Mathematics.

[Koch et al., 2008] Koch, R. H., May, A., and Li, J. (2008). Electromagnetic acoustic transducers for use in ultrasound inspection systems. *Patent*, (US7426867).

[Lamb, 1917] Lamb, H. (1917). On Waves in an elastic plate. *Proceedings of the Royal Society of London A: Mathematical, Physical and Engineering Sciences*, 93:114–128.

[Lee, 1955] Lee, E. W. (1955). Magnetostriction and Magnetomechanical Effects. *Reports on Progress in Physics*, 18:184.

[Liu and Qu, 1998] Liu, G. and Qu, J. (1998). Guided Circumferential Waves in a Circular Annulus. *Journal of Applied Mechanics*, 65:424–430.

[Lowe and Pavlakovic, 2013] Lowe, M. and Pavlakovic, B. (2013). DISPERSE user manual. http://www3.imperial.ac.uk/nde/products%20and%20services/disperse.

[Malvern, 1969] Malvern, L. E. (1969). *Introduction to the Mechanics of a Continuous Medium*. Prentice-Hall.

[Miller and Hinders, 2014] Miller, C. A. and Hinders, M. K. (2014). Classification of flaw severity using pattern recognition for guided wave-based structural health monitoring. *Ultrasonics*, 54:247–258.

[Moon, 1984] Moon, F. C. (1984). *Magneto-solid Mechanics*. John Wiley & Sons Inc.

[Nagy et al., 2014] Nagy, P. B., F. Simonetti, and G. Instanes (2014). Corrosion and erosion monitoring in plates and pipes using constant group velocity Lamb wave inspection. *Ultrasonics*, 54:1832 – 1841.

[Pei et al., 1996] Pei, J., Yousuf, M. I., Degertekin, F. L., Honein, B. V., and Khuri-Yakub, B. T. (1996). Lamb wave tomography and its application in pipe erosion/corrosion monitoring. *Research in Nondestructive Evaluation*, 8:189–197.

[Phang et al., 2008] Phang, A. P. Y., Challis, R. E., Ivchenko, V. G., and Kalashnikov, A. N. (2008). A field programmable gate array-based ultrasonic spectrometer. *Measurement Science and Technology*, 19:045802.

[Ribichini, 2011] Ribichini, R. (2011). *Modeling of electromagnetic acoustic transducers*. PhD thesis, Imperial College London.

[Ribichini et al., 2012] Ribichini, R., Nagy, P. B., and Ogi, H. (2012). The impact of magnetostriction on the transduction of normal bias field EMATs. *NDT & E International*, 51:8–15.

[Rose, 2004] Rose, J. L. (2004). *Ultrasonic Waves in Solid Media*. Cambridge University Press.

[Rose and Barshinger, 1998] Rose, J. L. and Barshinger, J. (1998). Using ultrasonic guided wave mode cutoff for corrosion detection and classification. *Ultrasonics Symposium, 1998. Proceedings., 1998 IEEE*, 1:851–854.

[Sergey Fomel, 1997] Sergey Fomel (1997). Traveltime computation with the linearized eikonal equation. *SEP report 94*, pages 123–131.

[Simonetti and Huang, 2008] Simonetti, F. and Huang, L. (2008). From beamforming to diffraction tomography. *Journal of Applied Physics*, 103:103110–103117.

[Simonetti et al., 2007] Simonetti, F., Huang, L., and Duric, N. (2007). On the spatial sampling of wave fields with circular ring apertures. *Journal of Applied Physics*, 101:83103–83106.

[STOPAQ B.V., 2015] STOPAQ B.V. (2015). Datasheet for STOPAQ CHZT.

[The MathWorks Inc., 2012] The MathWorks Inc. (2012). Documentation of Matlab R2012b. http://www.mathworks.co.uk/.

[Thompson, 1978] Thompson, R. B. (1978). A model for the electromagnetic generation of ultrasonic guided waves in ferromagnetic metal polycrystals. *IEEE Transactions on Sonics and Ultrasonics*, 25:7–15.

[Volker and van Zon, 2013] Volker, A. and van Zon, T. (2013). Guided wave travel time tomography for bends. *Review of Progress in QNDE, edited by D. O. Thompson and D. E. Chimenti, AIP Conference Proceedings*, 1511:737–744.

[Volker et al., 2015] Volker, A., van Zon, T., and van der Leden, E. (2015). Field trials results of guided wave tomography. *Review of Progress in QNDE, edited by D. O. Thompson and D. E. Chimenti, AIP Conference Proceedings*, 1650:615–621.

[Volker and Vos, 2012] Volker, A. and Vos, H. (2012). Experimental results of guided wave travel time tomography. *Review of Progress in QNDE, edited by D. O. Thompson and D. E. Chimenti, AIP Conference Proceedings*, 1430:1968–1975.

[Volker and Vos, 2013] Volker, A. and Vos, R. (2013). Annular plate inspection using guided wave tomography. *Review of Progress in QNDE, edited by D. O. Thompson and D. E. Chimenti, AIP Conference Proceedings*, 1511:745–752.

[Wagner et al., 2013] Wagner, R., Goncalves, O., Demma, A., and Lowe, M. (2013). Guided wave testing performance studies: comparison with ultrasonic and magnetic flux leakage pigs. *Insight*, 55:187–196.

[Wilcox, 2003] Wilcox, P. D. (2003). A rapid signal processing technique to remove the effect of dispersion from guided wave signals. *Ultrasonics, Ferroelectrics, and Frequency Control, IEEE Transactions on*, 50:419–427.

[Wilcox et al., 2005] Wilcox, P. D., Lowe, M. J. S., and Cawley, P. (2005). The excitation and detection of Lamb waves with planar coil electromagnetic acoustic transducers. *IEEE Transactions on Ultrasonics, Ferroelectrics and Frequency Control*, 52:2370–2383.

[Winter, 1995] Winter, G. (1995). *Genetic Algorithms in Engineering and Computer Science*. Wiley.

[Wright et al., 1997] Wright, W., Hutchins, D., Jansen, D., and Schindel, D. (1997). Air-coupled Lamb wave tomography. *Ultrasonics, Ferroelectrics, and Frequency Control, IEEE Transactions on*, 44:53–59.

List of Publications

[P1] M. Seher, P. Huthwaite, M. J. S. Lowe, P. B. Nagy, P. Cawley, "Numerical design optimization of an EMAT for A0 Lamb wave generation in steel plates", in *Review of Progress in Quantitative Nondestructive Evaluation Edited by D. O. Thompson, D. E. Chimenti, AIP Conference Proceedings*, 1581:340-347, Baltimore, Maryland, USA, 2014.

[P2] M. Seher, P. Huthwaite, M. J. S. Lowe, P. Cawley, "Experimental study of A0 Lamb wave tomography", in *Review of Progress in Quantitative Nondestructive Evaluation Edited by D. O. Thompson, D. E. Chimenti, AIP Conference Proceedings*, 1650:245-253, Boise, Idaho, USA, 2015.

[P3] P. Huthwaite, M. Seher, "Helical Path Separation For Guided Wave Tomography", in *Review of Progress in Quantitative Nondestructive Evaluation Edited by D. O. Thompson, D. E. Chimenti, AIP Conference Proceedings*, 1650:761-770, Boise, Idaho, USA, 2015.

[P4] P. Huthwaite, M. Seher, "Robust helical path separation for thickness mapping of pipes by guided wave tomography", in *IEEE Transactions on Ultrasonics, Ferroelectrics, and Frequency Control*, Volume 62, Issue 5, 2015

[P5] M. Seher, P. Huthwaite, M. J. S. Lowe, P. B. Nagy, "Model-based design of low frequency Lamb wave EMATs for mode selectivity", in *Journal of Nondestructive Evaluation*, accepted for publication, 2015

Appendix A

Guided Wave Tomography vs. Point Thickness Measurements

The presented studies all look at the comparison of the thickness measurement based on guided wave tomography with the nominal thickness variation, which allows for better and easier comparison of the various measurements. In this section, the thickness map of the guided wave tomography thickness reconstruction is compared to the ultrasonic point thickness gauging, a technique widely used in the petrochemical industry for thickness gauging.

Ultrasonic point thickness gauging (often referred to as point UT) is a technique in which a bulk wave (pressure or shear wave) is transmitted into a material at the front wall with normal incident and the reflection from the back wall is measured. The thickness can then be determined via the time delay between various reflections, based on a known wave speed, which needs to be calibrated before the measurement, usually on a block of the same material and known thickness. It needs to be noted that this approach only supplies a thickness for a specific location and for thickness mapping a whole area, multiple measurements need to be conducted, making this approach very labour intensive. Further, direct access to the region of interest is necessary.

The comparison of both thickness gauging techniques uses the 3 mm deep defect pipe as an example and both techniques are used to measure the thickness of the pipe wall. The

guided wave tomography approach uses the experimental setup presented in Figure 2.13 with a ring separation distance of 0.602 m. The ultrasonic point thickness measurement uses an Innerspec PowerBox H (Innerspec Technologies Inc., Lynchburg, Virginia, USA) instrument, which is used to generate and measure a single cycle shear waves toneburst centred at a frequency of 3.2 MHz. The calibration for the ultrasonic point thickness gauging is conducted on the pipe itself and calibrated against measurements with a micrometer screw gauge, such that an accuracy to the nearest 0.1 mm is assumed to be achievable. The pipe wall thickness is measured along a stretch of 0.8 m and sampled every 20 mm (half the A0 wavelength at the operation point of the guided wave tomography system) in the axial and circumferential directions.

The measured thickness maps on the 3 mm deep defect pipe are illustrated in Figure A.1, for the ultrasonic point thickness measurements in (a) and in (b) for the guided wave tomography reconstructions. For both thickness maps, the same range for the colour map is selected to allow for an easier comparison between the two methods.

The thickness map in Figure A.1(a) is an interpolated version of the raw thickness map from a 20 mm to a 5 mm spacing of the grid points for better visualisation. From Figure A.1(a) it can be seen that the defect does not seem to be axisymmetric as it would be expected from the nominal defect profile. This may be explained with the machining of the defect itself. Since the pipe is not a perfect cylinder, but rather oval shaped and the trajectory of the milling tool assumes a perfect cylinder, a discrepancy in terms of the shape of the defect is expected, especially in the circumferential direction. Another observation from the thickness map of Figure A.1(a), as indicated by the dashed line, is that there are signatures of helical welds visible, running parallel to the dashed line. This could be traced back to the manufacturing process of the pipe, which is welded from helically bent strips and is also observed and confirmed on the pipe specimen by subsequent visual inspection.

For the guide wave tomography thickness map in Figure A.1(b), a smoother variation of thickness is seen in comparison to the thickness map obtained with ultrasonic point thickness measurements, which is imposed by the resolution limit of the tomography algorithm and therefore is unable to resolve the finer features such as the weld signatures. Additionally, the welds from the manufacturing process are also not visible in the guided wave tomography thickness map, as thickness increase in the weld region are below the lowest threshold of

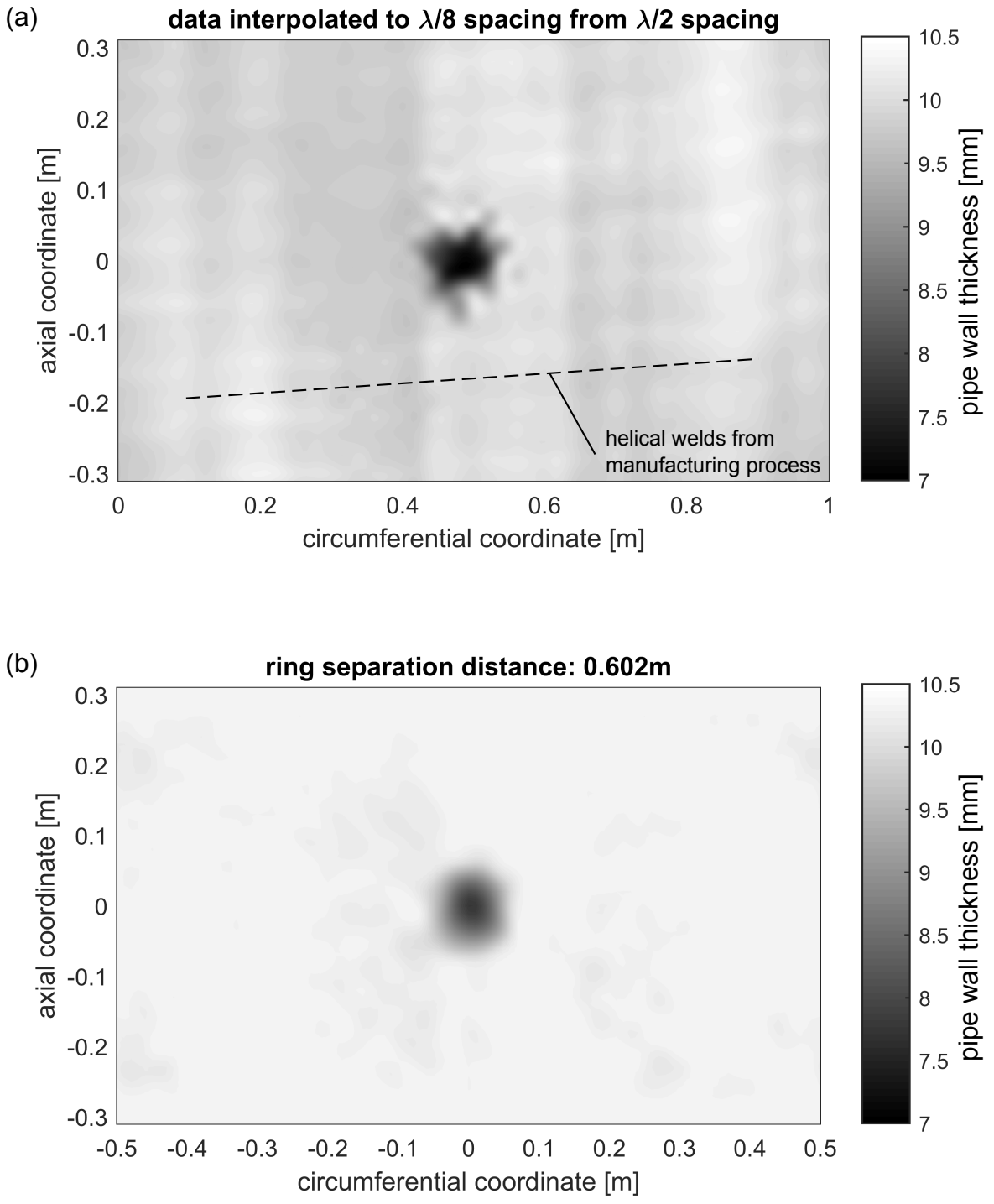

Figure A.1: Comparison of the thickness maps obtained from an ultrasonic point thickness measurement (a) and guided wave tomography (b). The ultrasonic point thickness measurements are sampled every 20 mm (half the A0 wavelength) and interpolated onto a higher resolution grid (eighth of the A0 wavelength). The guided wave tomography thickness map is measured with a ring separation distance of 0.602 m.

Table A.1: Comparison of the thickness reconstructions (ring separation distance of 0.602 m) with a point thickness gauging technique (Innerspec PowerBox H, Innerspec Technologies Inc., Lynchburg, Virginia USA) and nominal thickness variation. The mean background thickness refers to the mean thickness outside the region of the defect.

thickness gauging method	maximum depth	mean background thickness
nominal thickness	3.0 mm	10.3 mm
point UT measurement	2.8 mm	9.9 mm
guided wave tomography	2.6 mm	10.3 mm

VISCIT and therefore assigned the background value.

When comparing both thickness maps in Figure A.1(a) and Figure A.1(b), it is observed that the thickness map measured with the ultrasonic point thickness gauging has an overall darker shade of gray. The mean thickness outside the defect region for both thickness measurement approaches is listed in Table A.1, where the mean thickness for the ultrasonic point thickness measurements is 0.4 mm lower than the mean thickness of the guided wave tomography measurement. This is because the tomography algorithm assumes the nominal thickness as the background thickness for the computations, rather than the actual thickness. The comparison of the maximum defect depth needs to be treated with caution, as in case of guided wave tomography, the reconstruction error increases with increasing defect depth (as previously found). However, for shallow defects like the 3 mm deep defect, good agreement between both thickness gauging techniques is found. For a deeper defect such as the 6 mm deep defect, it is found that the discrepancy in terms of the maximum depth is greater.

As a conclusion from this comparison, it is found that for the 3 mm deep defect considered in this study, the guided wave tomography thickness matches the accuracy of the ultrasonic point thickness gauging well. This may be exploited to screen larger areas where only shallow defects are expected, as the inspection with guided wave tomography may be less labour intensive. On another note, the mean background thickness obtained with the ultrasonic point thickness measurement is still within the manufacturing tolerance for the pipe wall thickness, which is quoted with 12.5% [ASTM International, 2012] and the tolerance can be confirmed with these measurements. Since the pipe wall thickness is close to 10 mm, the comparison with the full view reconstructions on a plate in [Huthwaite, 2014] may be considered more valid.